

A Practical High Temperature Photonic Crystal for High Performance Thermophotovoltaics

by

Veronika Stelmakh

B.S., University of Texas at Arlington (2007)

M.S. Massachusetts Institute of Technology (2011)

Submitted to the Department of Electrical Engineering and Computer
Science

in partial fulfillment of the requirements for the degree of

Doctor of Philosophy

at the

MASSACHUSETTS INSTITUTE OF TECHNOLOGY

June 2017

© Massachusetts Institute of Technology 2017. All rights reserved.

Author
Department of Electrical Engineering and Computer Science
May 18th, 2017

Certified by
Dr. Ivan Celanovic
Principal Research Scientist
Thesis Supervisor

Accepted by
Professor Leslie A. Kolodziejcki
Chair of the Committee on Graduate Students

A Practical High Temperature Photonic Crystal for High Performance Thermophotovoltaics

by

Veronika Stelmakh

Submitted to the Department of Electrical Engineering and Computer Science
on May 18th, 2017, in partial fulfillment of the
requirements for the degree of
Doctor of Philosophy

Abstract

This work presents the first practical selective emitter for high performance thermophotovoltaics (TPV) that offers high optical performance, high temperature stability, and the ability to be fabricated in large area samples. In a TPV system, a heat source brings the photonic crystal emitter to incandescence, and the resulting thermal radiation drives a low-bandgap photovoltaic cell. The photonic crystal enables high efficiency by enhancing the radiation from the heat source in the wavelength range that can be converted by the photovoltaic cell and suppressing the radiation outside of that range. Our photonic crystal, composed of a square array of cylindrical cavities etched into a metallic substrate, enables unprecedented efficiencies in solar, radioisotope, and hydrocarbon TPV systems. We overcome multiple technical challenges previously limiting selective emitters by developing new fabrication processes to improve optical performance; by adopting commercial polycrystalline tantalum to fabricate large-area samples; by developing a HfO_2 passivation coating for improved thermo-chemical stability; and by developing a HfO_2 cavity filling process for improved omnidirectional performance.

More specifically, we developed a process for fabrication of uniformly patterned 50 mm diameter photonic crystals, integratable with virtually any heat source by brazing. Furthermore, we fabricated a photonic crystal in a sputtered tantalum coating, which can be directly sputtered onto a heat source. Our photonic crystal design reaches 67% of the performance of an ideal emitter. To further improve the omnidirectional performance, we fabricated a filled-cavity emitter, which experimentally demonstrated the theoretical prediction that HfO_2 -filled photonic crystals would have superior hemispherical in-band emissivity. Both fabricated photonic crystal designs were tested for 300 hours at 1000°C with no detectable degradation due to the passivation by HfO_2 . With our original design, we demonstrated the highest heat-to-electricity efficiency in a hydrocarbon TPV experiment to-date, exceeding 4% and greater than previous 2-3% efficiencies thought to be the practical limit. Furthermore, we expect from simulations that our filled photonic crystal design will enable over 12% efficiency with only engineering optimization. For reference, a 1.5% efficiency corresponds to the energy density of lithium ion batteries.

Thesis Supervisor: Dr. Ivan Celanovic

Title: Principal Research Scientist

To Larissa and Nikolai.

Acknowledgments

It takes a village to complete doctoral studies. I am thankful to everyone who made this work possible: my loving family, amazing friends, and wonderful colleagues. Without your encouragement and support in bright and dark times, it would not have been possible. I thank you all from the bottom of my heart. In particular, I would like to thank my mom Larissa for her unconditional love and support, my grandmother Veronika Sr. for inspiring me to be a scientist like her, and my grandparents Galina and Yuri for always telling me that I am the best at everything. I also know how proud my dad would be if he was still with us. I thank you, Papa, for inspiring me to always dream big and for passing on some of your work ethic to me.

I also would like to sincerely thank my advisors Ivan Celanovic, Marin Soljacic, and John Joannopoulos for their unwavering support over the years; committee members Leslie Kolodziejwski and Karl Berggren for providing insightful feedback; as well as Janet Fisher and the entire EECS Graduate Student Office. I was very lucky to find myself in a great lab, surrounded by wonderful people, over the course of my PhD program. I have many current and previous group members to thank: in particular, Walker Chan and Veronika Rinnerbauer for their support, mentorship, and friendship, without whom this thesis would not have been possible; Michael Ghebrebrhan and Adrian Y. X. Yeng for their tremendous help with simulations; Daniel Peykov for his help with substrate characterization; as well as all my other fellow past and present group members and collaborators Xiawa Wang, Jay Senkevich, Ognjen Ilic, Yichen Shen, David Bierman, Bo Zhen, Ling Lu, Scott Skirlo, Josue Lopez, to name a few. I also would like to thank Amy Tatem-Bannister, Marlisha McDaniels, Josh Freedman and the entire administrative team at the Institute for Soldier Nanotechnologies for tolerating my numerous requests.

This thesis would also not have been possible without the tremendous help I received over the years from all the cleanroom technical staff who took the time to train and support me, above and beyond their duties. In particular, I would

like to thank: Bob Geil (at CHANL, University of North Carolina at Chapel Hill) for his tremendous help and contributions in developing our process for the DRIE of tantalum; Jim Daley and Tim Savas (at NSL, MIT) for assistance with film deposition and interference lithography as well as emotional support in the cleanroom; Kurt Broderick (at EML, MIT) for assistance with sputtering and great company at all the MARC conferences; the technical staff of CNS, Harvard, Mac Hathaway and Austin Akey in particular, for very thorough training; Ronghua Wei, Robert Castillo, and Kent Coulter at Southwest Research Institute for tantalum sputtering; H.C. Starck for providing tantalum and tantalum 3% tungsten substrates and waterjetting of the Inconel substrates; Joshua Guske and Scott Speakman for assistance with XRD measurements (at CMSE, MIT); Libby Shaw for assistance with XPS and Auger measurements (at CMSE, MIT); Anna Osherov for assistance with the Cary 5000 (at CMSE, MIT); Christine Wang and Dan for assistance with zinc diffusion at Lincoln Laboratory; Davis Lee and Svetlana Radovanov with zinc implantation at Applied Materials; Steven Novak for assistance with SIMS (at CNSE, SUNY).

After my father suddenly passed away, at the end of my first year at MIT, I became a graduate resident tutor (GRT) at Maseeh Hall, which truly changed my life. I couldn't have completed my degree without the support of the Maseeh house team: Housemasters Suzanne Flynn and Jack Carol, Associate Housemasters Cullen and Donielle Buie, Area Director Rebecca Kjaerbye, and fellow GRTs. I especially want to extend my gratitude to my fellow GRTs Sebastian Schmidt and Mitali Thakor for their love and support. I also want to thank the amazing *Quantum Girls* for their amazing friendship, support, and inspiration throughout graduate studies at MIT: Nivedita Chandrasekaran, Sara Mouradian, Clarice Aiello, Valentina Schettini, and Maria Tengner. Many thanks also to my undergraduate studies advisor and friend Michael Vasilyev for his tremendous support and encouragement, especially at the beginning of this PhD program.

Last but certainly not least, I would like to thank Marilyn Levine at the MIT Writ-

ing Center for not just proof-reading and editing my dissertation, but also providing me with the emotional support required to finish writing this document.

Contents

1	Introduction	21
1.1	Thesis Motivation	21
1.2	Low Bandgap Photovoltaic Cells	25
1.3	Spectral Control for High System Efficiency	28
1.3.1	Cold Side Filters	28
1.3.2	Selective Emitters	28
1.3.3	Optical Performance	30
1.3.4	High temperature stability	32
1.3.5	Large area fabrication and system integration	34
1.4	Emitters Comparison	35
1.5	Our Photonic Crystal Selective Emitter	36
1.6	Summary of Contributions	39
1.7	Thesis Organization	40
2	Design	43
2.1	Analytical Modeling	45
2.1.1	Cavity Resonance Approach	45
2.1.2	Q-Matching Approach	46
2.2	Numerical Modeling	48
2.2.1	Simulation	48
2.2.2	Optimization	49

3	Large Area Photonic Crystal Fabrication	53
3.1	Substrate Preparation	56
3.2	Nanofabrication	58
3.2.1	Etching Layers	58
3.2.2	Interference Lithography	59
3.2.3	Pattern Transfer	60
3.3	Substrate Etch	62
3.4	Surface Passivation	63
3.5	Impact of Nanofabrication Improvements on Performance	66
4	Optical Performance and Thermal Stability	69
4.1	Optical Measurements	70
4.1.1	Room Temperature Measurement	71
4.2	Characterization	74
4.2.1	High-Temperature Measurement	76
4.3	Morphology	77
5	Omnidirectional Emissivity Improvement	79
5.1	Physics and Design	79
5.2	Fabrication and Characterization	81
6	System Integration	87
6.1	Integration by Sputtering	87
6.2	Integration by Welding and Brazing	91
7	Conclusion	97
7.1	Emitter Comparaision	97
7.2	Impact of this work	101
7.3	Summary of Key Contributions	102
7.4	Future Work	103

<i>CONTENTS</i>	13
A TPV Chronology	105
B Tantalum Substrates Characterization	109
B.1 Unpassivated Polished Tantalum	110
B.2 Passivated Tantalum	113
C Sputtered Metallic Coatings	117
C.1 Tungsten on Silicon Substrates	118
C.1.1 Summary	127
C.2 Tantalum on Inconel Substrates	128
C.2.1 Summary	136
C.3 Optical Performance	138
D Custom Codes	143
D.1 Reflectance Calibration	143
D.2 Geometric Parameter Fitting	144
D.3 Hot Side Model	144

List of Figures

1-1	New technologies are needed to harness the energy of hydrocarbon fuel in the 1–100 W range.	22
1-2	Hydrocarbon TPV conversion process using a photonic crystal selective emitter	23
1-3	In TPV, the radiation from the emitter then drives a low bandgap PV cell thereby generating electricity.	26
1-4	Evolution of solar PV cells.	27
1-5	Main requirements of a practical TPV selective emitter.	29
1-6	Comparison of the emittance of various selective emitters.	31
1-7	Hemispherically averaged emissivity comparison of ideal, blackbody, natural (erbia), and engineered (1D and 2D) selective emitters.	32
1-8	Main requirements for a practical TPV selective emitter.	35
1-9	Our photonic crystal selective emitter design consists of a square array of cylindrical cavities etched into a metallic substrate.	37
1-10	Photonic crystal design, fabrication, characterization, and integration process flowchart.	42
2-1	The primary influence the geometric parameters in the photonic crystal design.	44
2-2	One period of the photonic crystal structure.	45

2-3	Numerical simulation of an optimized photonic crystal compared with the analytically calculated lowest frequency mode of a single cavity.	47
2-4	Geometric parameters, radius r and period a , optimized for cutoff wavelengths λ_c ranging from 1.4 to 2.6 μm	51
3-1	The general process flow for the fabrication of our 2D photonic crystal selective emitter	53
3-2	The evolution of the substrates over the course of this work, from single crystal tungsten to large tantalum wafers.	55
3-3	Ultimate tensile strength, yield strength, percent elongation, and Young's modulus of tantalum-tungsten alloys.	57
3-4	Tri-layer stack optimization.	59
3-5	Schematic of Mach-Zehnder interferometer used in interference lithography.	61
3-6	A general process flow for the photonic crystal fabrication.	63
3-7	SEM of Si test piece after each fabrication step.	64
3-8	SEM of Si test piece after DRIE.	65
3-9	Improvements over the course of this work, from wet etching of Cr mask to RIE of SiO_2 mask.	67
3-10	Effect of cavity roughness on emissivity.	67
4-1	Effect of HfO_2 coating on cutoff wavelength.	71
4-2	HfO_2 -passivated photonic crystal emission before and after anneal.	72
4-3	FIB cross section of HfO_2 -passivated photonic crystal.	73
4-4	Emissivity measurements from 300 hour stability test.	73
4-5	Measured and simulated emittance of different fabricated photonic crystals.	75
4-6	High temperature emission measurements.	77
4-7	SEM and AES images of a photonic crystal with and without HfO_2	78

5-1	Emittance of filled and unfilled photonic crystals over θ and ϕ	80
5-2	SEM micrographs of filled photonic crystal.	82
5-3	Normal and 45° incidence measurements and simulations.	83
5-4	Effect of surface HfO ₂ layer on optical performance.	84
5-5	Effect of Ar etch back on emittance.	85
5-6	Filled photonic crystal after Ar etch back.	85
6-1	Schematic representation of a photonic crystal fabricated in tantalum sputtered directly on Inconel.	88
6-2	SEM micrograph of photonic crystal fabricated in sputtered tantalum.	88
6-3	Emittance of sputtered photonic crystal.	90
6-4	Welded photonic crystal before and after running burner at 900°C.	91
6-5	TPV system with brazed photonic crystal.	92
6-6	Measured and simulated electrical power output as a function of fuel flow.	94
7-1	Main requirements for a practical TPV selective emitter.	99
7-2	Simple modeling comparison of emitters from literature.	100
B-1	Passivated and unpassivated tantalum before and after annealing.	112
B-2	Auger analysis of tantalum surfaces.	115
B-3	Reflectance of passivated and unpassivated tantalum for different annealing times.	116
B-4	Unpassivated tantalum grain size as a function of annealing time at 900°C.	116
C-1	AFM and SEM images of unannealed sputtered tungsten.	120
C-2	Reflectance of sputtered tungsten before and after annealing.	121
C-3	AFM and SEM images of sputtered tungsten before and after annealing.	123
C-4	XRD data for sputtered tungsten.	124

C-5	FWHM and microstrain of sputtered tungsten.	126
C-6	Reflectance and roughness of sputtered tantalum.	130
C-7	Reflectance of sputtered tantalum before and after anneal.	132
C-8	XRD data for sputtered tantalum.	133
C-9	Pole figures for sputtered tantalum.	133
C-10	Residual stress of sputtered tantalum before and after anneal.	134
C-11	Spectral selectivity and power density for photonic crystals and flat tantalum.	139
C-12	Spectral efficiency and in-band emissivity for a photonic crystal and flat tantalum.	141
D-1	Reflectance calibration.	145
D-2	Fitting of parameters of the photonic crystal with 1.7 μm cutoff.	146
D-3	Fitting of parameters of the photonic crystal with 2.0 μm cutoff.	147
D-4	Fitting of parameters of the photonic crystal with 2.3 μm cutoff.	148
D-5	Microburner model.	150

List of Tables

1.1	Experimentally demonstrated TPV systems enabled by our photonic crystal selective emitter.	25
2.1	Dimensions of the 2D photonic crystal parameters optimized by NLOpt for different TPV cells and their respective cutoff wavelengths.	50
3.1	Improvements made for each fabrication step.	55
3.2	Parameters used during the RIE and DRIE processes to etch the tantalum using a chromium or SiO ₂ mask.	63
3.3	Parameters used during the HfO ₂ ALD process using TDMAH precursor to conformally coat the cavities of the photonic crystal.	66
4.1	Optical and geometric parameters of selected fabricated photonic crystals.	74
5.1	Parameters used during the HfO ₂ ALD process using TDMAH precursor to fill the cavities of the photonic crystal.	81
6.1	Simulated heat flow within TPV system.	95
7.1	Comparison optical performance, thermal stability, and size to literature.	101
A.1	Thermophotovoltaics chronology: early developments.	106
A.2	Thermophotovoltaics chronology: improving low bandgap TPV cells.	107

A.3	Thermophotovoltaics chronology: improving spectral control.	108
C.1	X-ray elastic constants of tantalum	129
C.2	Efficiency and power density comparison at 1500K.	139
C.3	Spectral efficiency and in-band emissivity of different emitters.	142

Chapter 1

Introduction

1.1 Thesis Motivation

The advances in high temperature photonic crystals described in this thesis enable a practical high efficiency thermophotovoltaic (TPV) system which in turn can meet the burgeoning demand for portable power: drones, robots, and soldier power for example. This demand is pushing current technologies to their limit, and challenging new technologies to sustain the demand in particular for applications in the 1–100 W range at the mesoscale (characteristic length on the order of millimeters). Indeed, unconventional and fundamentally different energy conversion methods are required at this scale because the vastly different length scales compared to conventional generators result in different geometric scaling (e.g., surface area to volume ratio) and different phenomenological behavior (e.g., laminar and turbulent flow) [1]. Indeed, hydrocarbon fuels offer very high energy density (~ 12 kWhr/kg) so that even a relatively inefficient generator can exceed the performance of state of the art batteries (200 Whr/kg). As shown in Figure 1-1, researchers have investigated a number of different technologies: mechanical approaches such as microturbines [2] and Wankel engines [3, 4], electrochemical approaches such as solid oxide or direct methanol fuel cells [5, 6], to thermal approaches such as thermoelectrics [7, 8] and

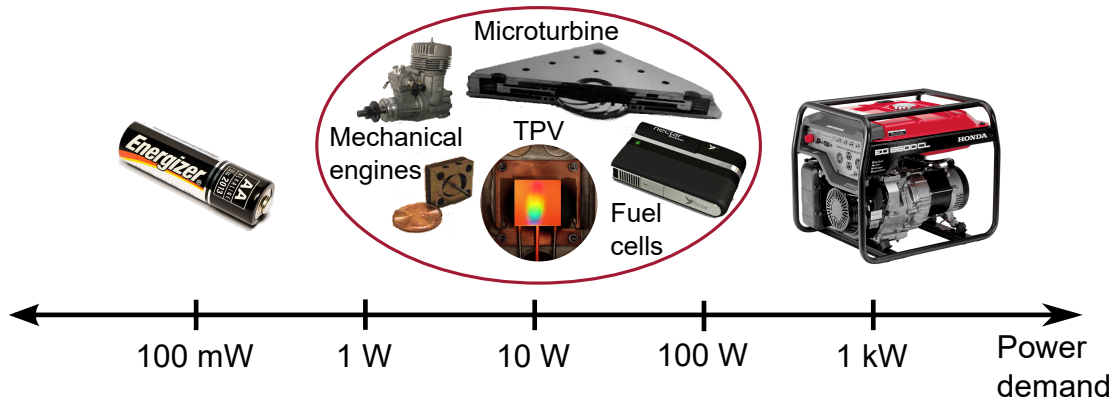


Figure 1-1: New technologies are needed to sustain the power demand in applications in the 1–100 W range. Indeed, while batteries are ubiquitous in the portable power space, their energy density is approaching its theoretical limit [12]. Hydrocarbon fuels offer very high energy density (~ 12 kWhr/kg) so that even a relatively inefficient generator can exceed the performance of state of the art batteries (200 Whr/kg). While diesel generators are very efficient, relative to smaller solutions, their size is limited by physics and cannot be reduced past a point that is still too bulky for portable applications because of scaling laws associated with internal combustion engines [13].

thermophotovoltaics [1, 9–11], but until now, all of these technologies have presented many challenges. Micro-mechanical engines are subject to frictional losses. Electrochemical systems have fuel utilization limitations and are subject to poisoning by impure fuels and require extensive balance-of-plant systems. All thermal solutions are limited by materials available for high operational temperatures and low efficiencies demonstrated to date. This thesis presents an approach to overcome these challenges, making TPV, hydrocarbon TPV in particular, a promising alternative technology for portable power.

As shown in Figure 1-2, in a hydrocarbon TPV energy conversion system, combustion heats an emitter to incandescence and its thermally radiated photons are converted into electricity via photovoltaic cells. There are three critical elements required to achieve the impressive efficiencies predicted by theoretic models for TPV energy conversion:

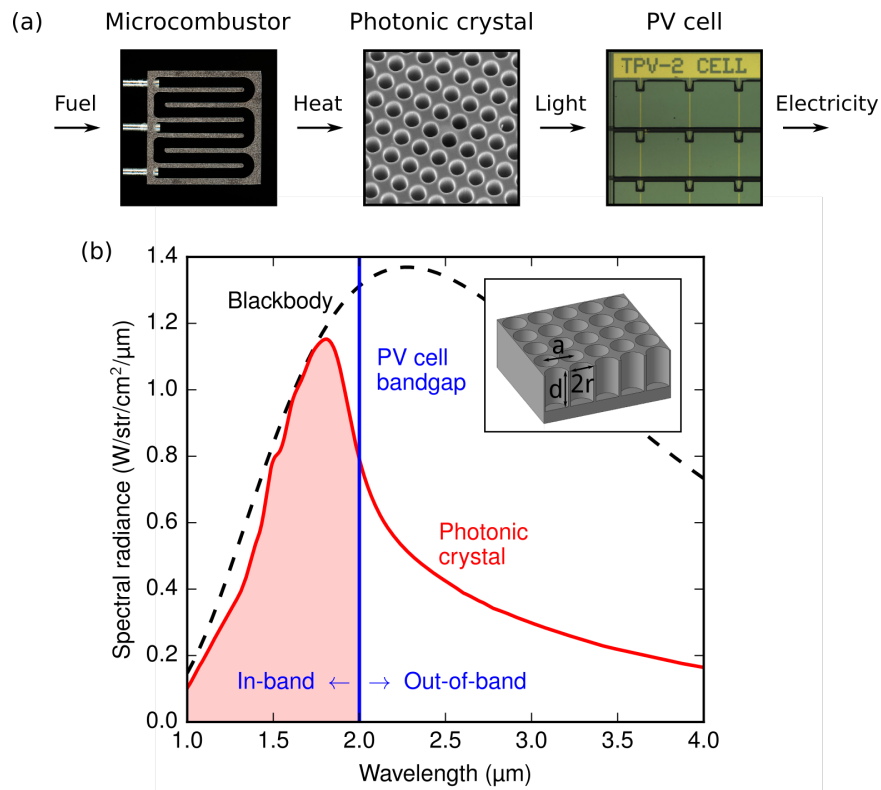


Figure 1-2: (a) Hydrocarbon TPV conversion process using a photonic crystal selective emitter. Only the photons below the cutoff wavelength (*i.e.* energy above the bandgap) of the PV cell can be converted to electricity. The photons above the cutoff wavelength are not only wasted, they lower the overall efficiency of the system and heat up the cell. The photonic crystal enhances the emission in the in-band region and suppresses the emission in the out-of-band region shown in (b).

- A **high-temperature heat source** drives the selective emitter. Heat sources include combustion, radioactive decay, and solar energy.
- A **selective emitter** tailors the emission and can operate at high temperatures.
- A **low bandgap PV cell** converts the thermal radiation into electricity with high efficiency.

Scientific and technological advancements over the past 70 years, since the technology was proposed, in high-temperature ($>1000^{\circ}\text{C}$) heat sources, selective emitters, and low bandgap semiconductor materials have paved the way towards unprecedented TPV efficiencies [14] and spurred new interest, as described in detail in Appendix A. However, no practical system has been realized or commercialized because no practical high performance selective emitter has existed until now, as described in this thesis.

Our approach is unique and enables practical system implementation by utilizing a novel superalloy microcombustor [1] as the heat source, a metallic high-temperature 2D photonic crystal for spectral control, and high efficiency advanced low bandgap III-V TPV cells for converting the thermal radiation to electricity. Using the proper spectral control and efficient cells, a system efficiency exceeding 20% is attainable in a small form factor [15]. Thus, harnessing the energy content of hydrocarbon fuels on the mesoscale should pave the way to transformative increases in portable power generation. Furthermore, our approach to TPV can be applied to other heat sources such as solar energy and radioactive decay, as shown in Table 1.1.

TPV offers some advantages over batteries and other microgenerator technologies for mesoscale power. The static conversion process does not fundamentally require moving parts. High power density results in a compact microgenerator. It also offers advantages over other static heat to electricity conversion technologies, i.e. thermoelectrics or thermoionics: the hot and cold sides are physically separate; only the burner and emitter need to be at high temperatures. The difficult conversion to

Table 1.1: Experimentally demonstrated TPV systems enabled by our photonic crystal selective emitter.

System	Heat source	Emitter	Cell	Ref.
Combustion	Microcombustor	Photonic crystal	InGaAs	[1]
Solar	Solar absorber	Photonic crystal	InGaAsSb	[16]
Radioisotope	Electrical heater	Photonic crystal	InGaAsSb	[17]

electricity is accomplished separately on the cold side, independently. Furthermore, there are no fundamental temperature gradients across materials which cause thermal stresses during startup and operation. High temperature continuous combustion (as opposed to discontinuous combustion in a piston engine) allows for efficient fuel utilization and low emissions, high power density, multi-fuel operation, and the ability to use conventional fuels such as gasoline, diesel, JP-8, as well as biofuels.

1.2 Low Bandgap Photovoltaic Cells

The low bandgap photovoltaic (PV) cell, also referred to as TPV cell, converts the thermal radiation to electricity. These cells operate on the same principle as solar PV cells, however the incident radiation is of longer wavelength and higher intensity than the solar spectrum, as shown in Figure 1-3, necessitating low bandgap semiconductors for efficient conversion. While typical solar PV cells have a band gap $E_g=1.1$ eV, typical TPV cells have $E_g=0.68$ eV for GaSb [18], 0.62 eV for InGaAs [19], and 0.54 eV for quaternary InGaAsSb cells [20]. As shown in Figure 1-3, each one of these bandgaps correspond to an optimum operating temperature, ranging from about 1000 to 1400°C illustrated by a blackbody at that temperature. Compared to solar PV cells, low bandgap PV cells remain in their infancy, and we can expect a doubling of efficiency if development follows the same trajectory as for solar PV, shown in Figure 1-4.

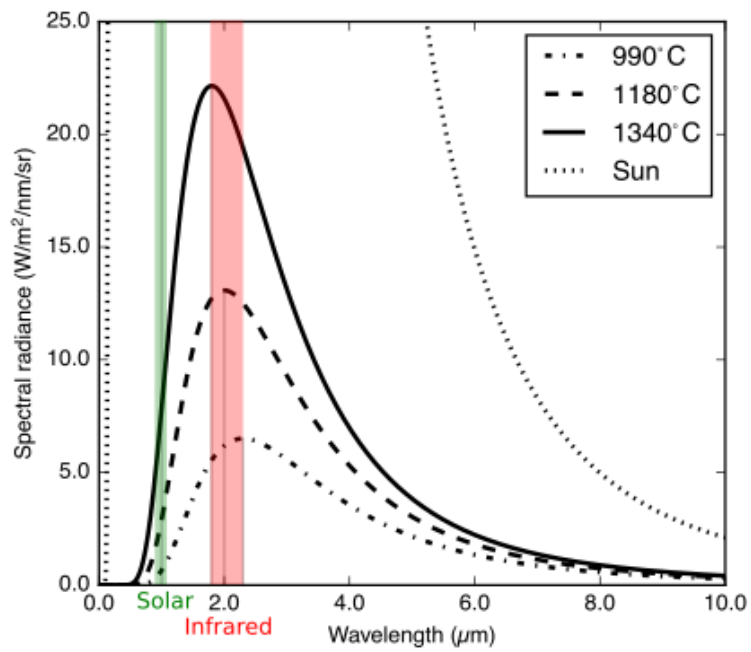


Figure 1-3: In TPV, the radiation from the emitter then drives a low bandgap PV cell thereby generating electricity. A blackbody at $\sim 990^{\circ}\text{C}$ matches the bandgap of GaSb ($1.8\ \mu\text{m}$), a blackbody at $\sim 1180^{\circ}\text{C}$ matches InGaAs ($2.0\ \mu\text{m}$), and a blackbody at $\sim 1340^{\circ}\text{C}$ matches InGaAsSb ($2.3\ \mu\text{m}$). For comparison, the bandgap of Si ($1.0\ \mu\text{m}$) is matched to the solar spectrum which corresponds to $\sim 5500^{\circ}\text{C}$.

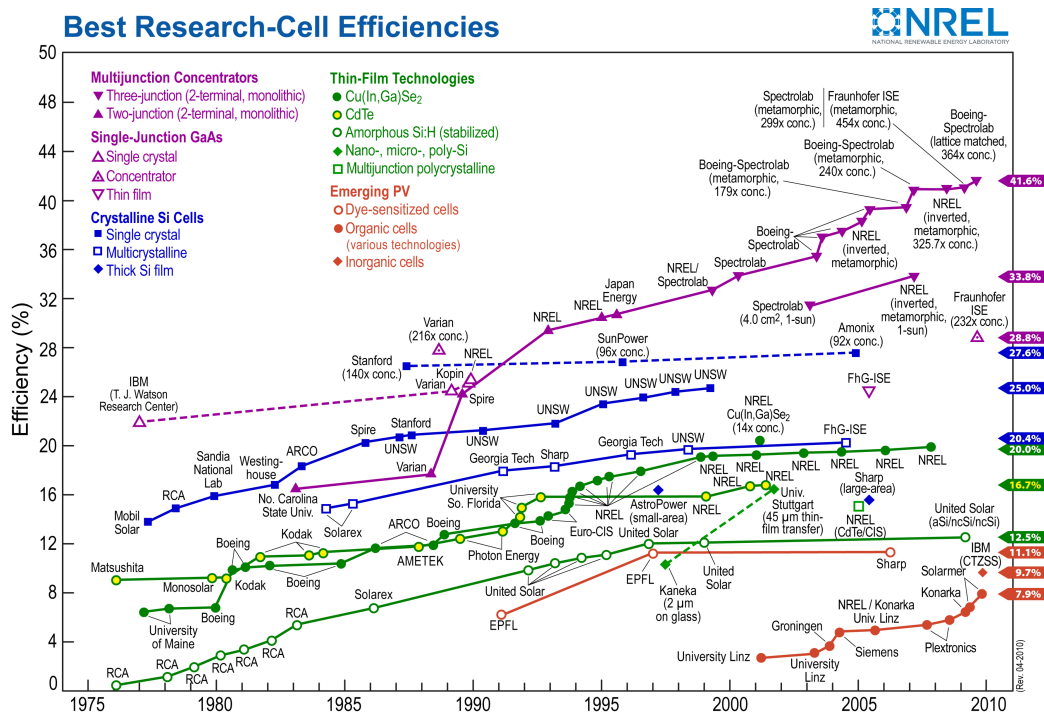


Figure 1-4: Evolution of solar PV cells. While solar PV cells have been studied and optimized since the Seventies, TPV cells remain in their infancy. Looking at the progress made in solar cells, it can be inferred that similar improvements in efficiencies could be made in low band gap PV cells. Silicon PV cells have been investigated for TPV applications as well [21]. (Data compiled by Lawrence Kazmerski, National Renewable Energy Laboratory (NREL). Licensed under Public domain via Wikimedia Commons.)

1.3 Spectral Control for High System Efficiency

Generally, there are two approaches to spectral control: using a cold side optical filter to pass a portion of the light to the cell while reflecting the rest back to the emitter and using a selective emitter to directly tailor the emission spectrum. In this work, we focus on direct control of the emission spectrum using a selective emitter because of the difficulty in achieving a sufficiently low loss optical cavity to make a viable cold side filter.

1.3.1 Cold Side Filters

Historically, cold side filters have been used with a blackbody emitter as an alternative to selective emitters. Although simple interference filters can be used [22], the large stop band of $\sim 10 \mu\text{m}$ required for effective photon recycling is better covered by a tandem combination of an interference filter and a plasma filter [23–25] or micro-resonator frequency selective surface [26]. In addition to the experimental difficulties associated with the large stop band (>50 layers, exotic materials), the approach had limited applicability to TPV microgenerators because of the high required cavity efficiency thus placing severe restrictions on the view factor and the acceptable loss or out-of-band transmission of the filter. The cold side filter can help increase the efficiency of a TPV system that already uses a selective emitter. However, on its own, it is too lossy, due to the large amount of circulating radiation.

1.3.2 Selective Emitters

A system using a selective emitter instead of a cold side filter does not need a low loss cavity, which is hard to achieve, but the selective emitter does need to operate at high temperatures, which presents a different set of challenges. As shown in Figure 1-8, a *practical* TPV selective emitter should have:

1. Good optical performance, defined in terms of high in-band emissivity and low

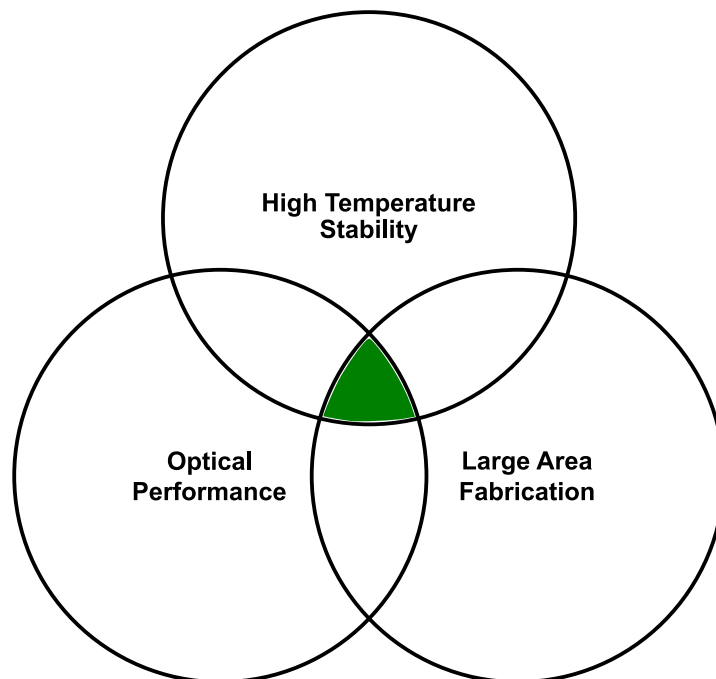


Figure 1-5: A practical TPV selective emitter should meet the three main requirements: (1) Optical performance, (2) High temperature stability, and (3) Large area fabrication and integration.

out-of-band emissivity.

2. High temperature stability, defined in terms of lack of degradation in emissivity after anneal.
3. Large area fabrication, defined by the fabricated sample size, and integration with the full system.

Many approaches to selective emitters have been investigated but none have met all the criteria and therefore were not viable solutions. Historically, natural materials were used as selective emitters for TPV applications. Rare earth emitters, such as ytterbium for example, were easy to fabricate and could sustain very high temperatures; however they did not provide sufficiently good optical control to enable high TPV energy conversion efficiency, as shown in Figure 1-6. Engineered materials, photonic crystals in particular, emerged as a potential solution as they could tailor the spectral emission much more effectively.

1.3.3 Optical Performance

The optical performance of a selective emitter is defined by its emittance. An ideal selective emitter has unity in-band emissivity and zero out-of-band emissivity, with a sharp drop-off between the two regions. This spectrum would correspond to a maximum in-band emissivity, and in turn, maximum radiative power, as shown in Figure 1-6(a). Natural selective emitters, such as ytterbia, and previously engineered selective emitters such as the 1D Si/SO₂ stack, never reached the level of in-band radiative power that our 2D photonic crystal has achieved, as shown in Figure 1-6.

As shown in Figure 1-7, we compare the hemispherically averaged emissivity of an ideal selective emitter (unity in-band emissivity and zero out-of-band emissivity), a ytterbia natural selective emitter, Si/SiO₂ 1D stack engineered multilayer selective emitter [11], and our 2D tantalum photonic crystal design [27]. Our 2D photonic crystal design exceeds the performance of all the other selective emitters, enabling

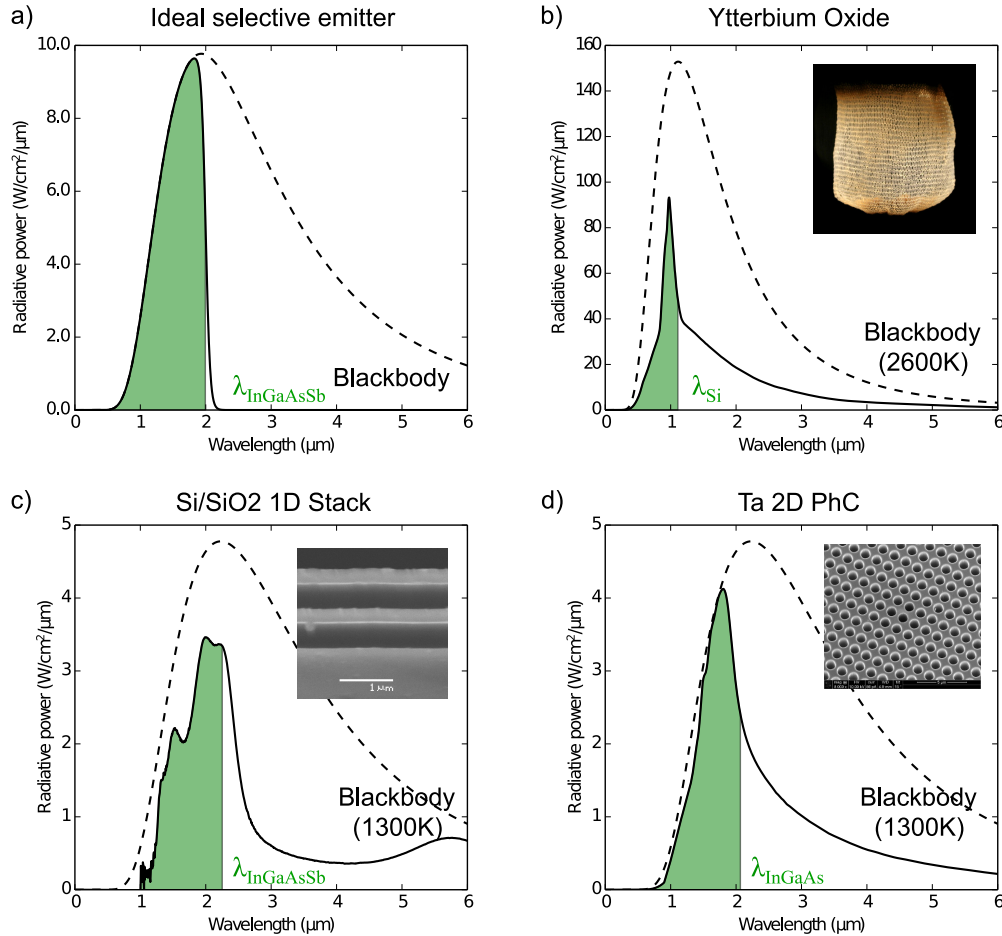


Figure 1-6: (a) Ideal selective emitter (unity in-band emissivity and zero out-of-band emissivity), (b) ytterbia natural selective emitter, (c) Si/SiO₂ 1D stack engineered selective emitter, and (d) tantalum 2D photonic crystal selective emitter compared with a blackbody at the same temperature. The convertible region of the matched semiconductor is highlighted.

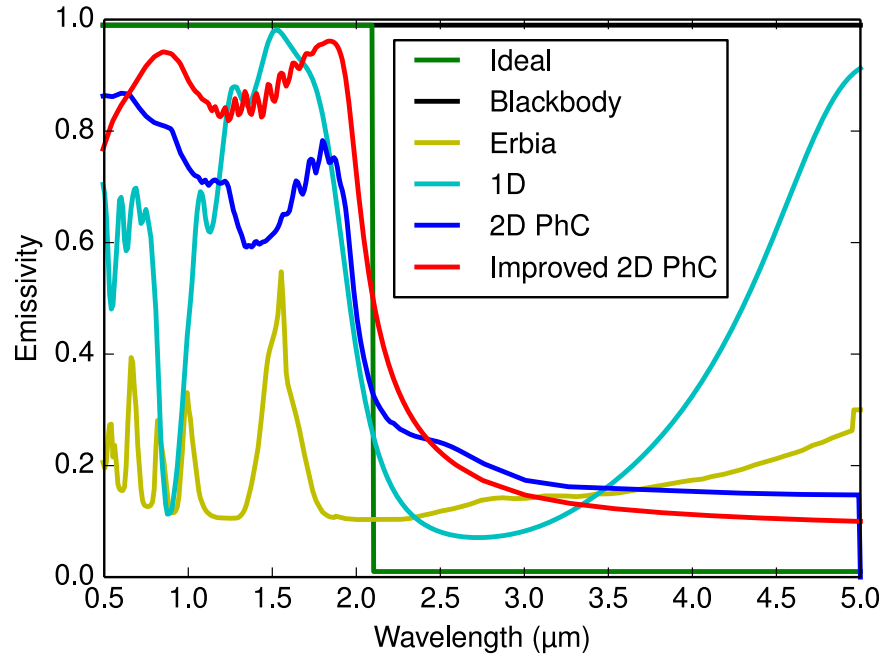


Figure 1-7: Hemispherically averaged emissivity comparison of ideal, blackbody, natural (erbium), and engineered (1D and 2D) selective emitters.

higher system efficiencies by tailoring the spectrum of the radiation to match the bandgap of the TPV cell.

1.3.4 High temperature stability

The high temperature performance of the selective emitter—stability for long durations at high temperatures—is of the utmost importance in a real TPV system. Natural selective emitters were chosen initially for TPV applications due to their very robust thermal stability. Oxides such as Yb_2O_3 and Er_2O_3 have been operated at 1462 and 1407°C respectively [28] without degradation, however as previously mentioned, their optical performance was not sufficiently good. Engineered selective emitters, which offer better optical performance, are typically fabricated in refractory metals such as tungsten or tantalum in order to sustain sustain the high operational temperatures. While refractory metals are well suited due their extremely high melting points (3017 and 3422°C for tantalum and tungsten, respectively), the long term

high-temperature stability of the photonic structure is never investigated past a few hours in literature. However most metallic structures have been suspected to degrade through a wide range of phenomena:

- Surface diffusion and vapor transport (evaporation condensation) can produce a rounding and smoothing of the surface [29–36], which has been linked to a gradual reduction in the efficiency of the emitter [37].
- Grain growth [29–32, 34, 36, 38–40] in polycrystalline substrates.
- Thermal cracking and delamination due to stress, observed in [33, 35] and explored in greater detail in [40, 41].
- Chemical degradation, including the oxidation of tungsten substrates [29, 31, 34, 36] and the formation of carbon-based agglomerates on tantalum [27, 38, 42], detrimental to the optical properties of these materials due to an increase in both their surface roughness and long-wavelength emissivity.

To overcome degradation, a number of different approaches have been proposed including the use of large grained or single crystal substrates to prevent grain growth [27, 38, 39, 43], alloying to promote a solute drag effect [31, 32, 34], improved vacuum conditions to prevent reactions with trace contaminants [31, 34, 36], as well as changes to the structure geometry to affect diffusion rates [36, 37]. Our approach involves the deposition of a conformal protective coating which serves to limit both the reactivity and the diffusivity of the metallic photonic crystal surface. Finding a coating that works for all the TPV requirements was one of the challenges of this work. Indeed, different chemically inert compounds, such as Al_2O_3 [33] or HfB_2 [35], have been attempted in the past. However HfO_2 , hafnia, has been the most promising thus far at preventing degradation and preserving optical properties [27, 29, 33, 35, 36, 38, 39, 42].

1.3.5 Large area fabrication and system integration

Thermophotovoltaic systems have a power density of about $0.5\text{--}1\text{W}/\text{cm}^2$. In order to meet the specified electrical power output, the emitter must be $\sim 10\text{ cm}^2$, necessitating the ability to fabricate large-area photonic crystals. Most of the approaches shown in Figure 1-8 have only been experimentally demonstrated on very small emitter areas, on the order of millimeters. While the natural selective emitters and 1D stack emitters have been realized in practical system sizes, their optical performance is not good enough. Emitters fabricated from single crystal tungsten have good optical performance but are limited in size due to the single crystal nature. In this work, we adopted commercial poly-crystalline tantalum to fabricate large-area samples. Furthermore, our photonic crystal is fabricated by standard nanofabrication processes which enable large area fabrication. We have demonstrated an emitter as large as 2 inches in diameter, and could easily scale to 6-inch wafers.

Once the photonic crystal is fabricated, the challenge remains to integrate it into a compact system operating at high temperatures. Most of the approaches shown in Figure 1-8 have never been integrated with a heat source, except for natural emitters and the 1D stack, which have unsatisfactory optical performance. Our photonic crystal was integrated by brazing to the Inconel microburner, enabling unprecedented efficiency.

Another integration method was also developed. Generally, spectral components are fabricated from bulk substrates and are welded on the source of heat, limiting substrate materials. Using a tantalum coating, for example, as a functional layer on different substrates, selected and matched to the system's needs, decouples the requirements of the functional layer and the substrate. Thick tantalum coatings were sputtered on polished Inconel 625, which is a readily available low-cost nickel-chromium-based superalloy used in many high-temperature applications and were found to be suitable for photonic crystal fabrication [40].

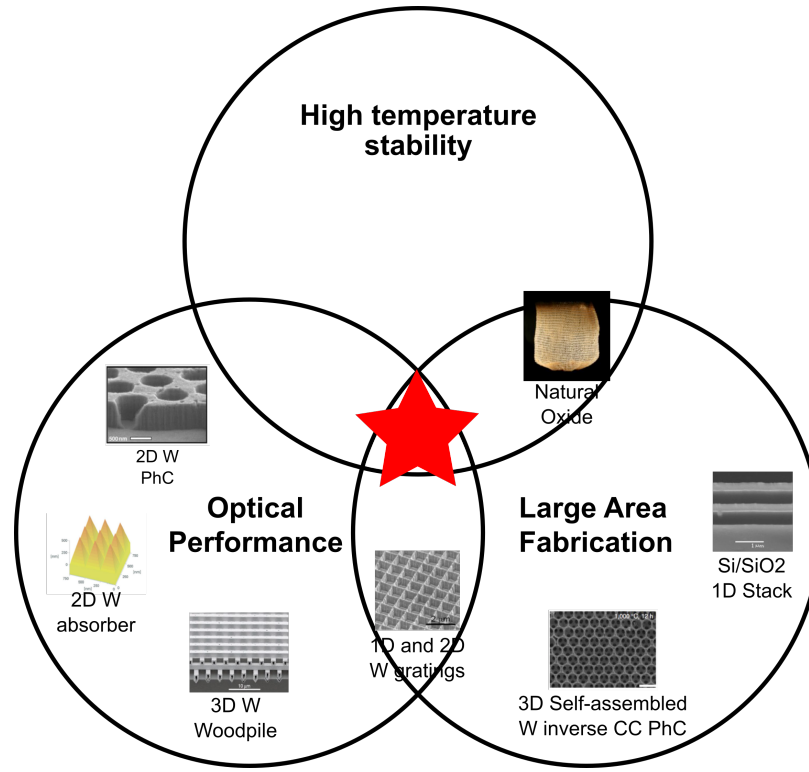


Figure 1-8: There are three main requirements for a practical TPV selective emitter: (1) Optical performance, (2) High temperature stability, and (3) Large area fabrication and integration. Photonic crystals fabricated as 1D, 2D, and 3D structures or metamaterials [33,42,44–47] enable higher system efficiencies by tailoring the photonic density of states to produce spectrally confined selective emission of light [30,48–50]. None of these approaches to selective emitters meet all the criteria for a practical TPV selective emitter.

1.4 Emitters Comparison

Photonic crystals are periodical structures, analogous to semiconductors in that they have allowed and forbidden states. Photonic crystals fabricated as 1D, 2D, and 3D structures or metamaterials [33,42,44–47] enable higher system efficiencies by tailoring the photonic density of states to produce spectrally confined selective emission of light [30,48–50]. One dimensional dielectric stack Si/SiO₂ photonic crystals exhibit omni-directional bandgap [51]. They are relatively easy to fabricate but have neither the high temperature performance, nor the optical performance required, in

the long wavelength particularly. Two-dimensional [35] and three-dimensional photonic crystals [52] refractory metal photonic crystals exhibit resonant enhancement and often tunable cut-off, thus generally offering a good optical performance, but are difficult to fabricate in large areas, and typically cannot sustain very high temperatures for long operational times required by TPV systems. Furthermore, most of the work on nanophotonics and photonic crystals in general is focused on room- and cryogenic-temperature operation, and a very limited body of work has explored the application of nanophotonics for solid-state energy conversion. Our practical selective emitter meets the requirements of optical performance, thermo-mechanical stability, large area fabrication, and system integration with our microburner. Our fabrication process is simple, scalable, and achievable with standard semiconductor process.

1.5 Our Photonic Crystal Selective Emitter

Our 2D photonic crystal consists of a square array of cylindrical cavities with radius r , period a , and depth d etched into the substrate, as shown in Figure 1-9(inset). Tantalum is a suitable substrate for high-temperature energy applications because it has high long-wavelength reflectance as well as a high melting point and low vapor pressure. The absorptivity of the substrate material is selectively enhanced by the introduction of cavity modes. The spectral range of enhancement can be tailored to the specific system needs by tuning the geometric parameters of the cavities, as shown in Figure 1-9.

Our 2D photonic crystal design exhibits exceeds the performance of other selective emitters, having a desired high in-band and low out-of-band emittance, as shown in Figure 1-7 where we compare the hemispherically averaged emittance of the Si/SiO₂ 1D stack stack [11], our 2D photonic crystal design (current design [27] and improved filled 2D photonic crystal design [53, 54]), a natural erbia emitter [55], and a black-body emitter, with an ideal emitter (step function). Our simple hafnia-coated 2D

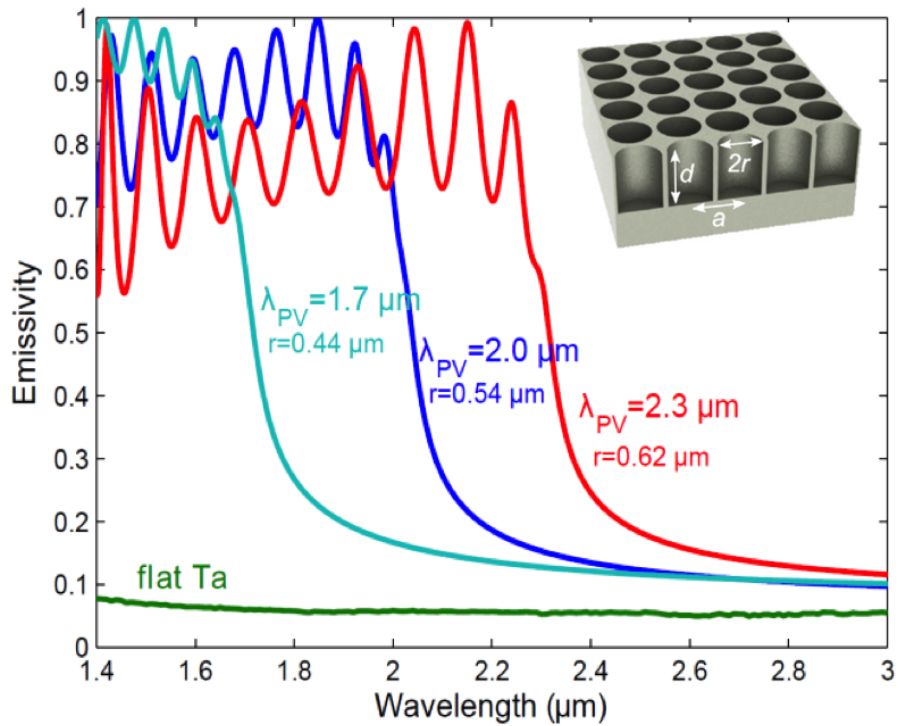


Figure 1-9: Our photonic crystal design consists of a square array of cylindrical cavities etched in a metallic substrate such as tantalum. The cutoff wavelength can be easily tailored to the specific system needs by tuning the geometric parameters of the cavities. Inset shows the 2D photonic crystal's square array of cylindrical cavities with radius r , period a , and depth d [38].

photonic crystal allows us to experimentally realize 67% of the ideal selective emitter limit of a combustion driven TPV system. Our improved filled-cavity photonic crystal further increases the hemispherical in-band emissivity and should be able to achieve 73% of the ideal emitter limit.

The thermal stability of our photonic crystal is also superior. The structure itself is very robust with minimum surface diffusion, vapor transport, and grain growth due to the metallurgical quality of the bulk substrate and simple geometry with low radius of curvature. The conformally deposited hafnia coating acts as a passivation layer on the surface of the photonic crystal to prevent degradation of the structure due to diffusion and the formation of tantalum carbides which lower the reflectance. Thermo-mechanically, the coating is stable at temperatures as high as 1200°C [41]. We found both conformally coated and filled-cavity emitters to be stable for as long as 300 hours at 1000°C with no degradation.

The fabricated photonic crystal size was as large as 2 inch wafers and samples were successfully integrated with the heat source by brazing and sputtering. Furthermore, our photonic crystal is fabricated using standard semiconductor processes, that are repeatable and scalable. The pattern is defined by interference lithography and transferred by deep reactive ion etching into the metallic substrate. The conformal passivation layer is deposited by atomic layer deposition.

Its great optical performance, combined with its high-temperature stability, its sample size matching the burner, and its integration by brazing or sputtering, makes our 2D photonic crystal selective emitter the most practical and viable emitter for TPV applications to date. Indeed, our fabricated bulk tantalum 2D photonic crystal with a 20 nm conformal hafnia coating enabled an experimentally demonstrated record fuel-to-electricity 4.5% system efficiency in a hydrocarbon TPV system. For comparison, a 1.5% fuel-to-electricity conversion efficiency corresponds to the energy density of lithium ion batteries. With small improvements to the burner, reducing the emissivity of the edges, a fuel-to-electricity efficiency of 7.6% is predicted at 100 W of

fuel input, using the same photonic crystal. With an improved filled-cavity photonic crystal, in addition to low emissivity edges, a fuel-to-electricity efficiency of 12.6% is predicted at 100 W of fuel input, which is several times higher than heat-to-electricity conversion methods previously reported [1], and paves the way for small scale portable power generation.

1.6 Summary of Contributions

Our fabricated bulk tantalum 2D photonic crystal with a 20 nm conformal hafnia coating enabled an **experimentally demonstrated record fuel-to-electricity 4.5% system efficiency in a hydrocarbon TPV system.**

- *Improved spectral selectivity by optimizing fabrication process:* New tantalum etch mask was developed: SiO₂ instead of the previously used chromium. The mask further minimized emission in the long wavelengths (previously due to residue from leftover chromium etch mask). Our photonic crystal design reaches 67% of the optical performance of an ideal emitter
- *Developed a passivation coating to prevent high temperature degradation:* The deposition of a conformal thin layer of HfO₂ as a thermal barrier preserved the PhC's outstanding emittance selectivity, even after annealing for 24 hours at 1200°C and 300 hours at 1000°C, demonstrating that the coating effectively prevents degradation due to surface diffusion at high temperatures.
- *Enabled system integration by developing a tantalum-tungsten alloy substrate material for photonic crystal fabrication:* A tantalum-tungsten (Ta-W) solid solution alloy photonic crystal was demonstrated as a spectrally selective emitter. The Ta 3% W alloy presented critical advantages compared to non-alloys as it combined better thermo-mechanical properties of tungsten with the more

compliant material properties of tantalum, allowing a direct system integration path.

- *Investigated two sputtered coatings, tungsten and tantalum, as a substrate for 2D photonic crystal fabrication:* The optical properties and thermo-mechanical stability of the coatings were characterized and the tantalum sputtered coating was found to be a suitable substrate as no cracking or delamination occurred.
- *Fabricated a 2D photonic crystal in sputtered tantalum:* The optical performance and thermal stability were characterized, enabling a new level of system integration which would benefit all high-temperature TPV systems. In the hydrocarbon microcombustor application, the photonic crystal can be sputtered directly on the burner minimizing heat losses and increasing efficiency. In STPV applications, the photonic crystal coating can also be applied as an absorber/emitter.
- *Fabricated an improved photonic crystal structure to enhance hemispherical emissivity:* A filled-cavity 2D photonic crystal in bulk tantalum was investigated to experimentally demonstrate the theoretical prediction that a HfO_2 filled photonic crystal would have superior omnidirectional performance and could reach 73% of the performance of an ideal emitter. An initial photonic crystal was fabricated, characterized and annealed for 300 hours at 1000°C .

1.7 Thesis Organization

This thesis focuses on the design, fabrication, and characterization of a practical high temperature photonic crystal selective emitter for high performance TPV systems, such as micro-combustion TPV, nuclear radioisotope TPV, or solar TPV. As detailed in the flowchart shown in Figure 1-10, the development of a fully integrated highly efficient TPV system can be broken into Chapters:

- In Chapter 2, the design constraints on selective emitter materials, photonic structure, and fabrication are discussed. The simulation and optimization of the chosen photonic structures are also detailed.
- In Chapter 3, the fabrication of the selective emitter photonic crystal is detailed, from substrate preparation, to nanostructuring of the photonic crystal, to the optical and thermal characterization of the fabricated emitter.
- In Chapter 4, thorough measurements and characterization of the optical and thermal performance of all the fabricated selective emitters is provided.
- In Chapter 5, an improved omnidirectional filled-cavity photonic crystal is developed, fabricated and characterized.
- In Chapter 6, different methods of system integration of the photonic crystal with the source of heat are presented, including challenges faced.
- In Chapter 7, a performance analysis quantifies the improvement in efficiency of a TPV system using our photonic crystal.
- A detailed chronology of TPV systems, low bandgap TPV cells, and selective emitter development and improvement is provided in Appendix A.
- The characterization of unprotected and hafnia-passivated unstructured polished tantalum is detailed Appendix B.
- The fabrication and characterization of sputtered metallic coatings as potential photonic crystal substates is detailed Appendix C.

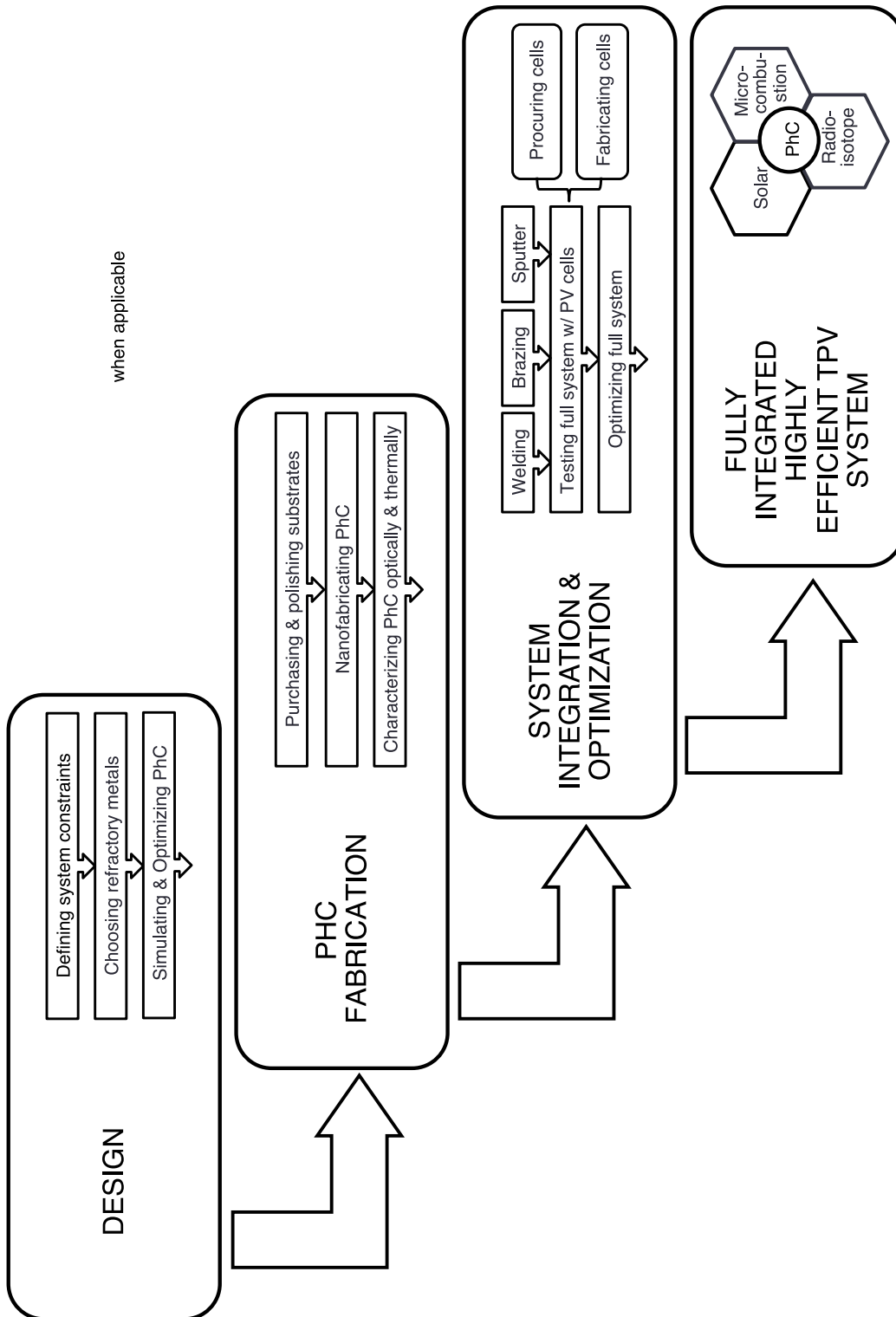


Figure 1-10: Photonic crystal design, fabrication, characterization, and integration process flowchart.

Chapter 2

Design

In order to maximize the efficiency of a TPV system, the emittance spectrum of the photonic crystal is tailored so that the cutoff wavelength λ_c of the high emittance band matches the bandgap λ_{PV} of a PV cell. We use metallic photonic crystals, which are metallo-dielectric structures with periodic wavelength-scale refractive index modulations. We use a simple approach to understand the physics of the photonic crystal. It is most intuitive to examine absorption of incident light: according to Kirchhoff's law, the absorptivity of incident exactly equals the thermal emissivity. We assume there are two regions: a region of high absorption and a region of high reflection. In the high absorption region, incident light excites cavity resonances which in turn effectively couple into the absorption of the metallic substrate. In the high reflection region, the frequency of the incident light does not excite the cavity resonance and the incident light only sees an effective medium of metal and air.

For our design, we can approximate the locations of the resonances, and hence the high emissivity region, by finding the modes of a cylindrical cavity. The strength of each resonance depends on how effectively it can “impedance match” between radiation and the absorption of the metal.

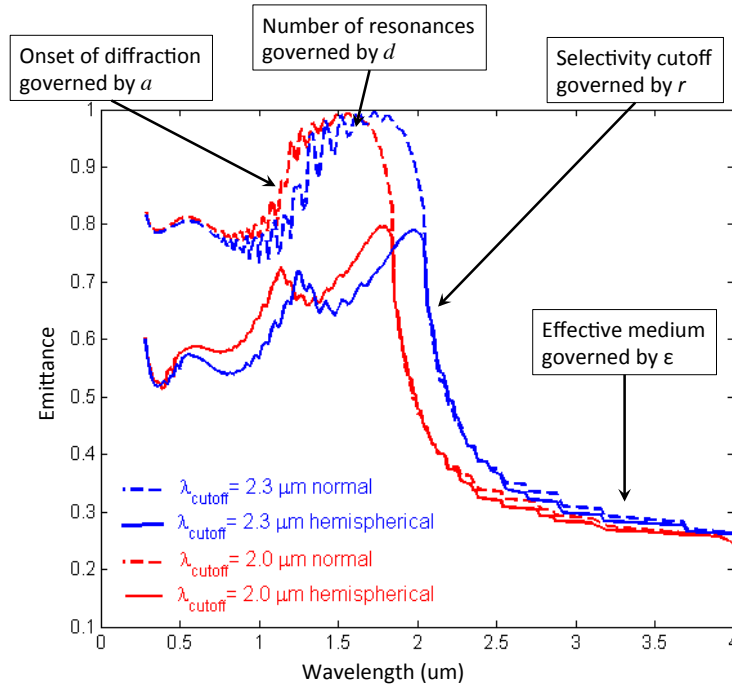


Figure 2-1: The primary influence of each geometric parameter in the photonic crystal design: r is the radius of the holes, d is the hole depth, and a is the period. The spectral emissivity of a blackbody is unity for all wavelengths and is the upper limit that any material can achieve. A selective emitter radiates only within a certain wavelength range. Some physical constraints imposed by fabrication: $a - 2r > 150$ nm, $d < 8$ μm . In our 2D photonic crystal the emissivity cannot be suppressed below the emissivity ε of flat polished Ta; it can only be enhanced in the region of interest. This is contrary to the 1D design, where the emittance is high to start with and is suppressed in the region of interest.

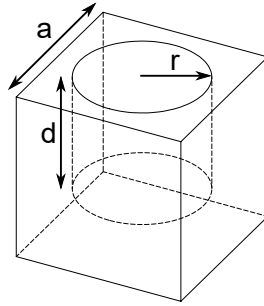


Figure 2-2: Drawing of one period of the simulated photonic crystal structure where r is the radius of the holes, d is the hole depth, and a is the period.

2.1 Analytical Modeling

This section describes two analytical modeling methods: the cavity resonance approach and the Q -matching approach. These methods lead to valuable insight into the physics of the photonic crystal and the mechanisms by which each design parameter affects the spectrum. They also provide a simple set of design tools that can be used to generate an initial set of parameters for nonlinear optimization. We study a isolated single cavity for simplicity, since there is no interaction between cavities through the substrate because the wall thickness is much greater than the penetration depth and since most of the interaction occurs on the surface.

2.1.1 Cavity Resonance Approach

The modes of an isolated finite depth cavity are governed by the lowest order resonant modes of the cylindrical cavity:

$$\omega_n = \begin{cases} \sqrt{\left(\frac{lr}{4d}\right)^2 + \left(\frac{\xi'_{mn}}{2\pi}\right)^2} & \text{TE modes} \\ \sqrt{\left(\frac{lr}{4d}\right)^2 + \left(\frac{\xi_{mn}}{2\pi}\right)^2} & \text{TM modes} \end{cases} \quad (2.1)$$

where, ξ_{mn} is the n_{th} root of the m_{th} order Bessel function, ξ'_{mn} is the n_{th} root of the m_{th} order Bessel function derivative, d and r are the depth of the cylinder and the cylinder radius, respectively, and l is an integer number. Cavity mode frequencies are expressed in normalized frequency units of $2\pi c/r$ [47]. The semi-open cavity can be modeled as a completely enclosed metallic cylinder cavity of depth $2d$ and the cutoff frequency is the lowest order mode. The high emissivity region below the cutoff wavelength is filled by many overlapping modes. A relationship between the desired cutoff wavelength and radius can be derived from the lowest cylindrical cavity mode:

$$r \approx 1.8412 \times \frac{\lambda_c}{(2\pi)} \quad (2.2)$$

The lowest mode obtained from Equation 2.1 is plotted in Figure 2-3, represented by a down arrow. While this approach predicts the peaks due to waveguide resonances, occurring at frequencies corresponding to the isolated waveguide resonant frequencies, the amplitude of the peaks is missing. For this, a Q -matching approach must be used.

2.1.2 Q-Matching Approach

As described in Ref. [50], Q -matching is used to understand the relative strength of the resonant enhancement to emission. Enhancement is the strongest when energy flows into and out of the cavity at the same rate. This condition is best understood by looking at the loss rate of energy in the cavity by different mechanisms. The cavity resonances experience two major types of losses: radiation through the top and absorption on the sidewalls and bottom. From each loss rate, a quality factor $Q = \omega_0\tau/2$ is calculated, where ω_0 is the resonant mode frequency and τ is the lifetime (or inverse loss rate) associated with a particular loss mechanism. The quality factor is a dimensionless lifetime: After Q periods, a resonance decays by $\exp(-2/\pi)$. When these two loss rates are equal—the Q -matching condition—complete absorption of incident radiation occurs. If these loss rates are not too large compared to the resonant

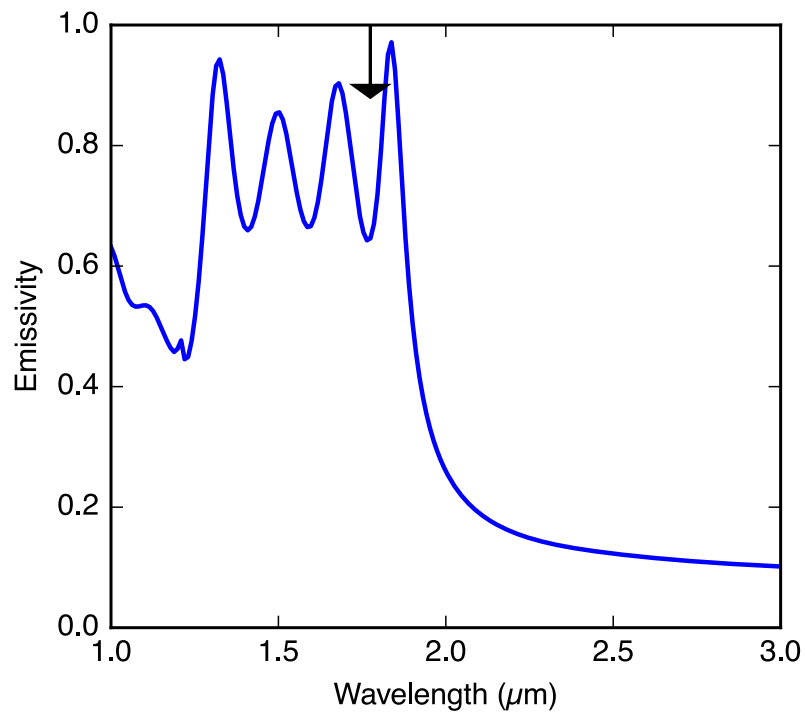


Figure 2-3: Using Equation 2.1, we can predict the lowest frequency mode, shown as a black arrow. The blue curve corresponds to a numerical simulation of an optimized photonic crystal for cutoff at 2.0 μm .

frequency, then each can be calculated independently [19]. Although calculation of the rates is beyond the scope of this work (see Ref. [50]), the absorptive rate can be closely approximated by closing the top with a perfectly conducting metal. A higher material absorption (resulting in a lower absorptive Q) can be matched if r increases and d decreases, as the radiative Q scales as $(d/r)^3$. The radiative and absorptive rates of these coupled waveguide resonances should depend more strongly on the hole radius r and depth d than on the period a ; therefore consider first a single, isolated hole ($a \rightarrow \infty$).

2.2 Numerical Modeling

In this work, photonic crystals were simulated using numerical methods prior to fabrication. First, the material properties of the substate, tantalum, were determined using a Lorentz-Drude model fitted to the elevated temperature emissivity to capture the optical dispersion of the substrate at high temperature. Initially, finite-difference time-domain (FDTD) was used, then rigorous coupled wave analysis methods (RCWA) Stanford Stratified Structure Solver (S4) for faster performance, including angular performance. Nonlinear optimization (NLOpt library, Python library) determined the period, cavity radius, and height with bounds based on fabrication constraints.

2.2.1 Simulation

The dispersion of tantalum is included in the simulations using the Lorentz-Drude model, fit using ReFFIT, a free program [56], both to the reflectance values at room temperature as measured on flat substrates and at elevated temperatures as taken from literature [57]. The spectral emissivity of the photonic crystal at normal incidence was initially determined by MEEP, developed at MIT [58], via FDTD numerical methods. However its high computational requirements limited its application in de-

termining the optimized hemispherical emissivity. Thus, for quicker estimation, a mode matching formalism was developed matching the radiation fields at the boundary of free space and the cylindrical cavities via expansion in the basis of a small number of cavity modes for shorter wavelengths and utilizing a surface area weighted impedance for longer wavelengths [50]. More recently, a rigorous coupled wave analysis methods (RCWA; also called the fourier modal method) [59] were made available to simulate the full hemispherical performance relatively quickly. It has been verified numerically that the most significant influence on the spectral properties in the range of interest is given by the cavity radius, whereas the period mainly influences the spectral position of the diffraction limit.

2.2.2 Optimization

Nonlinear optimization determined the period, cavity radius, and height with bounds based on fabrication constraints. The NLOpt software library for nonlinear optimization, developed at MIT [60], is used with two different optimization algorithms: controlled random search (CRS) with local mutation and multi-level single-linkage (MLSL) with the geometric parameters of period, cavity radius and height as optimization parameters. To take into account fabrication constraints, a minimum space of 0.1 μm between cavities was imposed and the maximum cavity height was limited to 8.0 μm . It has been verified that the most significant influence on the spectral properties in the range of interest is given by the cavity radius, whereas the period only influences the spectral position of the diffraction limit (i.e. the emissivity at shorter wavelengths). The increase of spectral efficiency with cavity height is decreasing and essentially negligible above a certain aspect ratio (diameter to height), the height of the cavity was thus limited to 8.0 μm in the optimization.

Initially, in this work, the figure of merit used in the optimization was spectral selectivity η_{sp} defined as the ratio of the number of (useful) photons emitted in the desirable wavelength range given by the TPV cell to the overall emitted photons at

Table 2.1: Dimensions of the 2D photonic crystal parameters optimized by NLOpt for different TPV cells and their respective cutoff wavelengths.

Cell	λ_{PV} (μm)	r (μm)	a (μm)	d (μm)
InGaAsSb	2.3	0.55	1.22	7.16
InGaAs	2.0	0.49	1.1	8.0
GaSb	1.8	0.43	0.96	8.0

a given operating temperature (Eq. C.2). The parameters of the NLOpt optimized designs for a target operating temperature of 1200°C are given in Table 2.1.

Another optimization was implemented using a Python library. The geometric parameters were optimized for multiple cutoff wavelengths, shown in Figure 2-4. A sequential least squares programming (SLSQP) method was used to perform a constrained nonlinear optimization of a , r , and d in order to maximize the figure of merit, the efficiency of a simplified, idealized hydrocarbon TPV system. Cutoff wavelengths were handled by changing the bandgap of the PV cell in the figure of merit calculation.

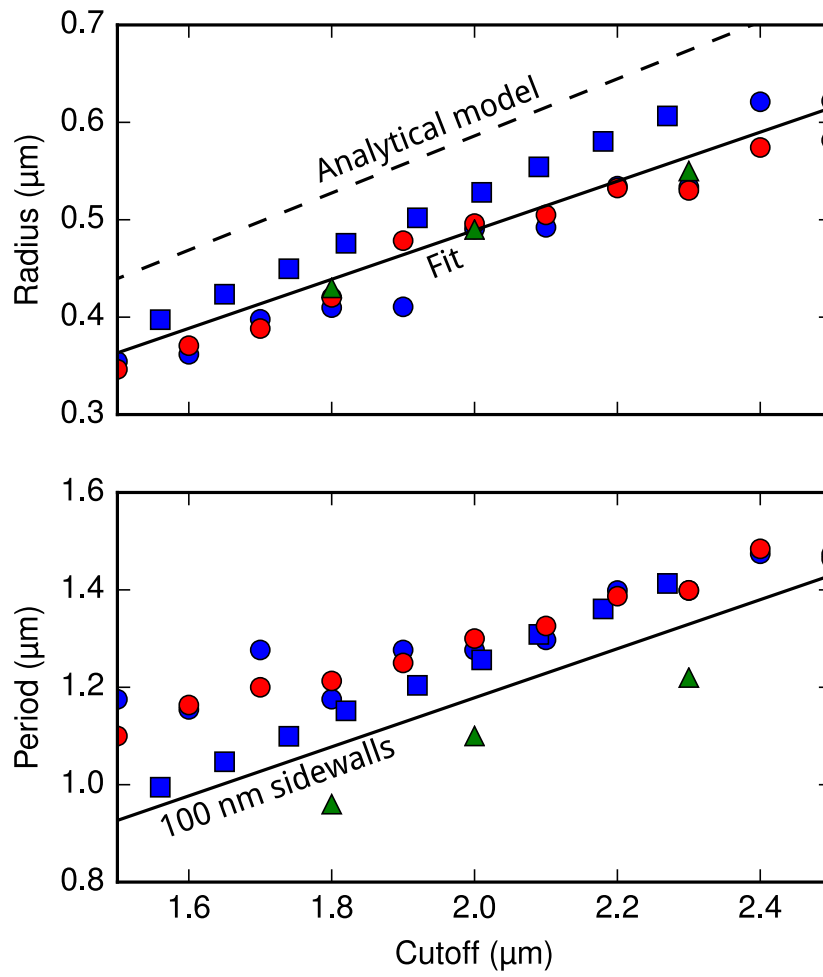


Figure 2-4: Geometric parameters, radius r and period a , optimized for cutoff wavelengths λ_c ranging from 1.4 to 2.6 μm .

Chapter 3

Large Area Photonic Crystal Fabrication

The general process flow for the fabrication of our 2D photonic crystal selective emitter is shown in Figure 3-1, involving: (1) substrate preparation, (2) fabrication layers (photoresist, antireflection coating, etch mask) deposition, (3) pattern generation by interference lithography, (4) pattern transfer into a fabrication layers, (5) final etch of substrate and removal of residual fabrication layers, and (6) surface passivation of the photonic crystal structure by atomic layer deposition for thermal stability. As part of this work, a number of improvements were made in each step of the fabrication process and are summarized in Table 3.1. These improvements are described in detail in this chapter as well as the current nanofabrication process for fabricating a 2D photonic crystal emitter to TPV applications.

In summary, the process was initially developed for tungsten substrates using



Figure 3-1: The general process flow for the fabrication of our 2D photonic crystal selective emitter.

laser interference lithography for patterning and wet etching of a chromium mask used to transfer the pattern into the tungsten substrate by carbon-tetrafluoride-based tungsten reactive ion etching (RIE) [61]. Multiple improvements were made to the original process:

- The wet etch of the chromium etch mask resulted in poor hole definition and lowered the performance of the photonic crystal. Switching from the wet etch to reactive ion etching (RIE) of the chromium mask enabled optical performance improvement [49, 62].
- Switching from single crystal tungsten to polycrystalline tantalum made it possible to fabricate large substrate materials.
- Tungsten was also difficult to machine and weld so tantalum was found to be a better substrate—a compromise of optical performance, thermal stability, and ease of integration.
- The Mach-Zehnder interferometer system allowed for large patterning of up to 6 in wafers [38], unlike the Lloyd’s mirror.
- The residual chromium mask was difficult to remove (using CR-7 etchant), lowering the reflectance of the photonic crystal in the long wavelengths. Using an SiO_2 mask instead further improved the performance of the photonic crystal as SiO_2 could be easily removed by hydrofluoric acid without damaging the substrate.
- The fabrication process was developed for both bulk metallic substrates and sputtered substrates [63, 64].
- A HfO_2 passivation layer was added by atomic layer deposition to greatly improve the thermal stability of the photonic crystal.

All these developed processes are described in detail in the following sections.

Table 3.1: Improvements made for each fabrication step.

Step	Improvement	Prior Work	Current Work
1	Substrate	Tungsten	Tantalum
2	Etch layer	Cr mask	SiO ₂ mask
3	Interference lithography	Lloyd's mirror	Mach Zehnder
4	Pattern transfer	Wet etch	Dry etch
5	Substrate etch	RIE	DRIE
6	Passivation	None	HfO ₂

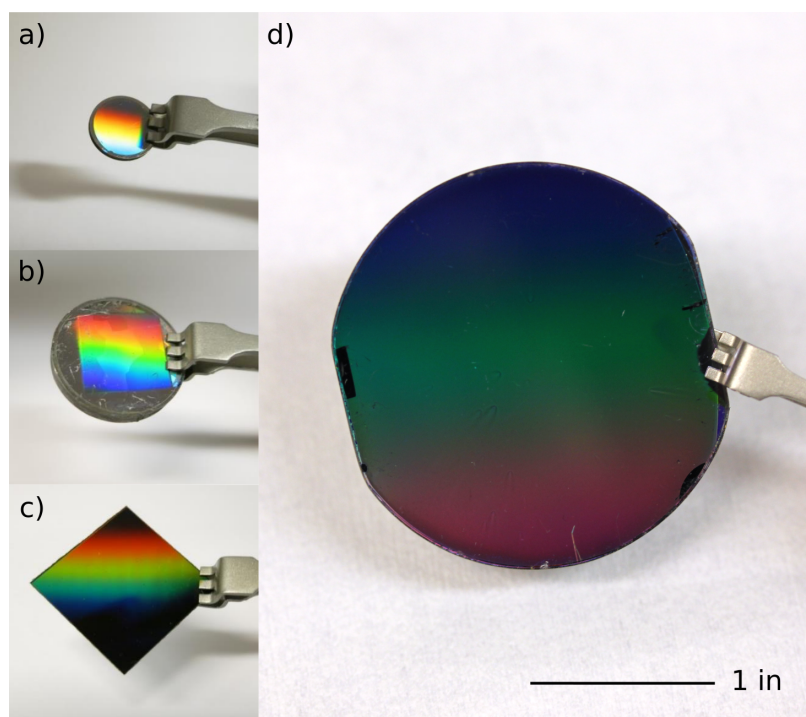


Figure 3-2: The evolution over time of the substrates, from a) small and thick single crystal tungsten to b) small and thick polycrystalline tantalum, to c) cold rolled sheets of tantalum 3% tungsten alloy, to d) large tantalum and tantalum 3 % tungsten wafers (up to 3 in). All photographs are on the same scale.

3.1 Substrate Preparation

The intended use of the selective emitters in high-temperature energy conversion applications with target operating temperatures ($>1000^{\circ}\text{C}$) and expected lifetimes of years imposes strict requirements on both the thermal stability of the fabricated microstructures and their optical properties as well as the thermal and thermo-mechanical stability of the emitter substrates in the context of system integration. Refractory metals are preferred at high temperatures due to their high melting point, low vapor pressure and advantageous high reflectivity in the IR.

- *Single crystal tungsten* was the first substrate investigated as the substrate for a high-temperature selective emitter, due to its excellent optical properties in the wavelength range of interest and good thermal stability. However, while tungsten has high yield strength and Young's modulus, it is very brittle and therefore hard to machine or weld.
- Therefore the next generation of photonic crystals was fabricated on *polycrystalline tantalum*. Tantalum is soft and more compliant, in addition to being easily weldable and machinable. The polycrystalline nature of the substrate allows for larger substrate size. Working with the supplier, we were able to obtain cheaper sheets of polycrystalline tantalum, which was also very desirable. High purity ($> 99.9\%$) tantalum polycrystalline tantalum substrates were supplied by H.C. Starck (Newton, MA). These substrates were stress relieved at 1339K and their initial grain size was measured as $57 \pm 8 \mu\text{m}$. However for a tantalum based system to achieve the same mechanical stability as for a tungsten based system, a thicker substrate is required due to tantalum's softness, which added to the system weight and cost.
- The use of a *tantalum-tungsten alloys* was then proposed to achieve the same thermo-mechanical stability while keeping the required material thickness low. Indeed the tantalum 3% tungsten alloy combines better thermo-mechanical

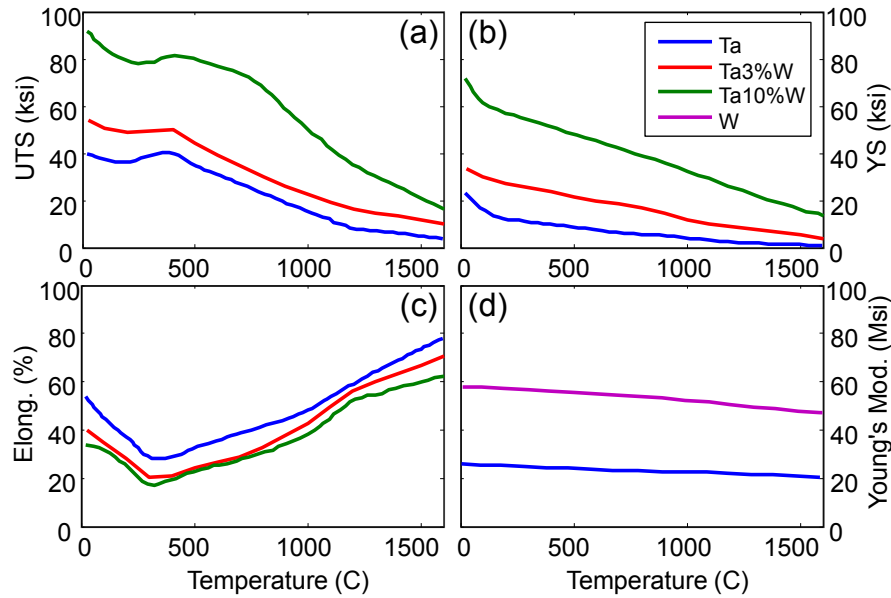


Figure 3-3: Comparison of a) ultimate tensile strength (UTS), b) yield strength (YS) and c) percent elongation of tantalum, tantalum 3% tungsten and tantalum 10% tungsten and their dependence on temperature. d) Comparison of Young's modulus of tantalum and tungsten [65].

properties of tungsten with the more compliant material properties of tantalum, allowing a direct system integration path, i.e. machining and welding.

- An alternative metallic substrate coating was also developed for improved integration with the heat source. Both tungsten and tantalum thick coatings were investigated and *sputtered tantalum* was found to be a suitable substrate for photonic crystal fabrication.

The bulk and sputtered substrates were prepared differently: in the case of the bulk metals, the surface must be polished to mirror finish in order for the photonic crystal to have maximum reflectance; in the case of the sputtered metals, the surface as-deposited was found to be sufficiently reflective, if the substrate on which the metal was sputtered was polished to mirror finish. The tantalum and tungsten coatings preparation is discussed in detail in Appendix C. Bulk substrates were cut, lapped to a thickness of 1 mm, and chemo-mechanically polished to achieve a roughness R_a

of less than 10 Å (mirror finish) by Cabot Microelectronics (Addison, IL). In the case of single crystal tungsten substrates, relatively small substrates were used (1 cm diameter) and the thickness was closer to 3 mm. In the case of tantalum, different substrates preparation conditions were investigated: hot rolled tantalum, cold rolled tantalum, pre-annealed at different temperatures to achieve thermal stability of the polycrystalline substrate material with large grain size. The tantalum 3% tungsten substrate was prepared from an alloy of high purity polycrystalline tantalum and tungsten (2–3.5% concentration). Figure 3-3 illustrates the mechanical properties of tantalum, tantalum 3% tungsten and tantalum 10% tungsten and their dependence on temperature and shows the increasing mechanical stability with increasing tungsten content of the alloy for all temperatures [65].

3.2 Nanofabrication

Once the substrate has been prepared, the photonic crystal can be fabricated. The following fabrication steps are performed in a clean room facility, and correspond to the latest fabrication process. This work was done at MIT (NSL), Harvard (CNS), and University of Chapel Hill (CHANL), either by the author or the technician associated with the tool.

3.2.1 Etching Layers

In order to fabricate the photonic crystal, SiO₂ is used as a hard mask for etching the tantalum substrate. The 250 nm SiO₂ layer is deposited by *plasma enhanced chemical vapor deposition* (PECVD) onto the cleaned polished metallic substrate. In PECVD processes, deposition is achieved by introducing reactant gases between parallel electrodes. The capacitive coupling between the electrodes excites the reactant gases into a plasma, which induces a chemical reaction and results in the reaction product being deposited on the substrate. The substrate was heated to 250°C during the SiO₂

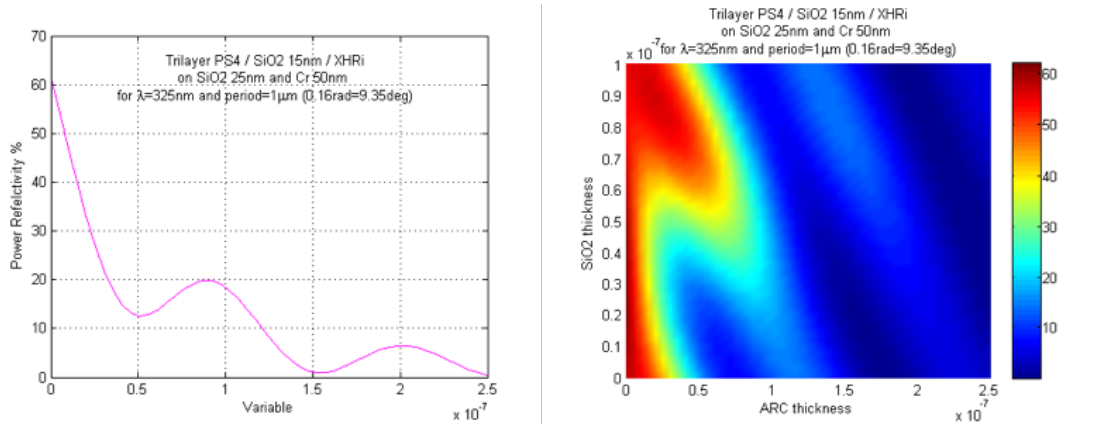


Figure 3-4: (a) (b) Tri-layer stack optimization in RGUI.

deposition¹. A standard tri-layer stack, designed for interference lithography, is then deposited: the anti-reflection coating (ARC, AZ BARLi, Microchemicals, 270 nm) is spin coated (followed by a post-bake at 175°C for 90 sec), then a 10 nm thick SiO₂ protection layer for the ARC is e-beam evaporated, and the negative photoresist layer (PS, NR7, Futurrex, 250 nm) is spin coated onto the sample (followed by a post-bake at 150°C for 60 sec) for the initial lithography process. The tri-layer stack thicknesses are optimized in RGUI, a freely available software at MIT, and obtained by varying the speed of the spin-coater, according to experimentally measured spin curves.

3.2.2 Interference Lithography

In an interference lithography (IL) setup, two coherent laser beams interfere with each other creating an interference pattern that is recorded in the photoresist by exposure, creating a fringe pattern. The exposure is performed once, and then once more after the samples are rotated by 90° to create a square array of cylindrical cavities. In order to obtain the large and uniform periodic pattern required, IL is performed using a

¹Previously, a 100 nm layer of chromium etch mask and 40 nm SiO₂ transfer layer were both deposited by e-beam evaporation, instead of the single thick 250 nm SiO₂ etch mask currently used. The chromium layer was difficult to completely remove by CR-7 and the residual amount was found to increase the emittance of the photonic crystal in the longer wavelength range.

Mach-Zehnder setup with a 325 nm HeCd Laser². Interference lithography requires no contact mask, can be easily tuned to match the desired period for the pattern, and quickly generates dense features over a wide area without loss of focus. The period of the pattern a is defined by the interference angle θ as $a = \lambda/2 \sin \theta$ [66]. The exposure times are calculated based on previous exposure times for a certain laser power, however since the laser fluctuates, the times are adjusted every time. The target diameter of the cylindrical cavities is based on simulations. Table 2.1 summarizes the appropriate dimensions found for typical TPV cell cutoffs. Due to the Gaussian distribution of the intensity of the exposure beam, the diameter of the holes is not completely uniform across the sample. Since the exposure dose is decreasing with the distance from the center of the substrate, the hole diameter is increasing slightly towards the edges of the sample, however the difference in hole size, and thus cutoff wavelength, was found to be minimum (changes by about 20 nm from the center to the edge of the sample).

3.2.3 Pattern Transfer

After the exposure, the pattern in the photoresist is developed (RD6:H₂O 3:1, for 60 sec), and baked post exposure at 100°C for 60 sec. The patterned holes are then made larger by isotropic O₂ plasma ashing. In an oxygen plasma asher, the reactive species, oxygen, combines with the photoresist to form ash which is removed with a vacuum pump. Longer ashing times result in larger hole diameters, however this is limited by the thickness of the resist. Generally an increase of the cavity diameter of about 200 nm is achieved by ashing the photoresist for 90 s at 200 W.

The pattern is then transferred by reactive ion etching (RIE) into the SiO₂ and ARC layers using a CF₄ and He/O₂ process respectively (Plasmatherm 790). Reactive ion etching is a type of dry etching which has different characteristics than wet etching.

²Prior to this work, a Lloyd's mirror setup was used for the exposure limiting the size of the samples that could be fabricated to only a few cm.

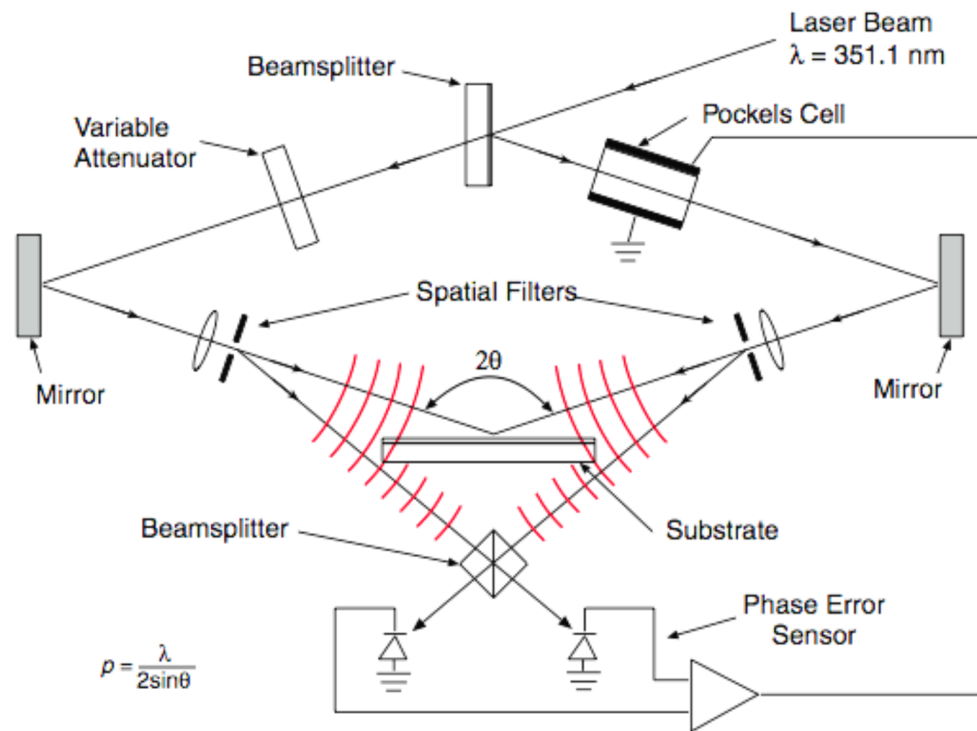


Figure 3-5: Schematic of Mach-Zehnder interferometer used to create the interference pattern in the photoresist. Constructive interference occurs when the waves are in phase, and destructive interference when they are half a cycle out of phase. Thus, an interference fringe pattern is produced. For 2-beam interference, the fringe-to-fringe spacing or period $p = (\lambda/2) / \sin(\theta/2)$ where θ is the angle between the two interfering waves. P_{min} achievable is then half the wavelength. A spatially coherent light source, a 325 nm HeCd laser, is used.

It uses chemically reactive plasma to remove material deposited on wafers. The plasma is generated under low pressure (vacuum) by an electromagnetic field. High-energy ions from the plasma attack the wafer surface and react with it.

Once the pattern has been transferred to the ARC layer, it can be increased once again by ashing the ARC to match the desired hole size. After the desired diameter is obtained, the cavities are etched into the underlying SiO₂ layer by the same CHF₃ based RIE process³.

Table 3.2 summarizes the parameters used during the RIE processes, for different masks and different substrates. Throughout the entire fabrication process, a photonic crystal is also fabricated on a Si test substrate using the exact same steps to facilitate imaging and testing. The overall fabrication steps are shown in Figure 3-7 using the Si test piece.

3.3 Substrate Etch

The final pattern transfer into the tantalum substrate was done by deep reactive-ion etching (DRIE) (Alcatel AMS100) with a Bosch process. Deep reactive-ion etching is a highly anisotropic etch process used to create deep penetration, steep-sided holes and trenches, originally developed for microelectromechanical systems. The Bosch process alternates repeatedly between a standard etch mode, nearly isotropic plasma etch, and a deposition mode, a chemically inert passivation layer, to achieve nearly vertical structures. These etch/deposit steps are repeated many times over resulting in a large number of very small isotropic etch steps taking place only at the bottom of the etched pits, resulting in small scalloping of the walls.

Our process uses SF₆ (200 sccm) and C₄F₈ (100 sccm) with 3 s/1.5 s pulses as the etching and passivating species, respectively, power 1200 W, pressure ~ 3 mTorr, substrate bias 75 W, and temperature 20°C. The pulse duration was optimized to

³In previous work, the pattern was transferred into the chromium mask by a Cl₂/O₂ based RIE process (Nexx Cirrus 150).

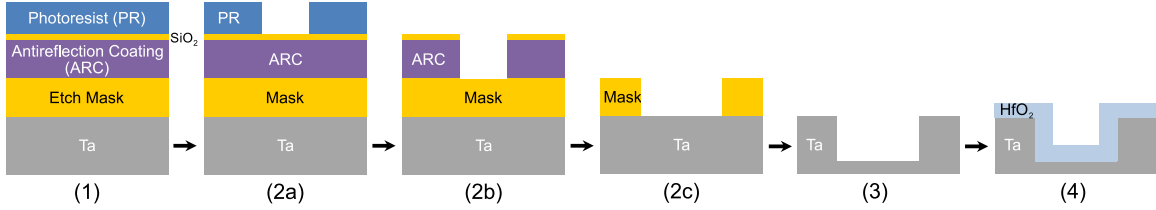


Figure 3-6: A general process flow for the fabrication of our 2D photonic crystal involves (1) pattern generation by interference lithography, (2) pattern transfer into a hard mask by reactive ion etching, (3) pattern transfer into the metallic substrate by reactive ion etching, and (4) surface passivation by atomic layer deposition for thermal stability.

Table 3.2: Parameters used during the RIE and DRIE processes to etch the tantalum using a chromium or SiO_2 mask.

Material	Gases	Flow (sccm)	Pressure (mTorr)	Power (W)
ARC	He/O_2	10/5	7	120
SiO_2	CF_4	15	10	150
Cr	Cl_2/O_2	15/3	5	300/100
Ta	$\text{SF}_6/\text{C}_4\text{F}_8$	200/100	3	1200/75

achieve complete passivation of the sidewalls and a straight sidewall etch profile, and the etch time is limited to 5 min cycles to prevent overheating of the substrate. An etch depth of about 6 μm corresponding to an aspect ratio of about 6 was achieved in tantalum with an overall etch time of 10 min⁴.

3.4 Surface Passivation

Surface diffusion and surface chemical reactions are known high-temperature photonic crystal degradation mechanisms. The addition of a protective dielectric, HfO_2 onto the fabricated selective emitters prevented both structural degradation by sur-

⁴In previous work, after DRIE, the remaining chromium layer was removed by CR-7 (Cyantek) liquid etchant. However a small amount of chromium would still be on the surface even after etching, increasing the emittance of the tantalum in the long wavelength range which was undesirable.

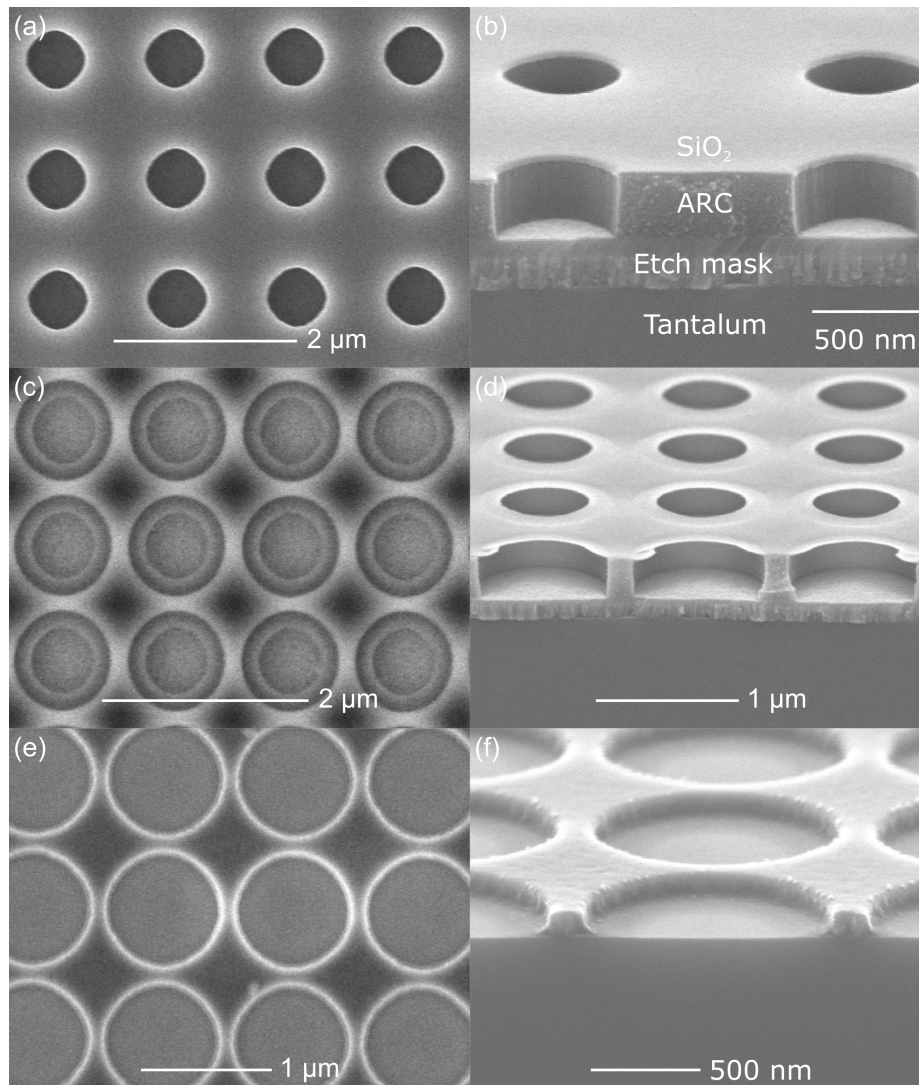


Figure 3-7: SEM of Ta PhC (left column, top view) and Si test piece (right column, cross section) after several fabrication steps, before DRIE.

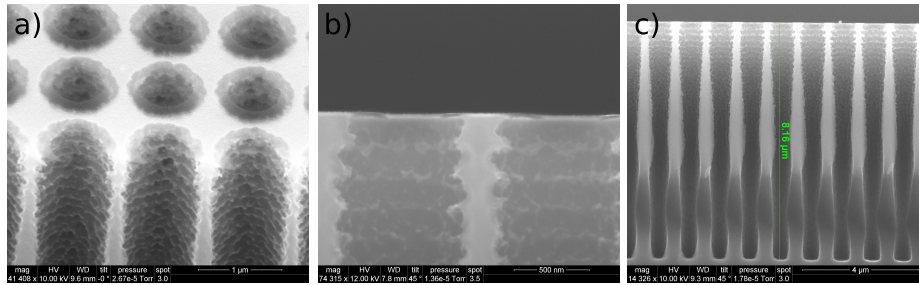


Figure 3-8: SEM of Si test piece after DRIE. Note the small scalloping of the walls, due to the alternating etch and passivation cycles.

face diffusion and grain boundary grooving as well as surface reactions such as the formation of tantalum carbide on the surface of the photonic crystal at high temperatures [33, 42, 67], as detailed in Chapter 4.

Atomic layer deposition is a thin film deposition method in which a film is grown on a substrate by exposing its surface to alternate gaseous precursors. In contrast to chemical vapor deposition, the precursors are never present simultaneously in the reactor, but they are inserted as a series of sequential, non-overlapping pulses. In each of these pulses the precursor molecules react with the surface in a self-limiting way, so that the reaction terminates once all the reactive sites on the surface are consumed. Consequently, the maximum amount of material deposited on the surface after a single cycle is determined by the nature of the precursor-surface interaction. By varying the number of cycles it is possible to grow materials uniformly and with high precision on arbitrarily complex and large substrates. The ALD deposition ensures completely conformal deposition of the coating in the high aspect ratio cavities.

In our photonic crystal, a 20-40 nm hafnia coating was deposited on the fabricated photonic crystals by ALD (Cambridge NanoTech Savannah) using the parameters given in Table 3.3.

Table 3.3: Parameters used during the HfO₂ ALD process using TDMAH precursor to conformally coat the cavities of the photonic crystal.

Process	Chamber temperature (°C)	Precursor temperature (°C)	N ₂ carrier flow (sccm)	Base pressure (mTorr)
ALD	250	85	20	200

3.5 Impact of Nanofabrication Improvements on Performance

The evolution of the photonic crystal fabrication is summarized in Figure 3-9. Prior to this work:

- A Lloyd's mirror setup was used for the exposure limiting the size of the samples that could be fabricated to only a few cm.
- A wet etch was used to transfer the pattern into the tungsten substrate which resulted in holes with high sidewall roughness, resulting in poor optical performance, as shown in Figure 3-10.
- Even once the pattern was transferred into the chromium mask by a dry etch (Cl₂/O₂ based RIE process using a Nexx Cirrus 150), the chromium layer was difficult to completely remove by CR-7 and the residual amount was found to increase the emittance of the photonic crystal in the longer wavelength range, which was undesirable.
- The photonic crystal's optical performance degraded after anneal for as little as 3 hours at 900°C, due to the lack of a passivation layer.
- No demonstrated integration path existed for the photonic crystal and heat source.

3.5. IMPACT OF NANOFABRICATION IMPROVEMENTS ON PERFORMANCE⁶⁷

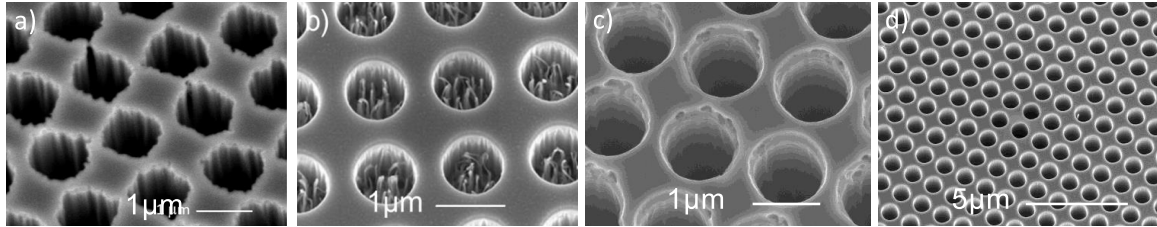


Figure 3-9: Improvements over the course of this work of the photonic crystal fabrication, from a) wet etching to b) RIE using a chrome mask, to c) d) RIE using an SiO₂ mask.

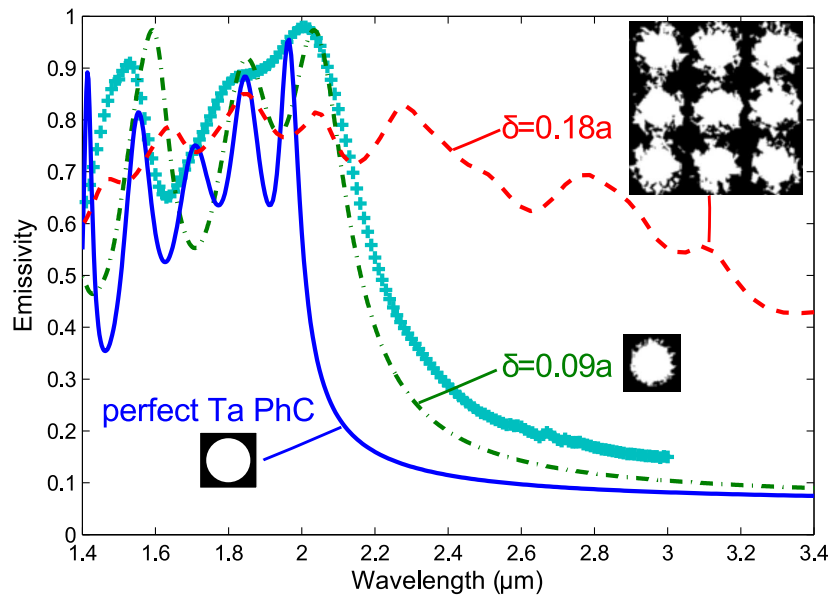


Figure 3-10: Simulation of the emissivity for a tantalum photonic crystal with perfect structure (solid line) and increasing sidewall roughness characterized by the maximum deviation $\delta = 0.09a$ (dashed-dotted line) comparable to the photonic crystal fabricated by wet etch with the measured emissivity (crosses), and simulation with $\delta = 0.18a$ (dashed line) resulting in breaking sidewalls. (Reproduced from [38] with permission).

Chapter 4

Optical Performance and Thermal Stability

Over the course of this work, dramatic improvements were made to: photonic crystal substrates, photonic structure fabrication methods, materials properties, thermal and optical properties, and characterization methods. In this chapter, we summarize the optical measurements, characterization methods, and results of our fabricated photonic crystals by substrate material (Ta, Ta 3% W alloy, and sputtered Ta), fabrication process (Cr and SiO₂ etch mask), and targeted cutoff wavelength (1.7 μm , 2.0 μm , and 2.3 μm). For all of these photonic crystals, we provide their optical parameters (in-band emissivity ε_{in} , out-of-band emissivity ε_{out} , cutoff wavelength λ_c , and steepness of cutoff k) and geometric parameters (period a , radius r , and depth d). All the hafnia-passivated photonic crystals were characterized before and after anneal at temperatures ranging from 900 to 1200°C and times ranging from 1 to 1000 hours, and the annealing conditions are provided for each photonic crystal. A flat polished tantalum and a tungsten photonic crystal fabricated by Yeng [49] are also provided for calibration and comparison, respectively.

4.1 Optical Measurements

Scanning electron microscopy (SEM) is used throughout this work to measure the geometric parameters of the photonic crystal. However, obtaining absolute measurements by SEM across many different samples is difficult. Therefore, the geometric parameters were also obtained from simulations fitted to the experimentally measured emittance spectra of each photonic crystal. The emittance of the fabricated photonic crystals was first obtained by spectroradiometric measurement (Gooch and Housego OL750) from near normal angle reflectance measurements at room temperature, using Kirchhoff's law by which the emittance $E = 1 - R$ for non-transmitting substrates. A good match between the numerical simulation and measured emittance was generally observed and the geometric parameters were then fitted to the simulations for better accuracy than visual inspection and measurement by SEM. Figure 4-1 shows good agreement between the measured emittance and the simulation ($r=0.53 \mu\text{m}$, $a=1.3 \mu\text{m}$, and cavity depth $d=6.7 \mu\text{m}$). The HfO_2 coating causes a slight shift of the cutoff wavelength, due to the higher index of refraction, which was taken into account in simulation and optimization of the photonic crystal geometry. Since the optical characterization was done at room temperatures, the simulations were then re-run with the same geometric parameters but using the high-temperature optical properties of tantalum to simulate the real performance of the emitter in a TPV system operating at 1200°C . Furthermore, since the optical characterization was done at normal incidence angles, the simulations were also re-run with the same geometric parameters but for full hemispherical emissivity to simulate the real performance in a TPV system, where an ideal emitter would have excellent omnidirectional performance.

An improved optical characterization method was developed by a system of calibration involving low and high reflectance calibrated mirrors and blocking the beam. More recently fabricated samples were characterized using this method. An alternative characterization approach was also used to measure directly the thermal emission

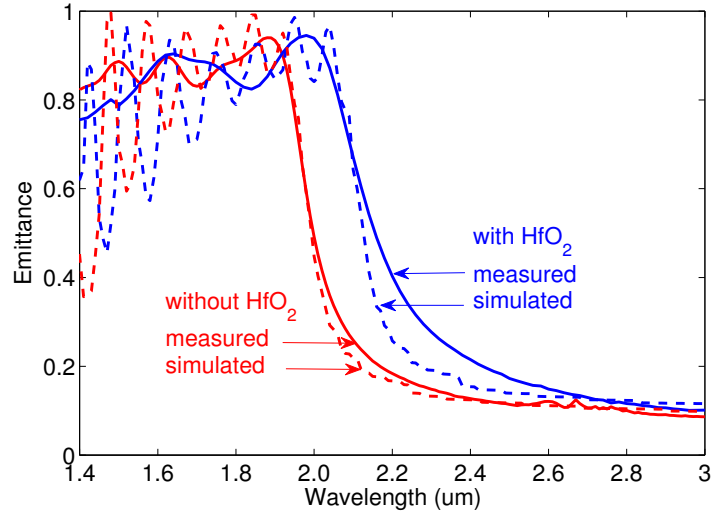


Figure 4-1: Ta 3% W sample fabricated with SiO₂ mask (with $a=1.37\ \mu\text{m}$, $r=0.53\ \mu\text{m}$, and $d=6.7\ \mu\text{m}$): Comparison of the normal emittance obtained from reflectance measurements and simulations at room temperature of the Ta 3% W photonic crystal without and with a HfO₂ coating of 40 nm thickness.

of the photonic crystals at high-temperature in a vacuum sealed heater with a calcium fluoride window facing the entrance of an FTIR, at normal incidence and different temperatures. However this method necessitates derivation of the temperature from simulation due to the large temperature gradients between the surface of the heater and photonic crystal. Thus only a few samples were characterized using this method.

4.1.1 Room Temperature Measurement

All of our fabricated photonic crystal selective emitters show high emittance below the cutoff wavelength while maintaining low emittance above, with a steep cutoff between, as shown in Figure 4-5 and summarized in Table 4.1. The measured reflectance of the hafnia-passivated Ta 3% W photonic crystal is shown before and after annealing in Figure 4-2. The spectral emittance was preserved after the 24 hour anneal at 1200°C [41]. A small degradation of the cutoff tail was observed after anneal, as well as a slight increase of the emittance above the cutoff wavelength, which is attributed

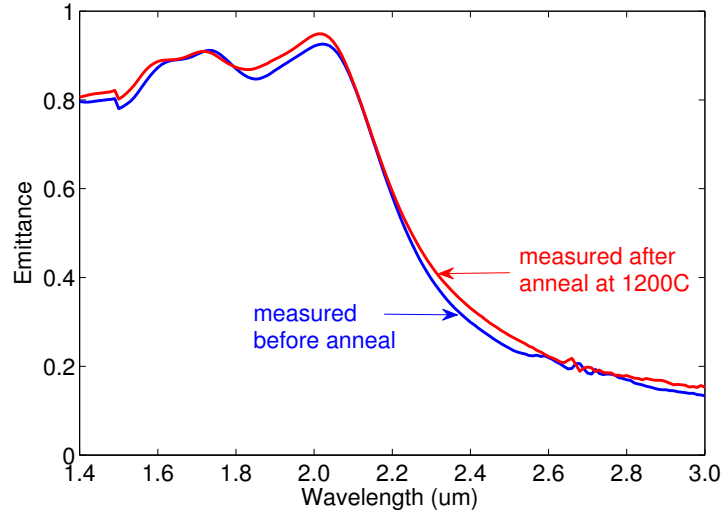


Figure 4-2: Ta 3% W sample fabricated with SiO_2 mask (with $a=1.37 \mu\text{m}$, $r=0.53 \mu\text{m}$, and $d=6.7 \mu\text{m}$): Comparison of the normal emittance of the Ta 3% W photonic crystal with a 40 nm HfO_2 coating before and after anneal at 1200°C for 24 hours in a vacuum furnace with the normal emittance of the polished substrate.

to carbide formation on the surface due to remaining carbon contamination in the vacuum system, as determined by Auger electron spectroscopy (AES). The structural stability of the Ta 3% W photonic crystal with the HfO_2 ALD coating was studied through the FIB cross sectional images before and after annealing, showing no change of the photonic structure profile, as shown in Figure 4-3. Surface diffusion was effectively prevented by the HfO_2 coating at least for the observed time and temperature scale.

Absolute accuracy in reflectance measurements is crucial to compare photonic crystals before and after annealing or other processing, and to compare different samples. In all instruments, we found a 10% variation in our data when using their standard calibration method. This made it particularly difficult to evaluate the degradation of our structure. In order to correct for these variations, we developed a system of calibration involving low and high reflectance calibrated mirrors (Ocean Optics STAN-SSL and STAN-SSH) and blocking the beam, using a different UV-Vis-NIR spectrophotometer than previously (Agilent Technologies, Cary 5000). A

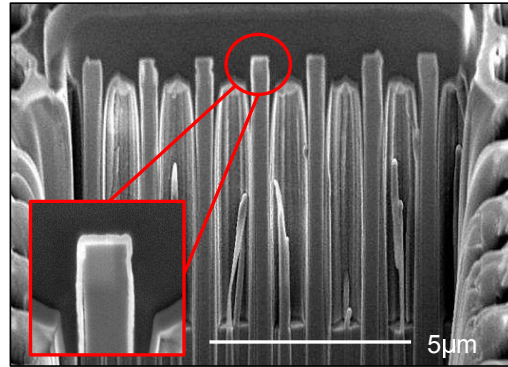


Figure 4-3: Ta 3% W sample fabricated with SiO_2 mask (with $a=1.37 \mu\text{m}$, $r=0.53 \mu\text{m}$, and $d=6.7 \mu\text{m}$): FIB cross section of the Ta 3% W photonic crystal after anneal at 1200°C for 24 hours in a vacuum furnace. Note that platinum was deposited prior to FIB milling in order to improve the cross-sectional imaging. The inset is a close up of the cavity wall.

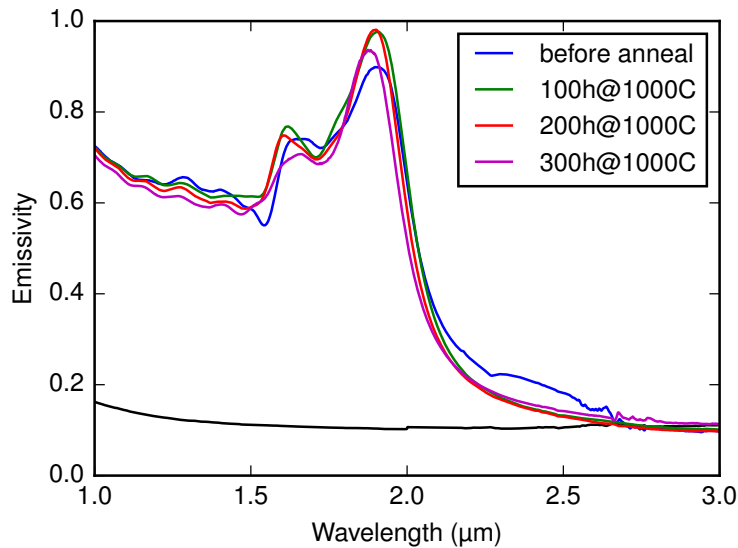


Figure 4-4: Different Ta 3% W sample fabricated with SiO_2 mask (with $a=1.3 \mu\text{m}$, $r=0.50 \mu\text{m}$, and $d=2.4 \mu\text{m}$): Measured normal emittance with a 20 nm HfO_2 coating before and after anneal at 1000°C compared with polished flat tantalum. The optical performance showed no degradation after 300 hours at 1000°C .

Table 4.1: Optical and geometric parameters of selected fabricated photonic crystals.

#	Substrate Material	Etch Mask	Optical Parameters (Normal)				Geometric Parameters			Ref.
			ε_{in}	ε_{out}	λ_c (μm)	k (μm^{-1})	a (μm)	r (μm)	d (μm)	
1	W	Cr ¹	0.848	0.138	2.11	13.5	1.40	0.55	1.61	[49]
2	Ta	Cr	0.869	0.147	1.95	18.6	1.17	0.52	6.79	[67]
3	Ta3%W	SiO ₂	0.833	0.115	2.04	17.8	1.23	0.54	4.89	[27]
4	Ta3%W	SiO ₂	0.938	0.089	1.85	14.0	1.11	0.47	6.68	
5	Sput. Ta	SiO ₂	0.944	0.126	1.60	6.5	1.05	0.40	1.75	[64]

custom code was employed to apply a linear correction, obtained with a least squared methodology, to the measurements, as described in detail in Appendix D. Using this technique, our fabricated photonic crystal was measured before and after anneal. As shown in Figure 4-4, the stability of our photonic crystal is exceptionally good with no deterioration for up to 300 hours at 1000°C.

4.2 Characterization

Although the optical performance of an emitter is fully described by its emissivity, it is useful to use average in-band and average out-of-band emissivities for comparisons. The emissivity can be approximated by a sigmoid function with four parameters: cutoff wavelength, average in-band emissivity, average out-of-band emissivity, and the slope of the transition between the two regions. A least squares fit of a sigmoid, weighted by a 1200°C blackbody, was applied to the measured normal emittance of different photonic crystals:

$$\varepsilon = \varepsilon_{in} - \frac{\varepsilon_{in} - \varepsilon_{out}}{1 + e^{-k(\lambda - \lambda_c)}} \quad (4.1)$$

where λ_c is the cutoff wavelength and k describes the sharpness of the cutoff.

Another fitting algorithm was developed for matching the geometric parameters of the fabricated photonic crystal to the measured reflectance, as described in detail in Appendix D.

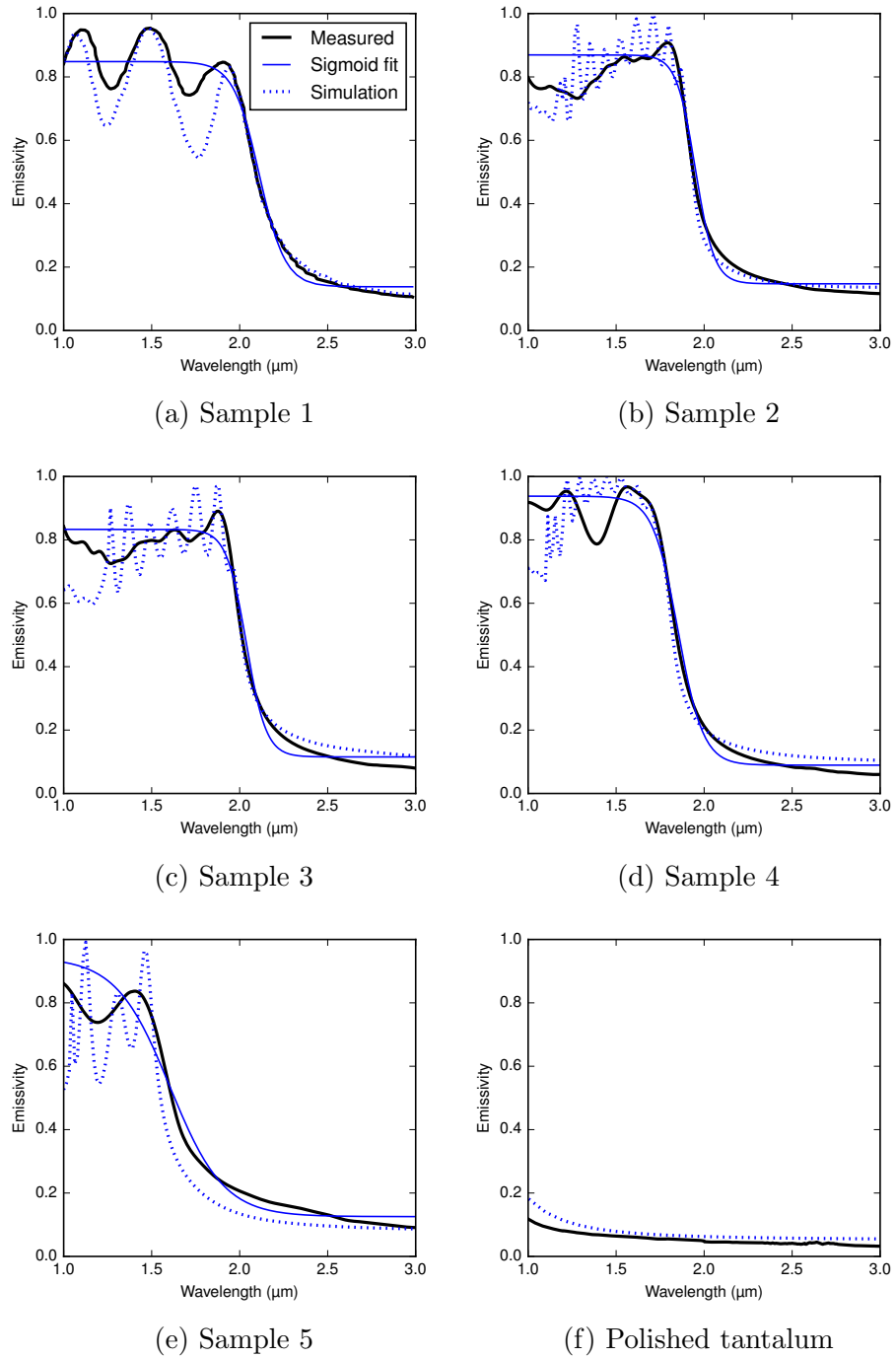


Figure 4-5: Measured and simulated normal emittance of different fabricated photonic crystals listed in Table 4.1 as well as that of polished tantalum. The sigmoid fit used to calculate the optical parameters is also shown.

4.2.1 High-Temperature Measurement

While all the reflectance measurements discussed previously were done at room temperature, it is possible to measure the thermal emission of the fabricated hafnia-passivated tantalum photonic crystals at high temperature, in a vacuum sealed heater with a calcium fluoride window facing the entrance of an FTIR, at normal incidence and different temperatures. Figure 4-6 shows the measured emission of a photonic crystal designed for a cut-off wavelength of 2 μm . The peak emission is below the target cut-off wavelength while emission at higher wavelengths ($\lambda \geq 3 \mu\text{m}$) is kept low, maximizing the in-band radiation. Determining the correct sample surface temperature is crucial in order to obtain the correct emissivity and the spectral efficiency. Yet this is very challenging to achieve experimentally at such high temperatures due to the small samples and large temperature gradients near the surface. Therefore we use the simulated emissivity near the fundamental resonant mode of the tantalum photonic crystal to estimate the surface temperature from the measured emission, a methodology developed by Yeng [49]. The sample temperature T can be calculated from the measured spectral emission L_S and the estimated emissivity ε of the fundamental resonance wavelength λ from the following equation:

$$T = \frac{hc}{\lambda k \ln \left(\frac{2hc\varepsilon}{\lambda^5 L_S} + 1 \right)} \quad (4.2)$$

where h is Planck's constant, c is the speed of light in vacuum, and k is the Boltzmann's constant. The relative uncertainty of the determined sample temperature $\Delta T/T$ can be approximated from the uncertainty of the emissivity $\Delta\varepsilon$ by:

$$\frac{\Delta T}{T} = \frac{\Delta\varepsilon}{\ln \left(\frac{2hc^2\varepsilon}{\lambda^5 L_S} + 1 \right) \left(\varepsilon + \frac{\lambda^5 L_S}{2hc^2} \right)} \quad (4.3)$$

The emissivity is simulated from the high-temperature material parameters obtained for tantalum, which has a small uncertainty ε and therefore T , resulting in a good

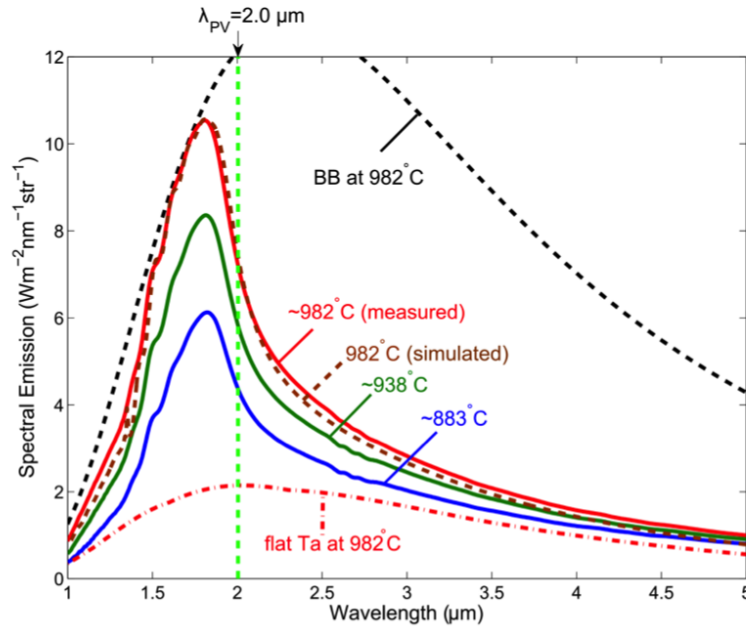


Figure 4-6: Measured normal spectral emission of a tantalum photonic crystal at different temperatures (solid lines), compared to its simulated emission (dashed line), the calculated emission of flat tantalum (dashed-dotted line), and calculated blackbody emission (dashed black line) at 982°C. (Reproduced from [39] with permission).

agreement between measurement and simulation of the spectral emission [39].

4.3 Morphology

The photonic crystals are imaged by SEM after fabrication to visually check the parameters, as well as after anneal to see if any degradation has occurred. In initial fabrication trials without coating, degradation of the surface occurred as quickly as after 3 hours at 900°C, which also caused a decrease in selectivity. However, in fabrication trials with the thin hafnia passivation layer (20 nm), the surface of the photonic crystal was fully preserved, and no decrease in optical performance, as shown in Figure 4-7. The star-like formations seen were the same tantalum carbide formation described in detail in Appendix B, where non-structured tantalum was studied with and without hafnia passivation before and after anneal.

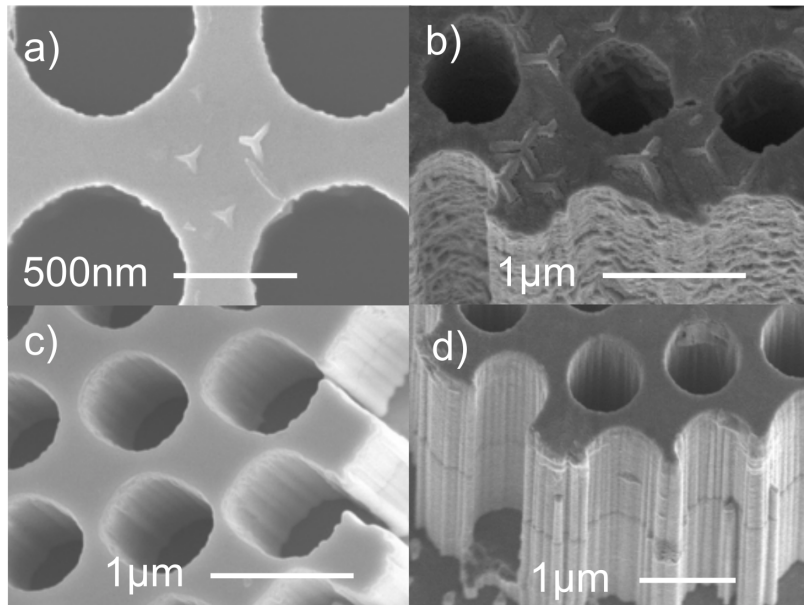


Figure 4-7: AES imaging without hafnia passivation layer: (a) beginning TaC formation after 3h anneal at 900°C, (b) after 24 hours at 900°C. SEM imaging with hafnia passivation layer: (c) before heating, (d) after 144 hours at 900°C.

Chapter 5

Omnidirectional Emissivity Improvement

The hafnia as a passivation layer, discussed in Chapters 4 and 3, generated significant interest in metal dielectric structures. Filling the cavities of the photonic crystal completely with a dielectric was proposed initially to improve thermal stability leading to the discovery of an unintended benefit of such a structure: hemispherically averaged emissivity improvement [53, 68]. Simulations showed that a dielectric filled 2D photonic crystal could overcome the narrow angular emission of the current photonic crystal, thus increasing the overall energy conversion efficiency and power density of TPV systems. Indeed a filled-cavity photonic crystal increases the efficiency directly by increasing the spectral selectivity and indirectly by altering the heat-balance.

5.1 Physics and Design

Because of the higher index of refraction, the optical diameter of the dielectric filled cavities can be maintained while reducing the physical diameter. A smaller physical diameter shifts the short wavelength diffraction cutoff at all angles. On the other hand, keeping the optical diameter the same maintains the desired long wave-

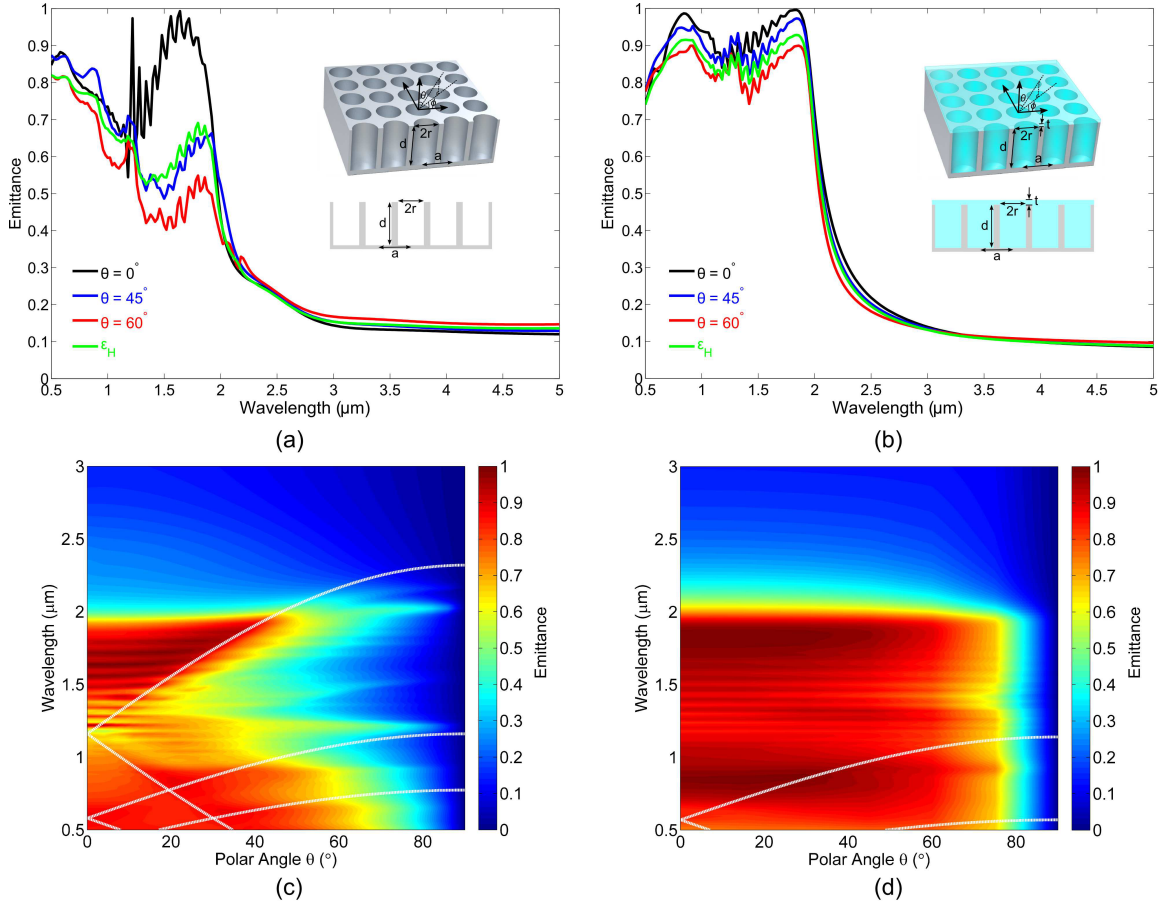


Figure 5-1: Emittance ε as a function of wavelength λ and polar angle θ averaged over azimuthal angle ϕ and over all polarizations for optimized (a) 2D TaPhC ($r = 0.53 \mu\text{m}$, $d = 8.50 \mu\text{m}$, $a = 1.16 \mu\text{m}$) and (b) HfO₂-filled ARC 2D TaPhC ($r = 0.23 \mu\text{m}$, $d = 4.31 \mu\text{m}$, $a = 0.57 \mu\text{m}$, $t = 78 \text{ nm}$). Both are optimized for $\lambda_c = 2.00 \mu\text{m}$. HfO₂ is depicted by the cyan colored areas in the inset, and ε_H is the hemispherically averaged emittance. Contour plots of $\varepsilon(\lambda, \theta)$ are also shown for optimized (c) 2D TaPhC and (d) HfO₂-filled ARC 2D TaPhC. White lines indicate the diffraction thresholds defined by $\theta_d = \sin^{-1}(\lambda/a - 1)$. (Reproduced from [53] with permission)

Table 5.1: Parameters used during the HfO₂ ALD process using TDMAH precursor to fill the cavities of the photonic crystal.

Process	Chamber temperature (°C)	Precursor temperature (°C)	N ₂ carrier flow (sccm)	Base pressure (mTorr)
ALD	200	65	20	200

length cutoff. Hafnium oxide, again, is the dielectric material of choice because of its transparency in the visible and infrared region, its compatible thermal expansion coefficient, and its stability at high temperatures.

5.2 Fabrication and Characterization

A filled cavity photonic crystal was fabricated, using the optimized parameters found in [53], following the same process as detailed in Chapter 3 but depositing the conformal HfO₂ coating by ALD until the cavities were filled (~ 2700 cycles, TDMAH precursor at 60°C). A shallower hole depth was chosen than in the optimized depth shown in Figure 5-4 (1.5 μm instead of 4.3 μm) to facilitate the filling process. The fabricated photonic crystal was measured by SEM and found to have a period $a \sim 0.5 \mu\text{m}$, radius $r \sim 0.2 \mu\text{m}$, and cavity depth $d \sim 1.5 \mu\text{m}$ before filling, as shown in Fig. 5-2 (a) and (b). The surface of the photonic crystal during filling is shown in Fig. 5-2 (c) and (d). The filling of the holes was found to be relatively uniform, as shown in Fig. 5-2 (e) and (f) in cross-section, however a small portion of the cavity was not filled, and a thick layer of HfO₂ formed at the surface of the photonic crystal corresponding to about the radius.

In simulations, the unfilled photonic crystal was found to have effective (least squares fit of sigmoid with 1200°C blackbody weighting) hemispherical in-band emissivity of 0.594 and out-of-band emissivity of 0.168 whereas a photonic crystal with

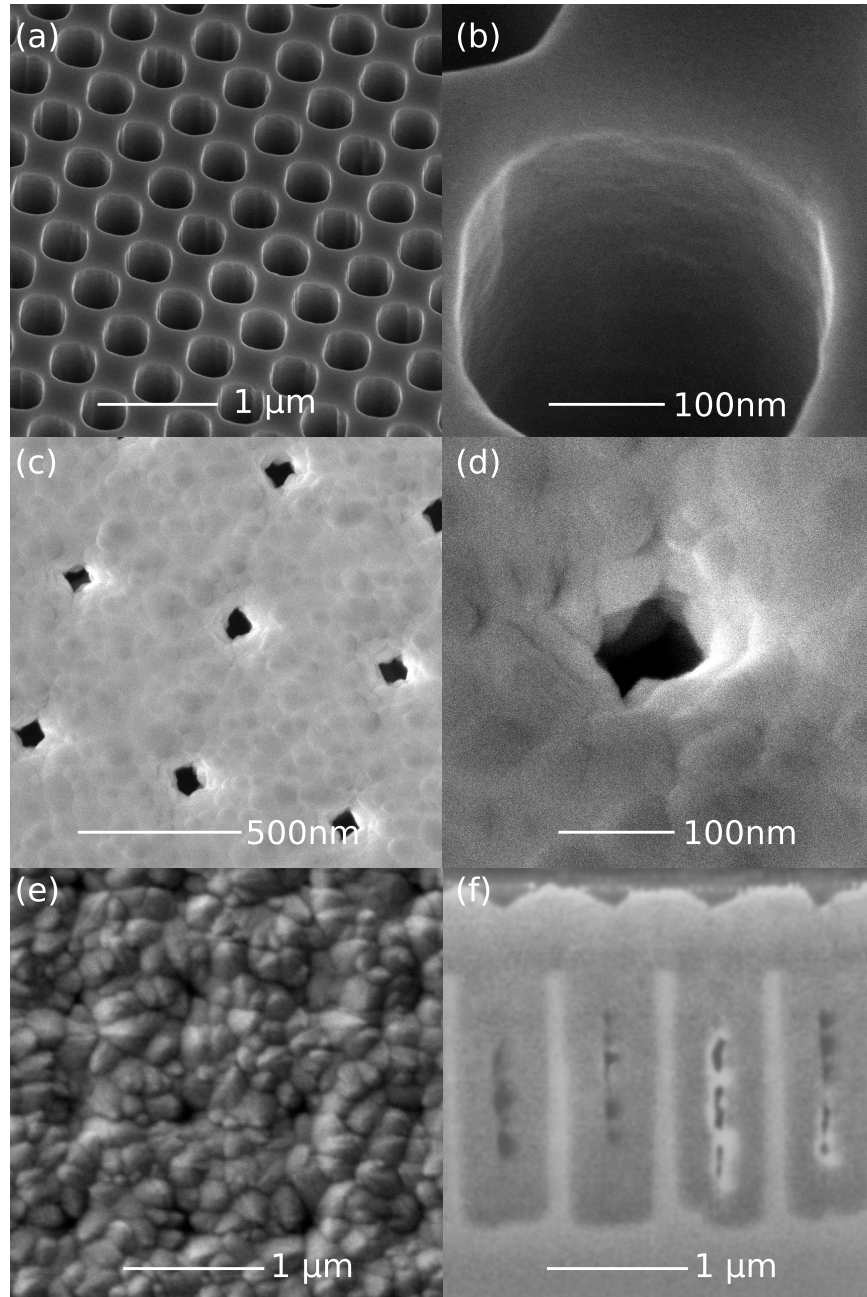


Figure 5-2: SEM micrographs of the photonic crystal (with $a=0.5 \mu\text{m}$, $r=0.2 \mu\text{m}$, and $d=1.5 \mu\text{m}$) (a) (b) before, (c) (d) during, and (e) after filling of the cavities with HfO_2 by ALD. (f) Cross section after filling.

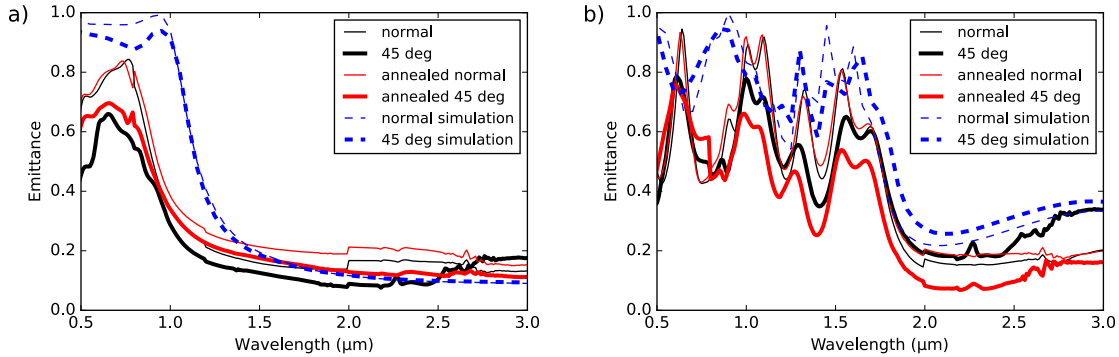


Figure 5-3: Normal and 45° incidence measurements (before and after anneal at 1000°C for 24 hours) of the (a) unfilled and (b) HfO₂-filled photonic crystals (with $a=0.5 \mu\text{m}$, $r=0.2 \mu\text{m}$, and $d=1.5 \mu\text{m}$) compared with their normal incidence and hemispherically averaged simulations.

HfO₂ filled cavities would have an in-band emissivity of 0.922 and out-of-band emissivity of 0.154, corresponding to a 55% increase in in-band emissivity without a change in out-of-band emissivity [53]. Thus, in an unfilled photonic crystal, the emissivity at 45° (approximately the hemispherically averaged emissivity) is about half of that at normal incidence, but in a filled photonic crystal the two emissivities are about equal. As shown in Fig. 5-3 (b), the peak normal in-band emittance of our fabricated filled photonic crystal was 0.9, and the 45° peak in-band emittance was 0.8, while the out-of-band emittance approached the emissivity of flat Ta. A sharp cutoff was observed in the desired wavelength range. The measured emittance of the photonic crystal matched the simulated emittance relatively well, as shown in Fig. 5-3, however, the emittance was overall lower than expected.

The cause for the lowered performance was believed to be the unoptimized layer on the top surface of the photonic crystal, in addition to the shallower cavities than the optimized design. Indeed, as shown in Figure 5-4, simulations predict a secondary peak centered at about 3 μm for a top thickness of 300 nm. Two approaches were considered for the removal of the top layer: chemical mechanical polishing/planarization(CMP) and Ar sputtering. The first process uses an abrasive and

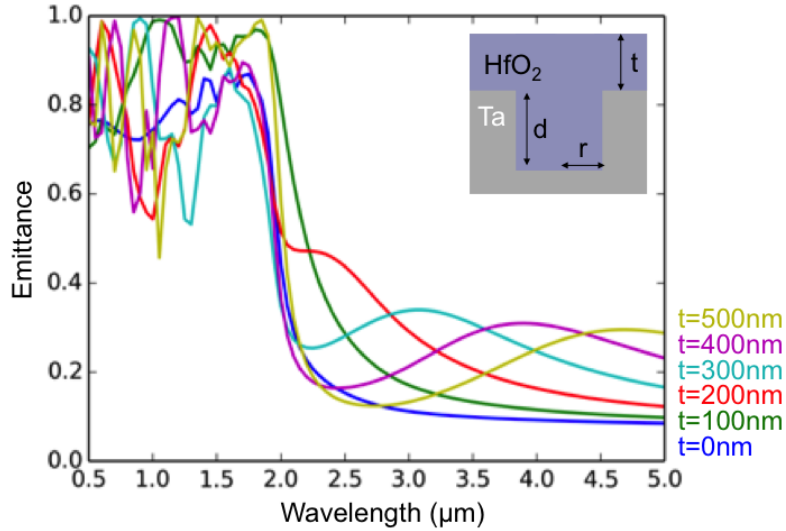


Figure 5-4: Varying t in optimized simulation for filled photonic crystal at normal incidence (with $a=0.57\mu\text{m}$, $r=0.23\mu\text{m}$, and $d=4.31\mu\text{m}$).

corrosive chemical slurry in conjunction with a polishing pad, and was deemed unsuitable due to contamination and difficulty in precisely removing materials on the nanometer scale. The latter, Ar sputtering, was investigated. Despite being very resistant to chemical etching, a 100 nm HfO_2 layer was successfully removed on passivated Si wafers at a rate of about 20 nm per minute. Argon was also found to damage the cavity walls of the photonic crystal if the hafnia was completely removed. Thus an optimized recipe was developed: another filled photonic crystal was fabricated using the Ar etch back method, followed by an additional conformal deposition of 20 nm of HfO_2 . While the performance in the long wavelengths was improved, as anticipated, with this fabrication method, more work needs to be done to improve the performance in the shorter wavelengths, as shown in Figure 5-5, attributed in part to the shallower cavities than the optimized design. Nevertheless, this work demonstrates that dielectric filling can improve the hemispherical performance of our 2D photonic crystal selective emitter without sacrificing stability or ease of fabrication, allowing for further increase in TPV system efficiencies.

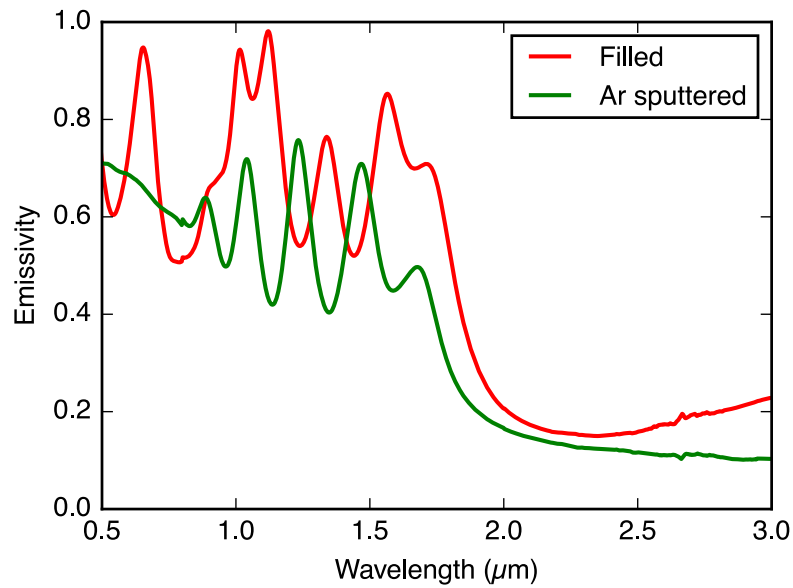


Figure 5-5: Comparison of the emittance of two filled photonic crystals with the same geometric parameters ($a=0.5 \mu\text{m}$, $r=0.2 \mu\text{m}$, and $d=1.5 \mu\text{m}$): (red curve) fabricated by ALD filling only, (green curve) fabricated by ALD followed by Ar etch back and another thin ALD layer.

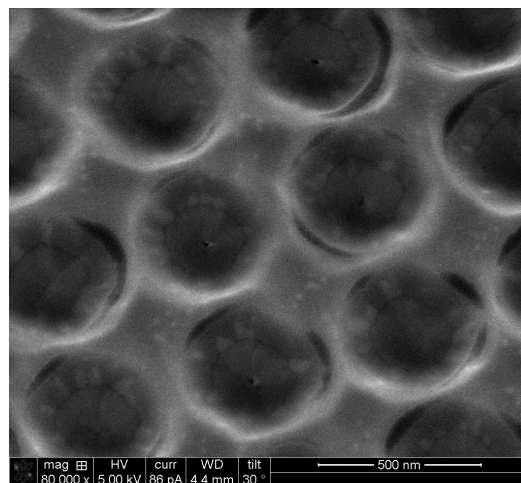


Figure 5-6: Filled photonic crystal after Ar etch back.

Chapter 6

System Integration

In addition to the demonstration of large area fabrication, thermal stability, and optical performance, a practical selective emitter must be integrated with the heat source, the Inconel microcombustor in this case. Two integration methods are discussed: a monolithic sputtered tantalum photonic crystal on an Inconel substrate and a bulk tantalum photonic crystal brazed on an Inconel microcombustor. Inconel was chosen as the substrate because of its high temperature oxidation resistance, which is needed for a microcombustor. Photonic crystal sputtering was successfully demonstrated on an Inconel coupon and photonic crystal brazing was successfully demonstrated with an Inconel microcombustor in a real TPV system.

6.1 Integration by Sputtering

A 2D photonic crystal was fabricated in a sputtered tantalum coating on Inconel for use in a monolithic TPV system, shown schematically in Figure 6-1. Using the 30 μm sputtered tantalum coating characterized in our study described in Appendix C as the substrate, the 2D photonic crystal was fabricated by the same fabrication steps as described in Chapter 3. The selective emitter was designed for a TPV system using a GaSb TPV cell with a bandgap corresponding to a cutoff wavelength of 1.7 μm .

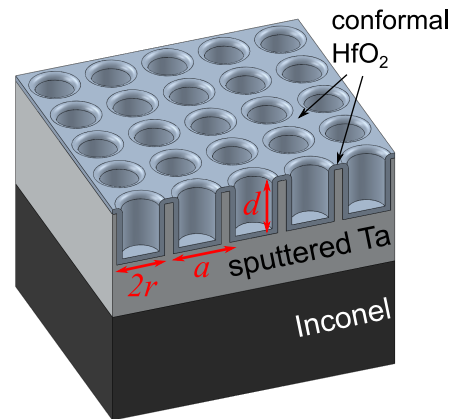


Figure 6-1: Schematic representation of a photonic crystal fabricated in tantalum sputtered directly on Inconel.

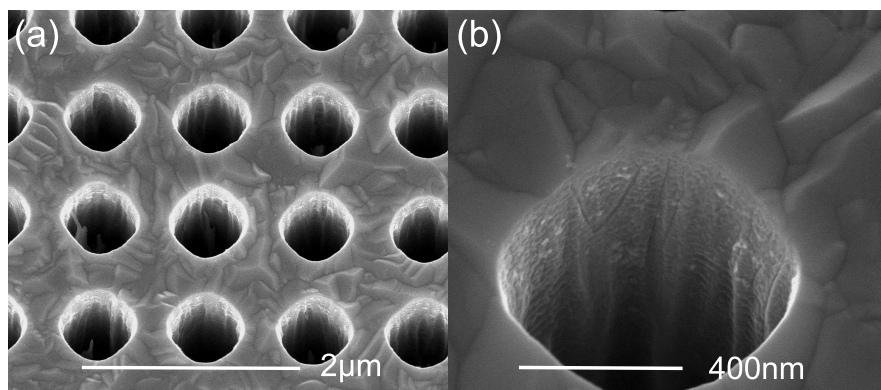


Figure 6-2: Micrographs of the photonic crystal fabricated in the tantalum sputtered coating, before the hafnia conformal coating deposition and before annealing.

The fabricated 2D sputtered tantalum photonic crystal coating was measured by SEM and found to have a period $a \sim 1 \mu\text{m}$, radius $r \sim 0.3 \mu\text{m}$, and cavity depth $d \sim 3 \mu\text{m}$, as shown in Fig. 6-2. A sharp cutoff in the spectral emissivity was observed in the desired wavelength range. The in-band emittance was increased to almost the blackbody limit, while the out-of-band emittance approached the emissivity of flat tantalum. The measured emittance of the photonic crystal was matched to the simulated (room temperature) emittance, and was found to be in best agreement with $a = 1.01 \mu\text{m}$, $r = 0.35 \mu\text{m}$, and $d = 2.5 \mu\text{m}$, as shown in Fig. 6-3(a).

The cutoff wavelength was measured to be $1.65 \mu\text{m}$, which is very close to the bandgap of a GaSb TPV cell. The emittance of the fabricated sputtered photonic crystal emitter after the conformal hafnia coating deposition is shown in Fig. 6-3(a) compared to the emittance of an emitter fabricated in bulk tantalum tuned for a similar cutoff wavelength, as well as the simulated emittance for the sputtered photonic crystal coating. The selective emitter previously fabricated in bulk tantalum had an average normal in-band emittance of 97.6% and average normal out-of-band emittance of 18.1%. The average normal in-band emittance of our fabricated sputtered photonic crystal was found to be 84.5% and the average normal out-of-band emittance was found to be 12.7%. Thus, this is a very promising initial performance for a sputtered 2D photonic crystal selective emitter for high-temperature applications. In order to characterize the optical properties as a function of temperature, the photonic crystal coating was annealed for one hour at 700, 900, and 1100°C and 24 hours at 900°C in a quartz-lined Inconel tube furnace in vacuum (5×10^{-6} Torr) to prevent oxidation, at a slow heating and cooling rate of 5°C/minute. The emittance of the selective emitter fabricated in the hafnia coated 30 μm tantalum coating before and after the anneals was characterized, as shown in Fig. 6-3(b), and compared to the flat sputtered coating and flat bulk tantalum, measured at room temperature. The optical properties of the selective emitter remained remarkably stable even after annealing for 24 hours at 900°C. No damage, such as cracking or delamination, in the

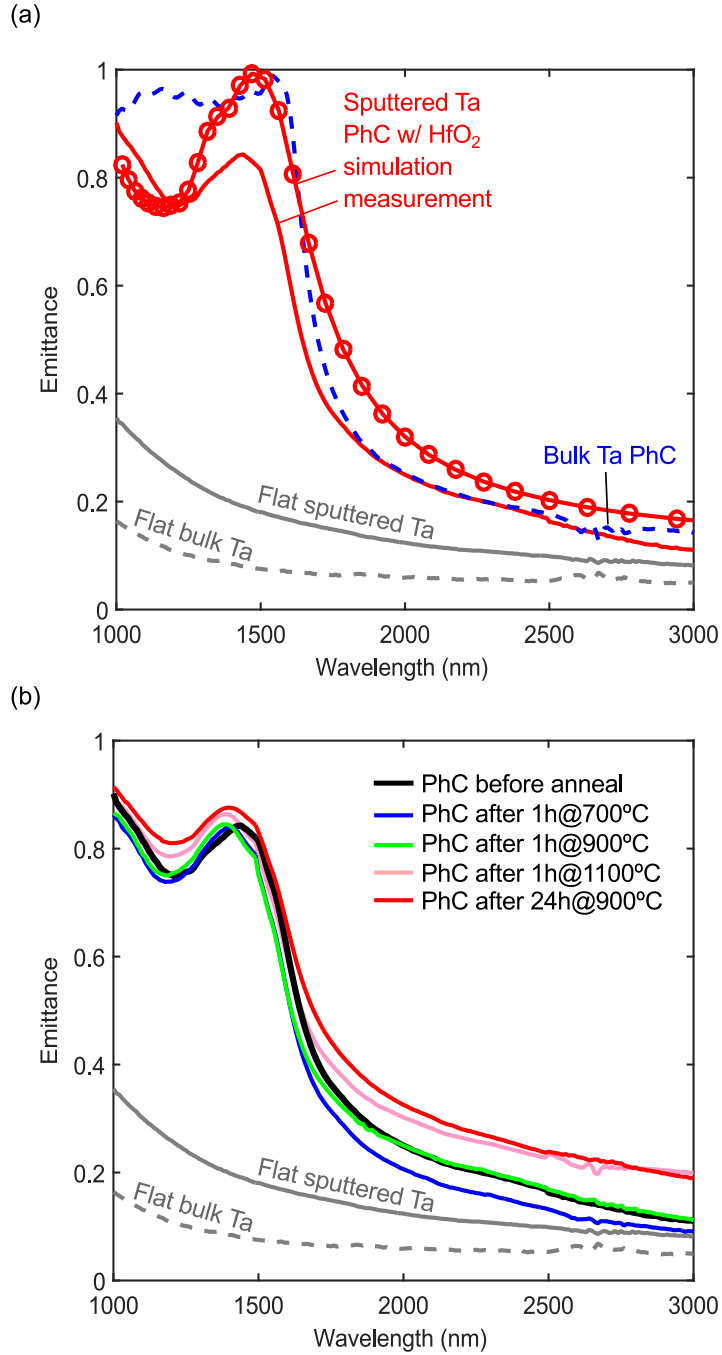


Figure 6-3: (a) Emittance of the fabricated sputtered 2D photonic crystal coating after conformal hafnia deposition compared to the flat (as deposited) sputtered tantalum coating, flat (as received) bulk polished tantalum, and photonic crystal simulation (room temperature tantalum emissivity, $a = 1.01 \mu\text{m}$, $r = 0.35 \mu\text{m}$, and $d = 2.5 \mu\text{m}$, coated). (b) Emittance of the fabricated sputtered 2D photonic crystal coating after the conformal hafnia deposition before and after annealing compared to the flat (as deposited) sputtered tantalum coating, and flat (as received) bulk polished tantalum.

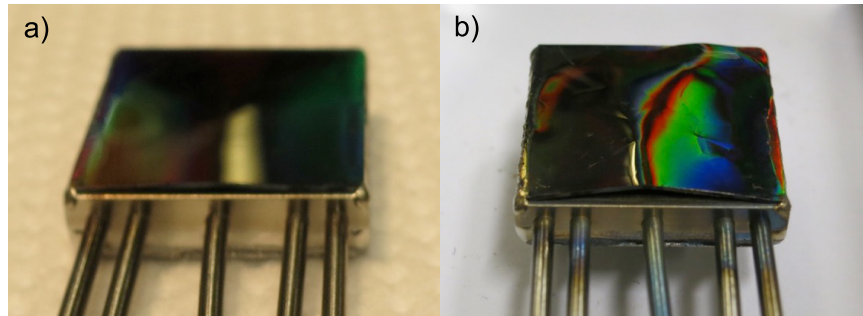


Figure 6-4: Welded photonic crystal before and after running burner at 900°C.

surface or microstructure was observed from visual inspection of micrographs after annealing. Overall, the results of this study suggest that thick tantalum coatings are a promising alternative to bulk substrates as a relatively low-cost and easily integrated platform for nano-structured devices in TPV systems.

6.2 Integration by Welding and Brazing

The experimental demonstration of the integrated TPV system required the design and fabrication of a microcombustor as well as the experimental apparatus, shown in Figure 6-5(a) and (b). Pure oxygen was used in the combustion reaction to emulate exhaust recuperation, which is required in a portable, air-breathing system. Propane and oxygen entered the microcombustor through the inlet tubes, flowed through an internal serpentine channel where they reacted on the catalyst-coated walls (5% platinum on porous alumina), and exited through the outlet tube [69]. Heat was conducted through the channel walls to the photonic crystal emitters bonded to the top and bottom surfaces of the microcombustor, as shown in Figure 6-5(c) and (d). The photonic crystal emitted spectrally confined thermal radiation matched to the InGaAs cells ($\lambda_{PV} = 2.0 \mu\text{m}$) mounted below the assembly [70]. The experiment was housed in a custom vacuum chamber to suppress convection and prevent degradation of the photonic crystal by reaction with air. A window was used in place of the top set of cells.

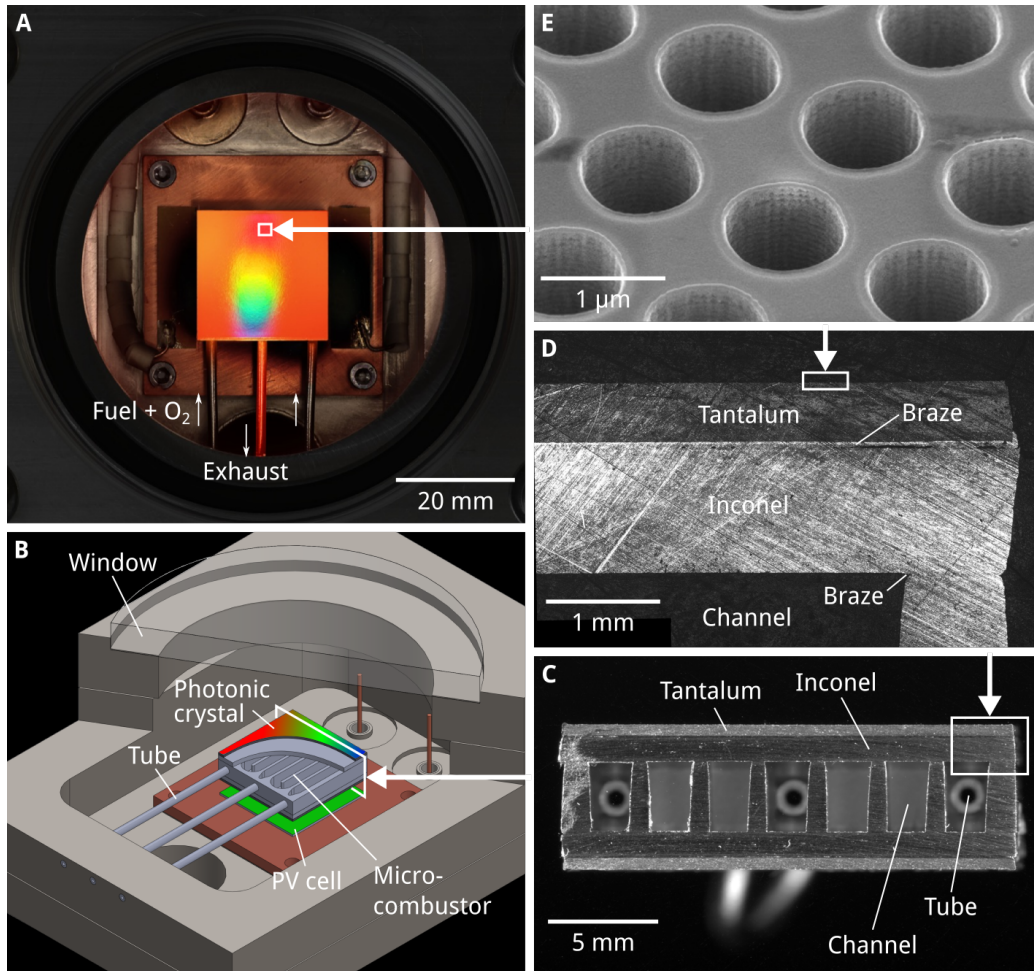


Figure 6-5: (a) Photograph of the experimental setup during operation, where a diffraction pattern is visible on the photonic crystal from the ambient light. (b) Cut-away drawing of the experimental setup with labeled components. (c) Cross section of the microcombustor with unstructured tantalum substituted for the photonic crystal. (d) Optical micrograph of the corner of the Inconel microcombustor, with the diffusion brazed joint between the Inconel and tantalum visible. (e) Scanning electron micrograph of the surface of the photonic crystal.

A microcombustor was characterized with and without a photonic crystal emitter. For the microcombustor without the photonic crystal, the bare Inconel surface was oxidized by operation in air until visibly black (emissivity of $\varepsilon \approx 0.8$) and used as the emitter. Electrical measurements are shown in Figure 6-6, scaled for a full set of cells. We measured a 1.5% with the oxidized Inconel emitter, for a fuel input of 100 W.

In our initial integration attempt, the photonic crystal was welded onto the microcombustor on 3 of the 4 edges of the microburner. However as shown in Figure 6-4, the photonic crystal bowed after running the burner at 900°C, significantly reducing the performance of the system due to heat losses caused by the gap between the source and emitter. Only a 2.4% fuel-to-electricity conversion efficiency was measured with the welded photonic crystal emitter, due to bowing.

Another integration of the photonic crystal with the microcombustor was then developed: we adopted the industrial process of diffusion brazing, as shown in Figure 6-5. An unprecedented 4.3% fuel-to-electricity conversion efficiency was measured with the brazed photonic crystal emitter for a fuel input of 100 W, as shown in Figure 6-6.

However, the simulations, summarized in Table 6.1, indicated that higher in-band emissivity of the photonic crystal could proportionally decrease the heat loss from the microcombustor edges and other microcombustor heat loss mechanisms. Therefore a mechanism for the improvement of the hemispherical emissivity of the photonic crystal was investigated in Chapter 5. Indeed, although at normal incidence the photonic crystal has near blackbody in-band emissivity, the wavelength-averaged in-band emissivity is only $\varepsilon_{in} = 0.59$, when averaged over all angles. By filling the cavities with a dielectric material, hafnium dioxide, we can increase hemispherical in-band emissivity by several mechanisms: the physical and optical dimensions of the cavity are decoupled, allowing us to decrease the period and move the onset of diffraction well below the wavelength range of interest, even at oblique angles; and the optical density of states is increased and additional resonant peaks are created,

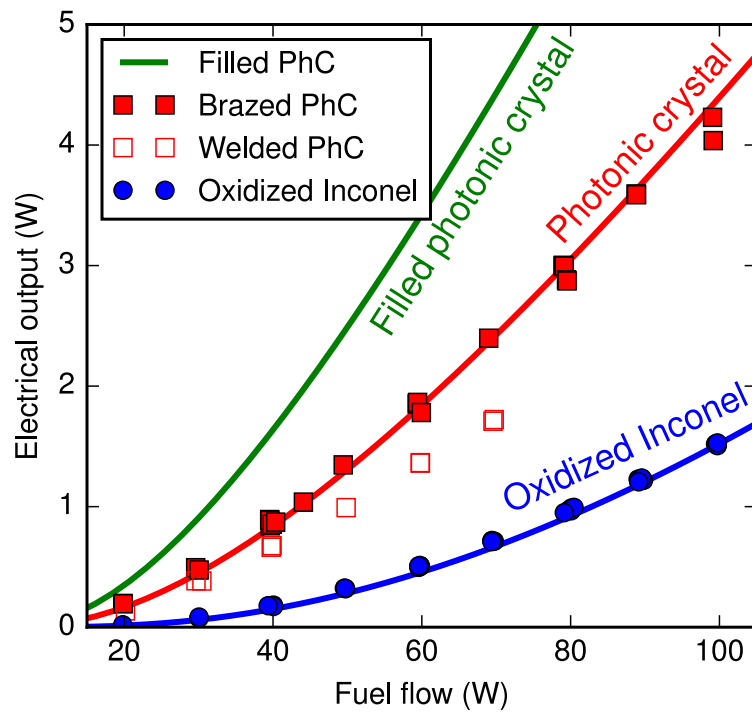


Figure 6-6: Measured (points) and simulated (lines) electrical power output as a function of fuel flow. The filled photonic crystal (green lines) offers the potential for an electrical power output of 12.6 W at 100 W of fuel flow (not shown), according to simulations. In both the oxidized Inconel and brazed photonic crystal cases, the experimental results matched very closely the predicted results.

Table 6.1: The simulated systems with the oxidized Inconel emitter, photonic crystal emitter, and filled photonic crystal emitter. The hemispherically averaged in-band and out-of-band emissivities of the emitters, edge emissivity, power distribution, efficiency, and temperature are listed.

Emitter	Oxidized Inconel	PhC	Filled PhC
Emitter emissivity ($\varepsilon_{in}/\varepsilon_{out}$)	0.80/0.80	0.58/0.18	0.92/0.16
Edge emissivity	0.80	0.55	0.15
Fuel	100 W	100 W	100 W
Exhaust	15.2 W	19.7 W	22.2 W
Conduction	3.6 W	4.6 W	5.1 W
Side radiation	27.3 W	32.8 W	12.5 W
View factor loss	4.8 W	3.6 W	5.4 W
Out-of-band radiation	46.9 W	24.5 W	15.2 W
Cell inefficiencies	4.3 W	10.6 W	27.1 W
Electricity	1.5 W	4.4 W	12.6 W
Fuel-to-electricity efficiency	1.5%	4.4%	12.6%
Temperature	843°C	1054°C	1169°C

further increasing the in-band emission. A fuel-to-electricity efficiency of 12.6% at 100 W of fuel input is predicted [1], as shown in Figure 6-6, which is several times higher than heat-to-electricity conversion methods previously reported.

Chapter 7

Conclusion

In this chapter, we compare the optical performance, thermal stability, and fabrication scalability of our photonic crystal to other selective emitters from the literature. We confirm our hypothesis that our approach is the only practical TPV emitter. We conclude by summarizing the contributions and by recommending future work.

7.1 Emitter Comparaison

In this work, we developed a better figure of merit to quantify the optical performance of various selective emitters, including ours, in our hydrocarbon TPV system: the ratio of total in-band radiation to input fuel flow (η_{hs}). Indeed, the common figures of merit described in Appendix C.3, spectral selectivity (η_{sp}), effective in-band emissivity (ε_{in}), or useful emitted power density (P_{out}) do not necessarily reflect the emitter's performance in a real TPV system. For example, a blackbody has the maximum possible in-band emissivity but a low spectral efficiency. A delta function can have perfect spectral efficiency but near-zero effective in-band emissivity. Thus, in order to more accurately understand the requirements of the emitter, we developed a simple system model of the hot side (burner and emitter) of a combustion driven TPV system, as shown in Fig. 7-2(c) [71]. We assumed that the hot side was perfectly

thermally insulated from the environment with the exception of thermal radiation from the emitter and the fuel, air, and exhaust flows necessary to sustain combustion. In the model, a 2 μm cutoff was used to represent an InGaAs TPV cell in the system; however we did not account for the efficiency of the cell.

A detailed description of the model is provided in Appendix D. In summary, the combustion efficiency η_c , spectral efficiency η_{sp} , and hot side efficiency η_{hs} are defined as:

$$\eta_c = \frac{Q_{rad}}{Q_{fuel}} \quad (7.1)$$

$$\eta_{sp} = \frac{Q_{in}}{Q_{rad}} \quad (7.2)$$

$$\eta_{hs} = \eta_c \times \eta_{sp} \quad (7.3)$$

where Q_{rad} is the total (in-band and out-of-band) radiation, Q_{fuel} is the caloric content of the fuel, and Q_{in} is the in-band radiation. In the case of the blackbody emitter, the combustion efficiency drops as the fuel flow (heat input) increases because a larger portion of the heat of combustion is carried out of the exhaust at higher temperatures. The spectral efficiency increases as the fuel flow increases because the higher temperature increases the in-band radiation. Indeed, the net effect of increasing fuel flow is an increase in hot side efficiency.

We compiled emissivity data for various emitters, as shown in Figure 7-2(a). Using our simple model, we calculated the hot-side efficiency for each emitter, as shown in Figure 7-2(b). Table 7.1 shows the hot side efficiency and temperature of the emitters for 10 W/cm^2 of fuel input. We also show their size and annealing conditions, if available.

The 2D W array of squares [73] or inverted pyramids [46] generally predicts good efficiency; however, this type of emitter is difficult to fabricate, particularly at large scales. Also, most emitters here are shown at normal incidence, with poor thermal stability, and small size.

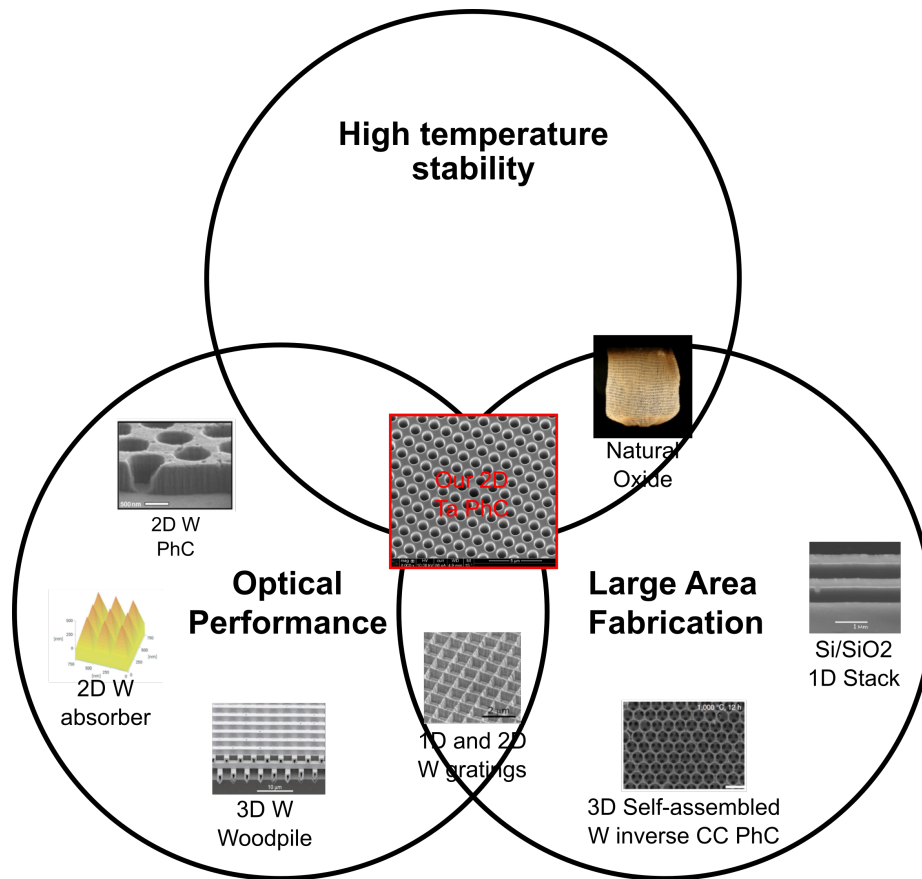


Figure 7-1: There are three main requirements for a practical TPV selective emitter: (1) Optical performance, (2) High temperature stability, and (3) Large area fabrication and integration. Photonic crystals fabricated as 1D, 2D, and 3D structures or metamaterials [33,42,44–47] enable higher system efficiencies by tailoring the photonic density of states to produce spectrally confined selective emission of light [30,48–50]. None of these approaches to selective emitters meet all the criteria for a practical TPV selective emitter.

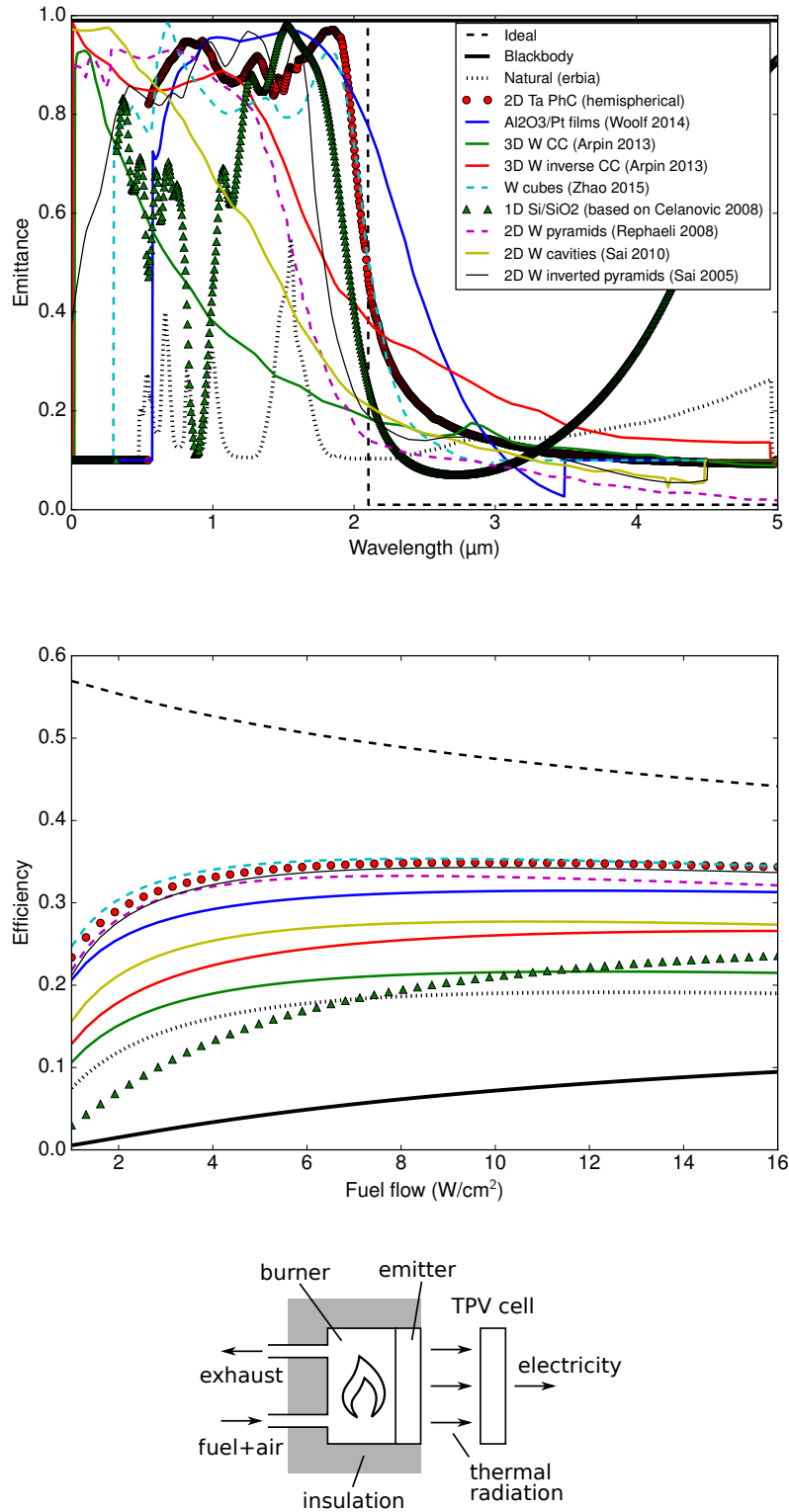


Figure 7-2: (a) Emittance and (b) efficiency of different emitters in a simple TPV system. (c) Simple TPV system model used for simulations above.

Table 7.1: Hot side efficiency (η_{hs}) and temperature (T) of different experimentally demonstrated emitters in a TPV system with a 10 W fuel input, compared with and ideal selective emitter and blackbody emitter in the same system, organized by highest to lowest η_{hs} .

#	Emitter	Hot side η_{hs} (%)	Emitter T (K)	Size (cm ²)	Anneal Time (h)	Anneal T (K)	Ref.
1	Ideal	47.4	1365				
2	Ta 2D cavities	34.9	1330	20	300	1273	[1]
3	Pt metasurface	31.4	1299	<1	0.083	1300	[72]
4	W 2D inverted pyramids	27.7	1448	<1	5	1170	[73]
5	W 3D inverse CC	21.5	1487	>1	12	1473	[35]
6	Si/SiO ₂ 1D stack	21.0	1268	>20	0.333	1073	[?]
7	Natural (Erbia)	19.0	1525	>20	>300	> 1500	[55]
8	Blackbody	7.2	1054				

Our 2D photonic crystal design exceeds the optical performance of all other experimentally demonstrated selective emitters. It exceeds by an order of magnitude the runtimes previously demonstrated for thermal stability, with no visible degradation for as long as 300 hours at 1000°C, as described in Chapter 4. It is the only engineered emitter, other than the Si/SiO₂ stack, fully integrated with a source of heat, as described in Chapter 6.

7.2 Impact of this work

With our 2D photonic crystal, we experimentally demonstrated a record fuel-to-electricity conversion in a hydrocarbon TPV system of nearly 5% at 100 W of fuel input. With further fabrication improvements described in Chapter 5, a fuel-to-electricity efficiency of 12.6% is predicted at 100 W of fuel input, which is several times higher than heat-to-electricity conversion methods previously reported and paves the way for small scale portable power generation. Our 2D photonic crystal design is the only practical high temperature photonic crystal for high performance thermophotovoltaics available today.

7.3 Summary of Key Contributions

The fabricated bulk Ta 2D PhC with a 20 nm conformal hafnia coating enabled a first of a kind **experimentally demonstrated record fuel-to-electricity 4.5% system efficiency in a hydrocarbon TPV system**. A filled cavity photonic crystal will enable a fuel-to-electricity efficiency of 12.6% at 100 W of fuel input [1], as shown in Figure 6-6, which is several times higher than heat-to-electricity conversion methods previously reported. Specifically, my key contributions were:

- *Significantly improved spectral selectivity by optimizing fabrication process:* New Ta etch mask was developed: SiO_2 instead of the previously used Cr. The mask further minimized emission in the long wavelengths (due to residue from leftover Cr etch mask). Our photonic crystal design reaches 67% of the optical performance of an ideal emitter
- *Developed a passivation coating to prevent high temperature degradation:* The deposition of a conformal thin layer of HfO_2 as a thermal degradation barrier preserved the PhC's outstanding emittance selectivity, even after annealing for 24 hours at 1200°C and 300 hours at 1000°C , demonstrating that the coating effectively prevents degradation due to surface diffusion at high temperatures.
- *Enabled TPV system integration by developing a Ta-W alloy substrate material for PhC fabrication:* A tantalum-tungsten (Ta-W) solid solution alloy PhC was demonstrated as a spectrally selective emitter. The Ta 3% W alloy presented critical advantages compared to non-alloys as it combined better thermo-mechanical properties of W with the more compliant material properties of Ta, allowing a direct system integration path.
- *Investigated two sputtered coatings, W and Ta, as a substrate for 2D PhC fabrication:* The optical properties and thermo-mechanical stability of the coatings were characterized and the Ta sputtered coating was found to be a suitable

substrate as no cracking or delamination occurred.

- *Fabricated a first of a kind 2D PhC in sputtered Ta:* The optical performance and thermal stability were characterized, enabling a new level of system integration which would benefit all high-temperature TPV systems. In the hydrocarbon microcombustor application, the PhC can be sputtered directly on the burner minimizing heat losses and increasing efficiency. In STPV applications, the PhC coating can also be applied as an absorber/emitter.
- *Fabricated an improved PhC structure to enhance hemispherical emissivity:* A filled-cavity 2D PhC in bulk Ta was investigated to experimentally demonstrate the theoretical prediction that a HfO₂ filled PhC would have superior omnidirectional performance and could reach 73% of the performance of an ideal emitter. An initial PhC was fabricated, characterized and annealed for 300 hours at 1000°C.

7.4 Future Work

- In order to understand the long term thermal stability of our photonic crystals, both the conformally coated and the filled cavity designs need to be tested for long operational hours, 1000 hours at 1000°C, 10 000 hours at 1000°C, for example, and at 1200–1400°C for shorter periods of time. The photonic crystals' anneals should also be cycled, annealing 100 hours and cooling back down and annealing again 10 times for example. One critical question that must be answered in the future is *when, at what temperatures or after how many hours, does the photonic crystal fail?*
- The fabrication of the filled-cavity photonic crystal must still be improved further to better match the geometric parameters that predict 73% of the performance of an ideal emitter. Argon sputtering must be investigated further

to improve the process that removes the HfO_2 top layer without damaging the cavity walls. Alternative HfO_2 depositions methods should also be investigated.

- In regards to the passivation layer itself, a detailed optical characterization of HfO_2 should be performed. Other passivation coatings could potentially work in this application and should be investigated.
- Finally, a full system characterization of the burner with the fabricated filled-cavity photonic must be performed to verify the theoretical prediction that it will result in a higher fuel to electricity efficiency. Specifically, several 2×2 cm sets of filled-cavity photonic crystals should be fabricated in the Ta 3% W foil and integrated with the microcombustor by brazing. The hydrocarbon TPV system should then be experimentally characterized to demonstrate a fuel-to-electricity efficiency greater than 10%.

Appendix A

TPV Chronology

Table A.1: Thermophotovoltaics chronology: early developments.

1956	H. Kolm demonstrates the first TPV system at MIT Lincoln Lab, using a Coleman camping lantern with an incandescent gas mantle as the emitter and using Si PV cells as the receiver [74]. However, the natural selective thermal emitter at $>2000^{\circ}\text{C}$ is poorly matched to the cells used resulting in a low system efficiency.
1960	P. Aigrain is listed as the inventor of TPV [14]. Aigrain proposed this direct energy conversion concept during a series of lectures on a number of technical topics given while a visiting professor at MIT.
1961	D. White, B. Wedlock, and J. Blair, as well as P. Gray concentrate on Ge PV cell development at MIT [75–77]. R. Schwartz does so at at Purdue University [78, 79].
1960's	The US Army needs portable power sources with a low signature, especially low noise, and TPV is an excellent candidate for this service.
1960's	E. Kittl and, later, G. Guazzoni, at the US Army Fort Monmouth play key roles in advancing TPV, contributing to the growth of the technology in systems development [80] and basic materials studies.
1966	General Motors's Defense Research Laboratory actively participates in TPV development [81], introducing the concept of a photovoltaic back surface reflector for TPV spectral control [82].
1972	G. Guazzoni reports high temperature emittance of a group of rare earth oxides that are potential TPV emitter candidates [55]. The TPV system consists of a multi-fuelled burner with recuperation as the power source, a Si carbide emitter for spectral control, Ge PV cells and a water-cooled cell heat-sink with heat rejection at a forced-convection-cooled radiator.
1970's	The pace of TPV development significantly slows down when the US Army choses thermoelectric technology to satisfy the need for covert power sources. TPV development was not sufficiently advanced when compared with the older, more reliable thermoelectric approach. GM also discontinues TPV development. Fossil-fuel powered TPV development comes to a virtual halt.
1970's	Worldwide interest focuses on renewable energy sources, especially solar. In the US, the Electric Power Research Institute (EPRI) funds studies concerning the feasibility of coupling the output of solar-powered arrays into the utility grid. The benefit of a TPV approach is investigated to shift the solar spectrum to longer wavelengths to match better available photovoltaic cells [83, 84].

Table A.2: Thermophotovoltaics chronology: improving low bandgap TPV cells.

1980's	A prolonged effort on TPV research begins in Europe driven, most likely, by solar energy conversion incentives [85, 86].
1986	General Atomics Technologies proposes InGaAs PV cells for TPV applications [87].
1990	W. Horne's EDTEK Inc. and L. Fraas's JX Crystals Inc. license Boeing's Zn-diffused GaSb cell technology to fabricate commercially available TPV cells.
1990's (mid)	A significant TPV program for an undisclosed military application stimulates the development of low band gap cells at NREL, RPI, Sarnoff Corp., AstroPower Inc., and MIT Lincoln Laboratory. McDermott Technology Inc. and ThermoElectron's Thermo Power Corporation, are awarded TPV developmental contracts, but their participation ends by the end of the decade.
1994	First NREL Conference on TPV Generation of Electricity.
1999	High-quantum-efficiency 0.5 eV GaInAsSb/GaSb TPV devices [88] are grown on GaSb substrates by organometallic vapor phase epitaxy exhibiting external quantum efficiency as high as 60%.
2000's	Slowdown of TPV development in the US, offset by renewed interest in Europe, in particular at the Fraunhofer Institute for Solar Energy Systems and the Paul Scherrer Institut. Cite Fraunhofer papers [89–91].
2003	Monolithic interconnected modules (MIMs), which are series-interconnected photovoltaic cells on a common, semi-insulating substrate and generally including rear-surface infrared (IR) reflectors, are implemented in InGaAs [70].
2004	An InGaAs MIM using reflective spectral control is fabricated and measured in a thermophotovoltaic radiator/module system resulting in greater than 20% radiant heat conversion efficiency [19].
2006	InGaAsSb TPV diodes are grown lattice matched to GaSb substrates by metal-organic vapor phase epitaxy in the bandgap range of $E_g = 0.5\text{--}0.6$ eV [92].

Table A.3: Thermophotovoltaics chronology: improving spectral control.

1983	Gillette develops selective fibrous rare earth oxide emitters [93].
1990	D. Chubb develops further selective emitters at NASA-Lewis for space power applications [94].
2003	A 3D photonic-crystal emitter consisting of stacked W rods was fabricated using a modified silicon process [52].
2004	1D Si/SiO ₂ dielectric stacks are explored as selective emitters [51].
2004	Two-dimensional surface-relief gratings with a period of 1.0-0.2 μm composed of rectangular microcavities were fabricated on single crystalline W substrates [45].
2004-2007	Progress in cold side filters improves TPV efficiencies [23, 24, 95, 96].
2008	2D W photonic crystal from MIT [47].
2008	Coated silica woodpile structures, created using direct laser writing in tungsten or molybdenum, are characterized at 650°C [97].
2008	Theoretical paper proposes a W black absorber for solar light with wide angular operation range using a pyramid structure [46].
2011	Investigation of metal-coated carbon inverse opal photonic crystal structures fabricated by chemical vapor deposition (CVD) of refractory metals (tungsten, molybdenum, or tantalum), with a thin hafnia interlayer. The tungsten-coated photonic crystals were found to be stable after 1000°C for 5 h [42].
2013	A 2.5% fuel-to-electricity efficiency is demonstrated in a Si hydrocarbon TPV system with a Si/SiO ₂ stack emitter and InGaAsSb cells [11].
2013	3D tungsten-inverse colloidal self assembled photonic crystals protected with HfO ₂ can withstand 1400°C operation for 1 h and an HfB ₂ -coated colloidal crystal can withstand 1000°C for 12 h with decent optical performance [35].
2013	A Ta 3%W alloy photonic crystal is fabricated and characterized with great optical performance and high-temperature stability up to 24 h at 1200°C [27].
2014	A record solar TPV efficiency of 3.2% is obtained at MIT using a photonic crystal solar absorber and InGaAsSb cells [98].
2016	A record fuel-to-electricity efficiency of 4.5% is obtained at MIT in a hydrocarbon TPV system using a photonic crystal selective emitter and InGaAs cells [1].

Appendix B

Tantalum Substrates

Characterization

We characterized unstructured flat tantalum to understand the long term thermal stability of our selective emitter, by looking at the degradation of its optical properties. As described in Chapter 3, two kinds of samples were used: pure tantalum polycrystalline substrate samples with and without passivation. For the passivated substrate, a 20 nm film of HfO_2 was deposited by ALD. All the samples were annealed in a high vacuum quartz-lined Inconel tube furnace at 900°C for durations ranging from 6 to 48 hours. A mass spectrometer (Stanford Research Systems RGA100) directly attached to the furnace was used to dynamically measure the quality of the vacuum and identify the impurities present. During annealing, the vacuum pressure was consistently found to be on the order of 10^{-6} – 10^{-5} Torr, with the gas composition consisting primarily of carbon monoxide, as well as trace amounts of nitrogen.

After annealing, the surface morphology and topography of the samples was analyzed using SEM (JEOL 6700) and AFM (Veeco Dimension 3100). The grain size was also determined from micrographs using an intercept method. Additionally, the near-normal incidence reflectance was measured using a spectroradiometer (Gooch & Housego OL750) in the 1 to 3 μm wavelength range. Finally, changes to the surface

chemistry were monitored with a scanning Auger nanoprobe (Physical Electronics Model 700), which examined the oxygen, carbon, tantalum and hafnium peaks as a function of depth.

B.1 Unpassivated Polished Tantalum

The effects of annealing on the surface morphology and topography of unpassivated tantalum surfaces are exemplified in Figure B-1(a) and (b). In all samples, a large number of protrusions were formed, which had a characteristic three-pointed star shape. Similar formations have been reported at elevated temperatures in tantalum and niobium, and have been attributed to ion implantation [99–104], radiation exposure [105, 106], and chemical contamination [39, 107–109]. The “crow-foot” shapes, formed at elevated temperatures ($>700^{\circ}\text{C}$), were suspected of being oriented along the intersections of the surface and certain slip planes of the underlying material.

As the samples used in this study are unirradiated, it appears far more likely that the root cause of these formations is contamination. The results do corroborate the notion that the size and orientation of the structure’s branches depends on the underlying lattice. For instance, note that the three different types of structures in Fig. B-1(a) (marked 1’, 2’, and 3’) correspond to three different tantalum grains, with a noticeable pile-up of smaller star shapes near their boundaries. Additionally, the dimensions of these structures were found to vary significantly, as is clearly shown in Fig. B-1(b). In fact, AFM scans reveal heights ranging from below 10 nm to above 100 nm and widths of less than 20 nm to more than 500 nm. Moreover, increasing the annealing time did not cause a significant change to these dimensions, but instead increased the number of such precipitates until they began to overlap and saturate the surface.

A chemical analysis of unpassivated tantalum surface is shown in Figure B-2(a) and (b). The concentration depth profile in Fig. B-2(a), which extends to a depth

of approximately 50 nm, reveals that while the initial tantalum surface is free of any carbon or oxygen contamination, the star-shaped features are made up of a significant (roughly 20%) amount of carbon, with no oxygen. The Auger lineshape of this carbon is shown in Fig. B-2(b), and contrasting it with known carbon Auger peak shapes [110–116] reveals that it has the characteristic traits of a tantalum carbide, with major three peaks and minima at 249, 257, and 270 eV. Moreover, comparing the carbon content with well-known equilibrium phase diagrams [117–119] suggests that it consists of a M_2C carbide, as had been concluded from the Auger results of Thomas and Bauer [120]. Altogether, it appears that carbon contamination during annealing caused the precipitation of Ta_2C surface carbides that grow along preferential directions and thus produce a distinctive three-pointed star pattern.

The effects of these precipitates on the infrared reflectivity of the tantalum surface as a function of annealing time at 900°C is revealed in Figure B-3(a). The reflectivity is found to decrease significantly from an average value of 0.85 down to approximately 0.65 as the annealing time increases. This decrease is likely to be caused by an increase in the carbon content, as carbides have lower reflectivity than pure metals [57, 121–123] as well as increase in the roughness of the surface. Interestingly, the reflectivity decrease begins to slow down past 12 hours of annealing, indicating the saturation of the surface with carbon and carbon-based precipitates.

Finally, the growth of the tantalum grains was monitored as a function of annealing time, and is plotted in Figure B-4. No significant change in the grain size was detected. This finding is expected as studies of grain growth in tantalum do not reveal significant growth below approximately 1100°C ($T_M \sim 0.4$) [124–128], which is significantly higher than the operating temperature considered in this work (900°C). Therefore, unlike previous reports on refractory metals for high temperature photonic applications, these results suggest that grain growth may not be a relevant degradation mechanism at the temperatures of interest.

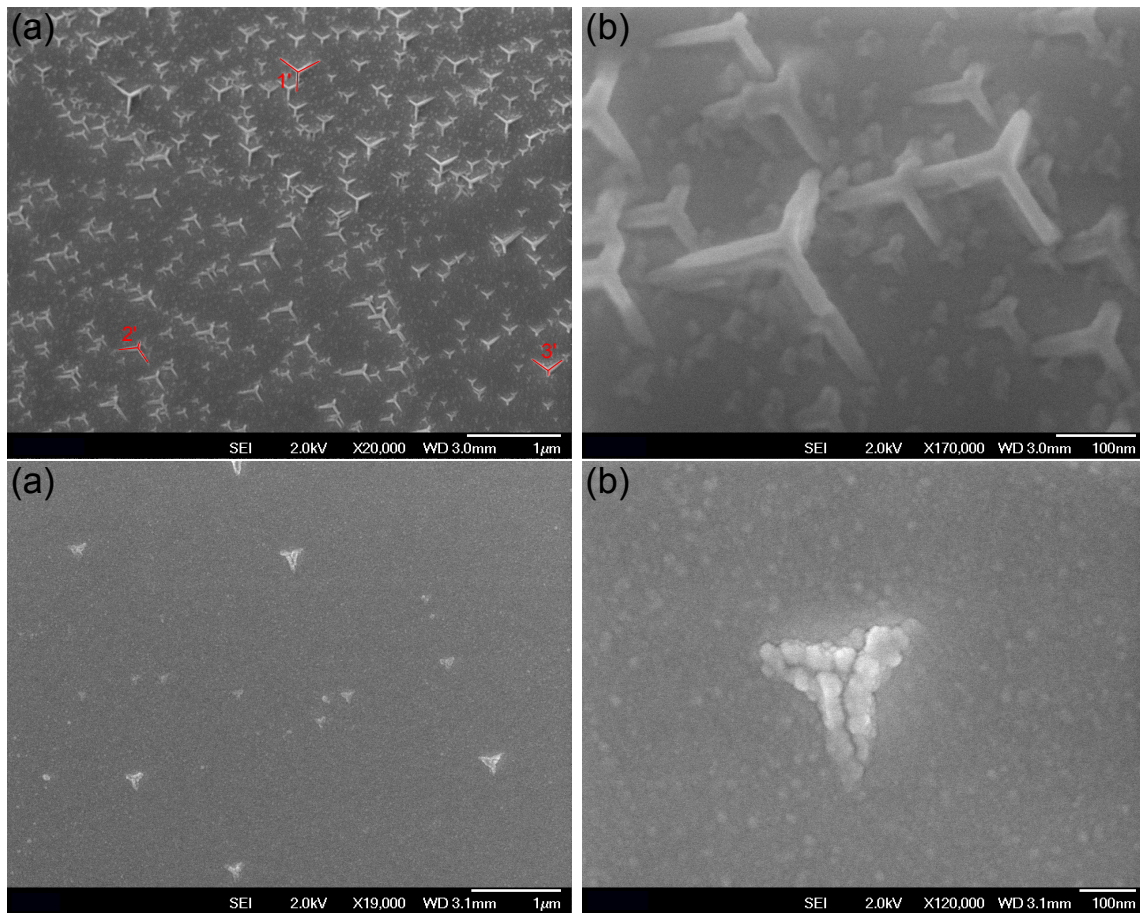


Figure B-1: (a) (b) Unpassivated tantalum surfaces after annealing for 6 hours at 900°C. (c) (d) HfO₂-passivated tantalum surfaces after annealing for 48 hours at 900°C.

B.2 Passivated Tantalum

The morphological changes caused by annealed tantalum surfaces passivated by a 20 nm film of hafnia are shown in Figure B-1(c) and (d). In this study, much fewer star-shaped structures were found. They appear to have similar dimensions as their unpassivated counterparts, and also appear to depend on the orientation of the underlying tantalum (notice that the features in Figure B-1(c) are all oriented in the same directions). The number of star-shaped structures is greatly diminished in comparison to the unpassivated Ta substrate anneal experiment: while the unpassivated surface revealed hundreds of such precipitates, this number decreases to a few dozen for the passivated surface.

Additionally, instead of the typical smooth thin elongated branches shown in Figure B-1(a), the features that develop on the HfO_2 -passivated surfaces have thicker prongs consisting of overlapping small round bulbs and cracks. These results therefore reveal that while a 20 nm protective film of hafnia is beneficial in inhibiting the large-scale formation of these carbon precipitates, it does not entirely eliminate their formation. Moreover, the appearance of these structures suggests that they are being generated at the Ta- HfO_2 interface, and that they are pushing out against the hafnia, thereby granting them a cracked appearance. Further studies must be conducted for long time frames to understand the effect of hafnia as a thermal barrier coating.

A comparison of Auger concentration depth profile of an unannealed hafnia-passivated surface and of a star-shaped precipitate formed on a passivated tantalum surface is given in Figure B-2. Once again, annealing is found to increase the carbon content of the surface, but this change is less significant than that observed for the unpassivated surface. Additionally, the tantalum and oxygen distributions are altered: the tantalum content increases in the hafnia layer, and decreases in the bulk, while the oxygen content follows the reverse trends. A closer look at the carbon Auger peak in Figure B-2(d) reveals the same characteristic lineshape observed in Figure B-2(b) for the tantalum carbide. Together, these results convincingly show

that while a thin film of HfO_2 has some beneficial effects on the chemical stability of the surface, it is unable to completely inhibit the carbon contamination that produces surface tantalum carbides.

The change in the infrared reflectivity of hafnia-passivated tantalum surfaces with annealing at 900°C is shown in Figure B-3(b). Unlike the previous findings on unpassivated surfaces, these results do not reveal any significant modification in optical properties with annealing time. It therefore appears that the number of precipitates formed and the chemical changes observed are not substantial enough to alter the surface's reflectivity.

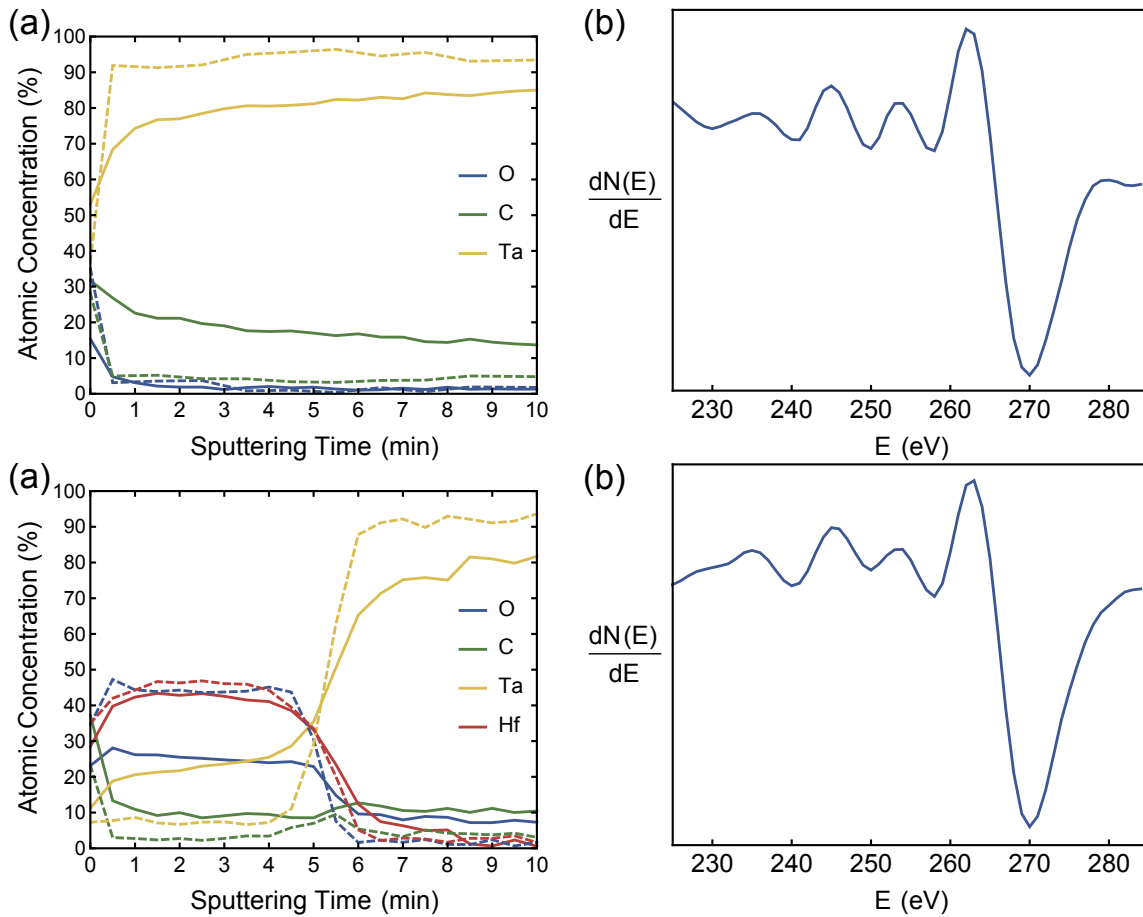


Figure B-2: Auger analysis of tantalum surfaces. Concentration depth profile before annealing (dashed) and of a star-shaped precipitate after a 6 hour anneal at 900°C(solid) for (a) unpassivated tantalum and (c) HfO₂-passivated tantalum. Carbon Auger lineshape of precipitate for (b) unpassivated tantalum and (d) HfO₂-passivated tantalum.

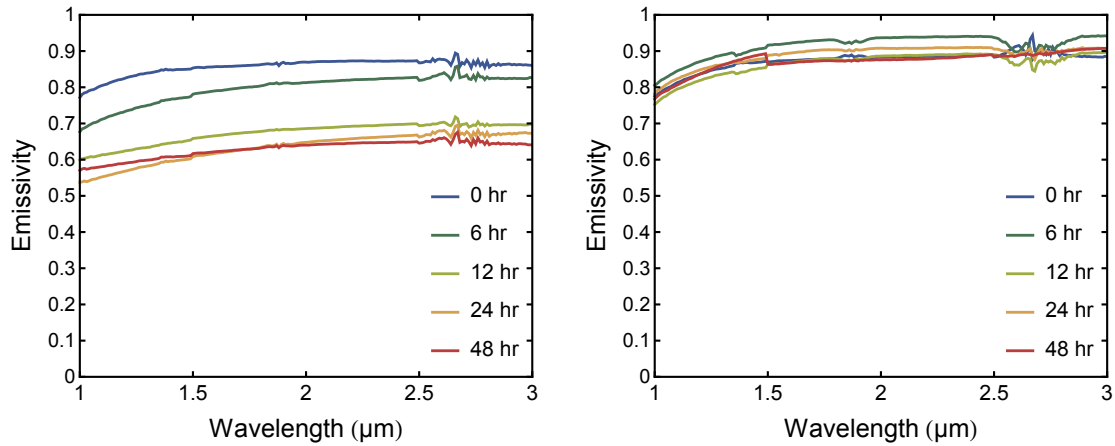


Figure B-3: Infrared reflectivity of a (a) unpassivated tantalum surface and (b) hafnia-passivated tantalum surface as a function of annealing time at 900°C.

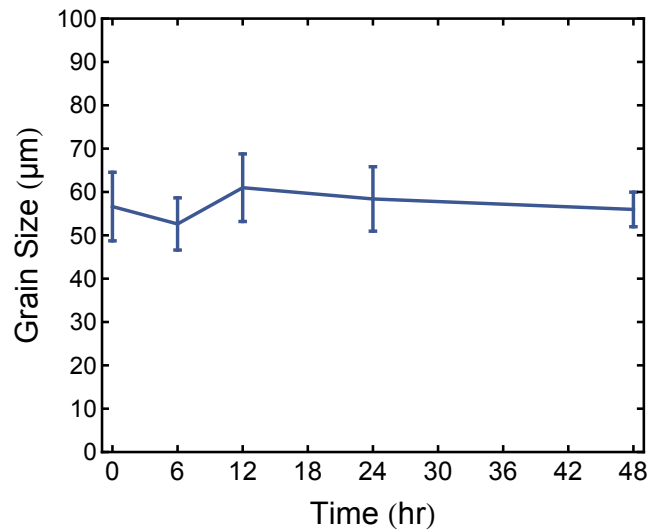


Figure B-4: Unpassivated tantalum grain size as a function of annealing time at 900°C.

Appendix C

Sputtered Metallic Coatings

In this work, we investigated sputtered refractory metal coatings and their suitability at high-temperatures. The key challenges for such coatings are: thermo-mechanical stability regarding delamination, oxide formation and diffusion at high operating temperatures, and achieving long term high-temperature grain stability. In addition, as for the bulk substrates, high reflectance is critical for high-temperature nanophotonic devices. Using a coating as a functional layer on different substrates, selected and matched to the system's needs, decouples the requirements of the functional layer and the substrate. In initial studies, evaporated tantalum coatings on silicon were found to have low film density and high surface roughness, resulting in low reflectance in the near-infrared wavelength range and thick sputtered tungsten coatings on silicon delaminated at high temperatures [67]. In this work, two coatings were investigated:

- The tungsten coatings on silicon study revealed that sputtered tungsten layers were a promising approach for a PhC substrate, if the challenge of delamination at high temperatures could be overcome [41].
- The thick sputtered tantalum coatings on polished Inconel 625 were found to be suitable substrates for high-temperature energy conversion applications as no delamination occurred after anneal up to 900°C for 24 hours [40].

C.1 Tungsten on Silicon Substrates

The tungsten coatings (1 and 5 μm thick) were fabricated via DC magnetron sputtering on silicon (100) substrates [129]. Argon was used as a sputtering gas at 10 mTorr, with a base pressure of $\sim 8 \times 10^{-7}$ Torr. The chamber contained a heat source that was used to bring the internal chamber and substrates to a temperature of 400°C. The deposition was carried out at this elevated temperature, which allowed the mobility of the arriving atoms to achieve a dense structured film. Before the deposition, an RF back-sputter was carried out to prepare the substrate for optimal adhesion. The adhesion layer, 100 Å of titanium, was deposited at 10 mTorr with no gas modulation. The tungsten deposition was then activated still under elevated temperature (400°C). During the tungsten metallization, the starting pressure of argon at 10 mTorr was modulated between 10 and 30 mTorr in increments of 10 min at 10 mTorr and 15 min at 30 mTorr until the desired thickness was achieved. The argon gas modulation assists in alleviating film stress by obtaining a near neutral stress state of the deposited film. A slight compressive stress to the film is an acceptable condition for adhesion to the substrate [130, 131]. The chamber was slowly allowed to cool to ambient temperature before opening.

The prepared samples were imaged by AFM (Veeco Nanoscope V Dimension 3100), to characterize the surface and roughness of the samples. An SEM (Zeiss) was used to obtain images of the cross-section of the sample, and to confirm the film thickness. The reflectance of the tungsten samples was obtained experimentally at room temperature and before and after each annealing run using an automated spectroradiometric measurement system, scanning the wavelength from 1 to 3 μm . The effects of temperature on the samples were studied using two different furnaces. X-ray diffraction (XRD) analysis was performed in the PANalytical X'Pert Pro Multipurpose Diffractometer with an Anton-Paar HTK1200N Furnace *in situ*, in vacuum (50 mTorr), flowing argon (100 mTorr) over a 48 hour period while heating at a rate of 5°C/minute to avoid thermal shock. Using this method, the broadening of

the tungsten peaks and the microstrain evolution were quantified as a function of temperature, from room temperature to 1000°C. In order to characterize the optical properties in dependence of each annealing temperature, another set of samples was annealed in a tube furnace in vacuum (10 mTorr base pressure), flowing argon gas (60 mTorr), at a slow heating and cooling rate of 2°C/minute. The samples were annealed at 500, 700, 800, and 900°C for 1 hour and reflectance was measured after each annealing run.

The coatings were characterized as deposited by AFM and SEM imaging (as shown in Figure C-1). The surface roughness of the two samples was characterized and compared using the AFM. The arithmetic average (R_a) of the roughness was found to be 4.56 nm and 18.6 nm for a coating thickness of 1 and 5 μm respectively, with a maximum amplitude range (Z) of 50.7 nm and 206 nm, respectively. A strong preferential columnar growth was observed in the SEM images of the cross-section of both coatings (Figure C-1), which was observed in literature for tungsten coatings grown under tensile stress [132].

The optical properties of the coatings as deposited and after annealing at different temperatures were characterized. The measured spectral reflectance of the unannealed sputtered samples as deposited was not as high as that of bulk tungsten in the IR range and was found to be 0.80 and 0.75 at a wavelength of 2 μm for the 1 and 5 μm sample respectively, in comparison to 0.9 for bulk tungsten [121]. In order to measure reflectance as a function of annealing temperature, one set of samples was annealed at different temperatures for 1 hour each. The 1 μm sample exhibited higher reflectance than the 5 μm sample for all wavelengths before annealing but its reflectance did not change significantly with annealing up to 700°C at which point it delaminated. The 5 μm sample annealed at 900°C however showed a significant increase in reflectance, and after a 1 hour anneal at 900°C, the 5 μm sample's reflectance was comparable to the values found in literature for polished flat tungsten (Figure C-2).

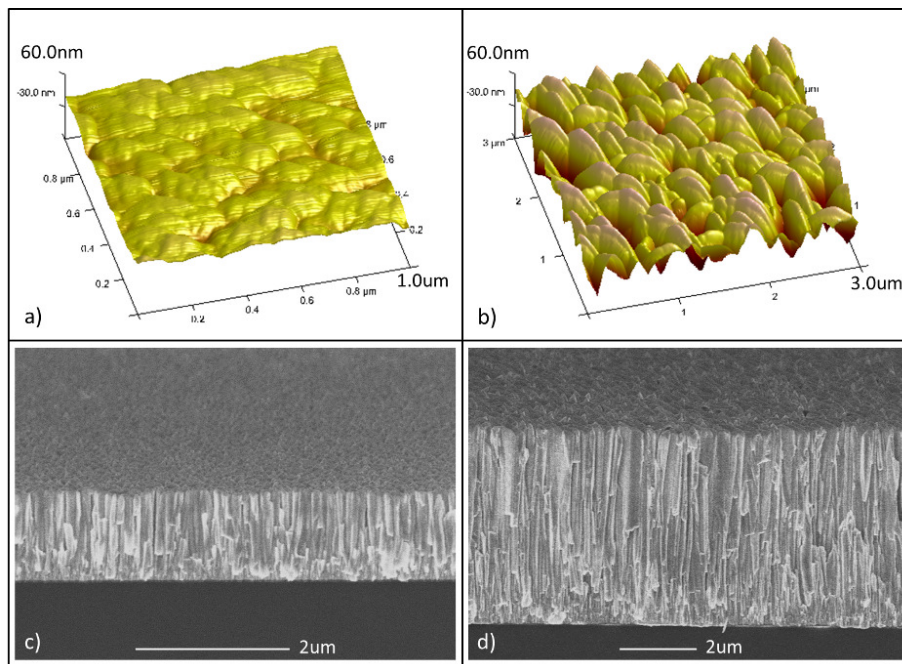


Figure C-1: (a) and (c) AFM and SEM imaging, respectively, of the 1 μm tungsten sputtered film. (b) and (d) AFM and SEM imaging, respectively, of the 5 μm tungsten sputtered film, showing increased roughness of the 5 μm thick layer as compared to the 1 μm thick one. Preferential growth is observed in both samples.

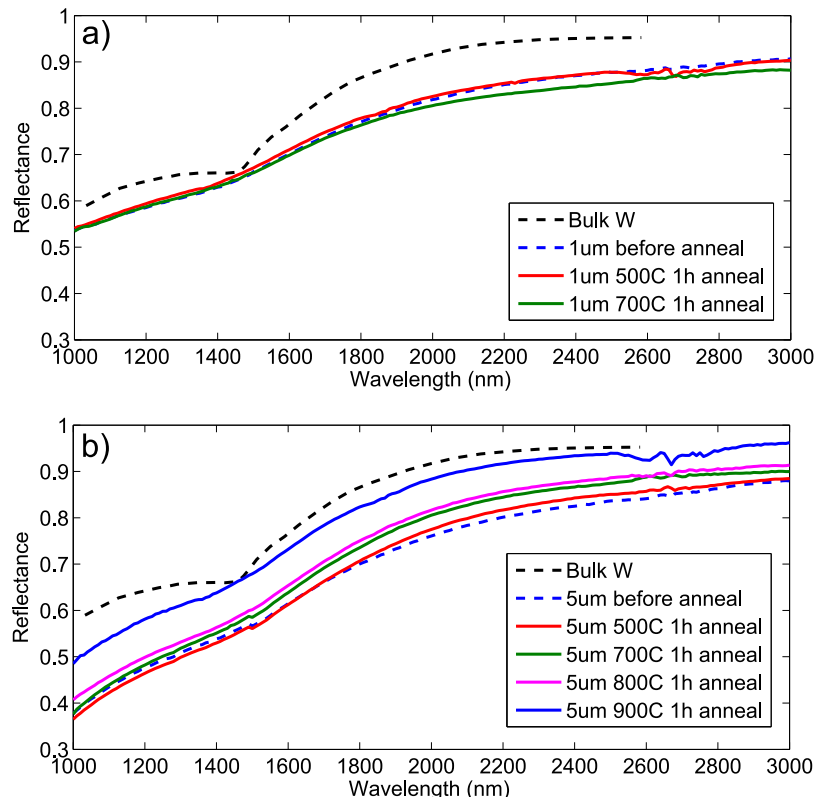


Figure C-2: Comparison of reflectance of bulk tungsten [121] to the experimentally measured reflectance of (a) the 1 μm sputtered tungsten coating and (b) the 5 μm sputtered tungsten coating before and after the 1 hour anneal in a tube furnace at different temperatures at a ramp rate of $2^\circ\text{C}/\text{min}$.

The increase in reflectance can be attributed to coating densification, decreased porosity of the layer and grain growth [133]. According to effective medium theory [134], the effective refractive index of a heterogeneous medium depends on the volume fraction of the two constituents, and is limited by the Wiener bounds. As the fraction of air respective voids and grain boundaries to metal decreases with annealing in the deposited layers, the effective refractive index increases, leading to higher reflectance. Hence, annealing of the tungsten coatings at temperatures at or above 900°C is essential in order to obtain the reflectance required for photonic applications at high-temperature, for the tungsten sputtering parameters used in this study.

The surface roughness and coating structure of the thicker coating before and after annealing at 900°C is compared by AFM surface scans and SEM images of the film cross-sections, respectively, in Figure C-3. It was observed that the reflectance of the sample increased after annealing even though the surface roughness also increased from approximately 19 nm to 35 nm. No visible change in the structure of the tungsten coating and no volume change can be discerned in the cross-section images. The densification of a deposited film during annealing that can be observed in an increase in reflectivity in our study, and more generally in a change of the optical and electrical properties of deposited metal films, does not necessarily lead to a reduction of volume. It is rather a consequence of a reduction of porosity along grain boundaries and a reduction of defect sites, that would be reordered at higher temperature and thus release some of the disorder and microstrain accumulated during deposition [38,133].

The approximate crystallite size and microstrain (non-uniform lattice strain) of the samples was determined by evaluating the broadening of the diffraction peaks in the XRD pattern. Generally, in a powder sample, a large number of diffraction peaks is obtained. In the case of our coatings, only two tungsten peaks were observed: the (110) peak and the (220) peak, as shown in Figure C-4, which is attributed to the highly textured nature of the sputtered samples due to a strong preferential growth. The microstrain in the samples was quantified using the Williamson-Hall plot [135].

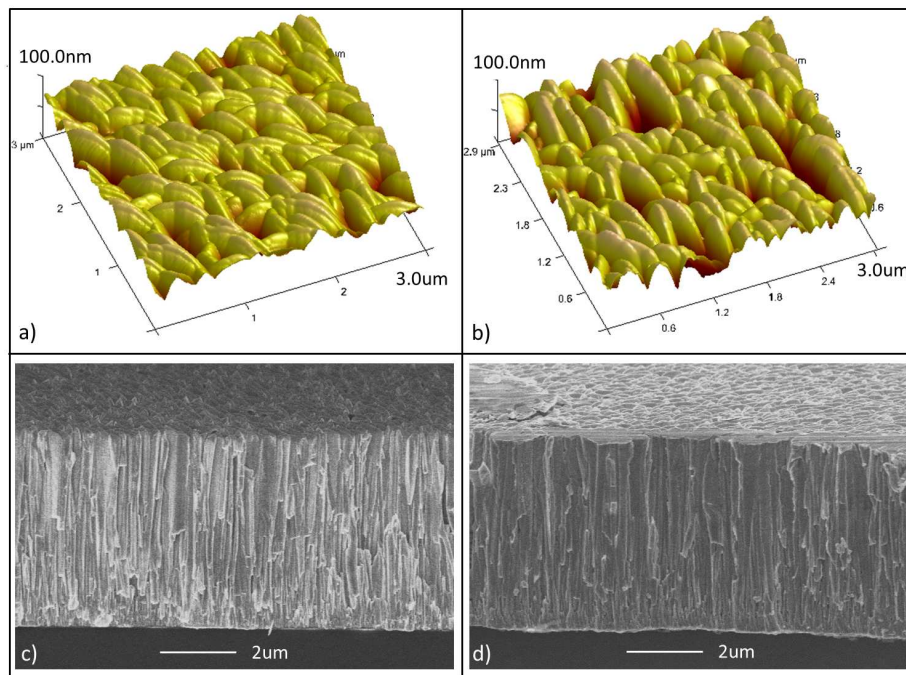


Figure C-3: (a) and (c) AFM and SEM imaging, respectively, of the 5 μm tungsten sputtered film before anneal (room temperature). (b) and (d) AFM and SEM imaging, respectively, of the 5 μm tungsten sputtered film after anneal at 900°C for 1 hour. No noticeable difference in thickness was observed after anneal despite an increase in roughness.

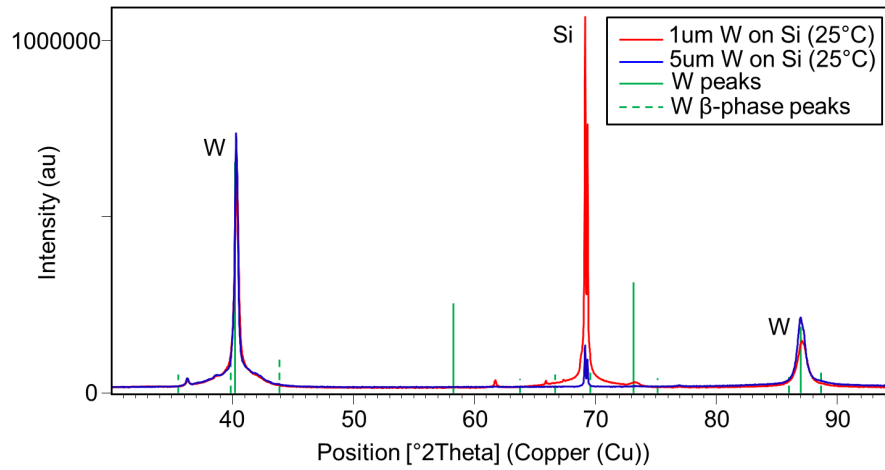


Figure C-4: XRD data collected using a diffracted beam monochromator. The 1 and 5 μm tungsten films deposited on a silicon (100) substrate are compared at 25°C. The predominant peak of the silicon occurring at 69.3° corresponds to the (100) peak. The predominant peak of the tungsten occurring at 40.2° corresponds to the (110) peak, and the other significant tungsten peak occurring at 86.9° corresponds to the higher order peak (220). The presence of only one first order peak indicates the highly textured nature of the tungsten sample. The small peak at 36.2 2θ can be readily identified as copper K- β peak due to the XRD source, not the tungsten coating.

Since the broadening of the peaks was dominated by microstrain the crystallite size was not easily resolved. It was found to be between 50 and 100 nm for the 5 μm sample and 20 to 80 nm for the 1 μm sample at room temperature, before anneal. The lack of precision was due to the presence of only one first-order peak resulting in microstrain dominance. A crystallite size of 10-50 nm range has previously been observed in tungsten sputtered thin-films deposited at room temperatures [136] which is in the same range as our findings.

Both the 1 and 5 μm thick tungsten coatings were sputtered by stress balancing them by modulating an argon gas pressure between 10 mTorr and 30 mTorr. Quite possibly the 10 mTorr layer and the 30 mTorr layer have different grain structure and physical density; however, each layer was not independently investigated. Instead the composite coating was characterized. It is essential to balance the stress in such thick

coatings in order to avoid delamination. The influence of the deposition conditions on the properties of DC magnetron sputtered thin tungsten films is well studied [132]. Depending on argon gas pressure, substrate material, substrate temperature and deposition duration, there is a different relative amount of beta- and alpha-tungsten phase deposit. According to literature, the beta phase is metastable and transforms into alpha phase. It is a thermally driven process but the transformation takes place even at room temperature. For thicker films (> 50 nm), even deposited at room temperature, no beta phase is found [137,138]. This is confirmed in Figure C-4 as no tungsten beta phase peaks were found in the XRD analysis of the thick tungsten coatings.

In order to quantify the evolution of the microstrain as a function of temperature, an *in-situ* XRD analysis was performed on the 1 and 5 μm samples over a 48 hour period from 25 to 1000°C in 100°C increments. For each temperature, the diffraction peak width at full width half-maximum (FWHM) and microstrain were quantified (Figure C-5). A clear inflection point was seen around 700°C for both the 1 and 5 μm samples. Assuming that the majority of the peak broadening was due to microstrain, as in the room temperature measurements, the results indicated that the micro-structure was unambiguously changing. The microstrain was quantified, ranging from 0.33 to 0.18% for the 1 μm sample and 0.26 to 0.20% for the 5 μm sample, decreasing as the temperature increased. This observation is reasonable since at higher temperatures molecular mobility increases and thus lattice strain is relieved. It was observed that the 5 μm sample had less microstrain than the 1 μm sample at all temperatures.

The tensile stress in the films is attributed to the CTE mismatch of substrate and film and the elevated substrate temperature during deposition. The films were deposited at an elevated temperature of 400°C and the deposition parameters were chosen such that the films were mostly balanced at the deposition temperature. As the substrates cool down after deposition, however, the smaller CTE of the substrate

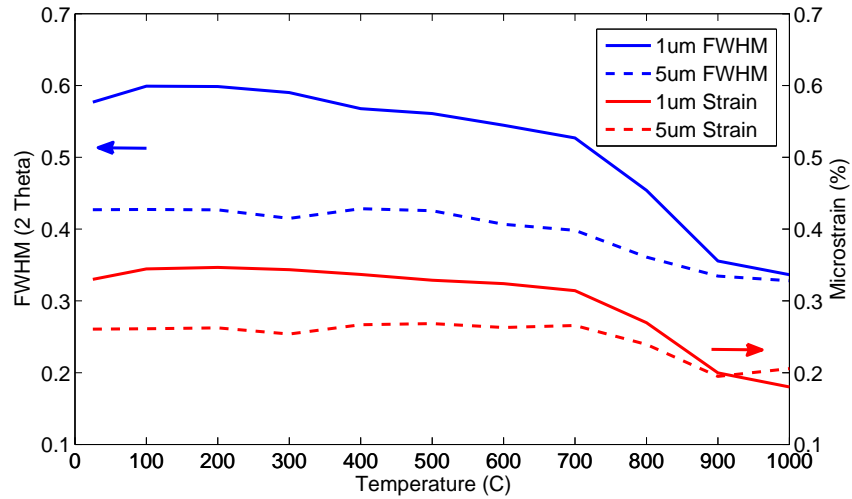


Figure C-5: Left axis: FWHM of the 1 and 5 μm tungsten sample as a function of temperature (blue). Right axis: microstrain of the 1 and 5 μm tungsten sample as a function of temperature (red). While the exact crystallite size could not be determined, the crystallite size of the 5 μm sample was clearly larger resulting in a smaller FWHM of the diffraction peak.

leads to an increasingly tensile stress in the coatings. Therefore, as the samples are annealed, the tensile stress is released again, which can be seen in the reduction of the tensile micro-strain with increasing temperature.

Despite the decrease in microstrain (*i.e.* decrease in the number of dislocations and defects in the film) with increasing temperature, delamination occurred between 700 and 800°C for the 1 μm sample and between 900 and 1000°C for the 5 μm sample after annealing in the tube furnace. The delamination can be attributed to the mismatch in CTE of silicon and tungsten. The linear CTE of silicon is about $2.6 \times 10^{-6}/^\circ\text{C}$ while the CTE of tungsten is about $4.6 \times 10^{-6}/^\circ\text{C}$ [139]. Differences in the CTE values of adjacent materials during heating and cooling will induce tensile stress in tungsten, leading to cracks in tungsten since it is a brittle material and cannot withstand tensile stresses. In the case of a brittle material like tungsten, the CTEs should be matched within about $0.2 \times 10^{-6}/^\circ\text{C}$ and a mismatch of 0.5 to $1.0 \times 10^{-6}/^\circ\text{C}$ is considered the upper limit [140, 141]. In addition, the CTE of Ti is about twice as high as that of

tungsten, and could therefore play an additional role in the delamination. However, since the 100 Å layer of Ti used as an adhesion layer represents only 1% of the total thickness of the 1 µm film and only 0.2% of the thickness of the 5 µm film, the thermal mismatch of the CTE of Ti was considered to be a minor effect in the annealing behavior. While the 5 µm sample did not delaminate when annealed at 900°C, it did begin to show signs of microscopic cracking.

C.1.1 Summary

The properties of tungsten coatings, in particular the optical properties, microstrain and surface roughness, and their evolution at high temperatures, were studied as a potential fabrication route for high-temperature nano-structured surfaces. The 5 µm thick layer was found to be rougher than the 1 µm thick layer which resulted in a lower reflectance at all wavelengths. However, after annealing the 5 µm sample at 900°C for 1 hour, its reflectance exceeded that of the 1 µm sample and came very close to that of bulk tungsten found in literature. An XRD analysis was conducted to understand the effect of temperature on the crystallite size and microstrain of the 1 and 5 µm samples. The grain growth could not be definitively quantified due to the dominating presence of microstrain in both samples but was in the order of 20 to 80 nm for the 1 µm sample, and 50 to 100 nm for the 5µm sample, as deposited, and increased with temperature. Microstrain was quantified, ranging from 0.33 to 0.18% for the 1 µm sample and 0.26 to 0.20% for the 5 µm sample, decreasing as the annealing temperature increased especially for temperature larger than 700°C. It was observed that the 5 µm sample had less strain and larger crystallite size than the 1 µm sample at all temperatures. The delamination of the tungsten at high annealing temperature was attributed to the mismatch in CTE of silicon and tungsten.

C.2 Tantalum on Inconel Substrates

Tantalum coatings were fabricated via ion-assisted DC magnetron sputtering on Inconel 625 substrates at a deposition temperature of 300°C at 2 kW. Argon was used as the sputtering gas and the vacuum chamber pressure was 2 mTorr with a base pressure of 5×10^{-6} Torr. A 40 V bias was applied on the samples and the discharge filament was run at 40 A for the secondary plasma to increase ion bombardment. The thicknesses of the samples were determined by contact profilometry after deposition and found to be 8 and 30 μm via witness coupons. A 20 nm conformal layer of hafnium oxide (HfO_2) was deposited via ALD at 250°C, using TDMAH and water as precursors as described in Chapter 3, to prevent degradation of the coatings at high temperatures [38].

In order to characterize the optical properties as a function of temperature, the samples were annealed at 700, 900, and 1100°C for one hour in a quartz-lined Inconel tube furnace in vacuum (5×10^{-6} Torr base pressure), at a slow heating and cooling rate of 2°C/minute. The reflectance of the tantalum samples was measured at room temperature and after each annealing run using an automated spectroradiometric measurement system (Gooch & Housego OL750), scanning the wavelength from 1 to 3 μm .

The prepared samples were imaged by AFM (Veeco Nanoscope V Dimension 3100), to characterize the surface and roughness of the coatings as-deposited and after each anneal. In order to quantify and compare the roughness of the coating, the average one-dimensional surface roughness R_a and root-mean-square (RMS) roughness R_q were calculated from the AFM images. In addition, the autocorrelation $R(r)$, which measures the correlation of surface heights separated laterally by the distance r , and height-to-height correlation $H(r)$ functions were calculated. The autocorrelation was fitted using the $R(r) = \exp(-(r/\xi)^{2\alpha})$ approximation model where ξ is the lateral correlation length, defined as the value of r at which $R(r)$ decreases to $1/e$ of its original value, and α is the roughness exponent, extracted from the slope of the

Table C.1: X-ray elastic constants of tantalum

hkl	S_2 (10^{-6} MPa $^{-1}$)
220	7.022
310	7.852
222	6.591
321	7.022

corresponding height-to-height correlation function analysis [142].

The residual stress of the coatings was determined via XRD analysis (Rigaku Smartlab) using a $\sin^2 \psi$ methodology [143, 144], as-deposited and after each anneal. After measuring the d -spacing at several sample rotations ψ , the residual stress σ was calculated (under the assumption of a bi-axial stress state in the film) as

$$\sigma = \frac{1}{d_0} \frac{1}{S_2} \frac{\partial d}{\partial \sin^2 \psi} \quad (\text{C.1})$$

in which d_0 is the stress-free lattice parameter (taken as the lattice parameter at $\psi = 0$), and the partial derivative $\frac{\partial d}{\partial \sin^2 \psi}$ is calculated from a fit of the results. The X-ray elastic constant of tantalum is denoted by $S_2 = (1 + \nu)/E$ which depends on the crystallographic plane of interest, and is equivalent to $(1 + \nu)/E$, where ν is Poisson's ratio and E is the elastic modulus. In this work, four tantalum diffraction peaks were analyzed ([220], [310], [222], and [321]), and their respective residual stresses were averaged. The values of S_2 for each peak, calculated from single crystal elastic constants [145–149] as the Neerfeld limit (i.e., the average of the Voigt and Reuss limits), are listed in Table C.1.

The phase and texture of the sputtered tantalum coatings were characterized via XRD analysis and compared after different anneal temperatures. The texture of the films was evaluated using pole figure analysis and compared after different anneal temperatures.

In this study, the topographical results, including the roughness R_q , the lateral correlation length ξ , and the roughness exponent α , of the 8 and 30 μm coatings

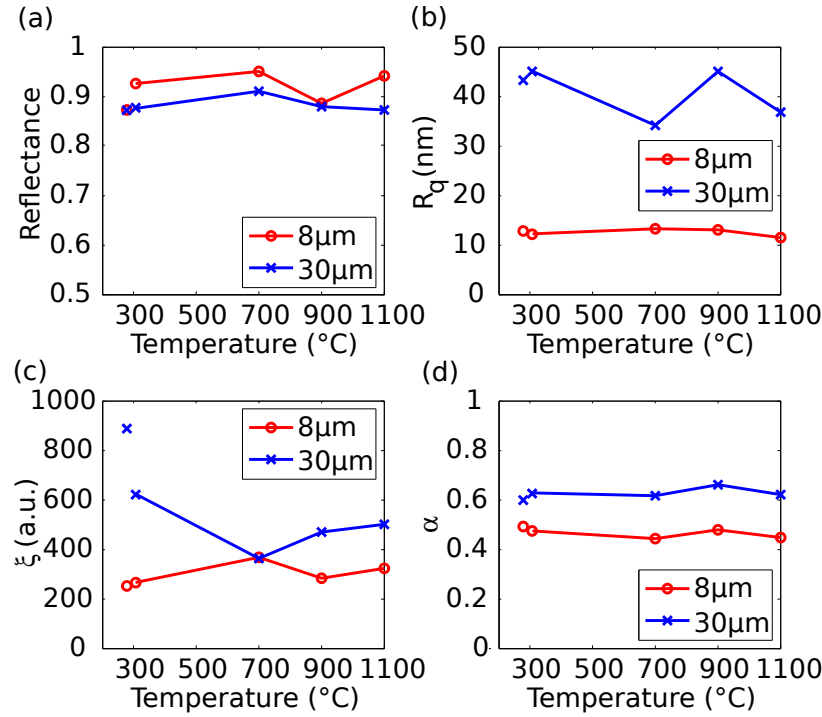


Figure C-6: Comparison of the 8 μm (in red) and 30 μm (in blue) coatings in terms of (a) reflectance of the coatings measured at a wavelength of 2 μm , (b) RMS roughness R_q , (c) lateral correlation length ξ , and (d) roughness exponent α , as-deposited, as well as after the deposition of the protective HfO_2 conformal layer at 250°C, and after anneal at 700, 900, and 1100°C.

were characterized, as shown in Figure C-6. In all cases, no significant change was observed, thereby revealing that neither the height variation, nor the arrangement of this variation, was affected by annealing.

The optical properties of the coatings as-deposited and after annealing in vacuum at different elevated temperatures were characterized. As shown in Figure C-7, the reflectance of the tantalum sputtered coatings was exceptionally high and comparable to that of polished bulk samples. Dense metallic coatings have been shown to have similar optical properties as their bulk counter parts [150–154]. On average, the reflectance of the 8 μm coating was higher in the measured range than that of the 30 μm coating. Surface roughness causes a decrease in reflectance and can introduce a wavelength dependence through surface plasmon effects [155]. The initial increase

in reflectance after annealing can be attributed to coating densification, decreased porosity of the layer, and grain growth [133]. The subsequent decrease can be attributed to the observed increase in surface roughness. Overall, a minimal net change in reflectance was observed, thus meeting the roughness and reflectance requirements for thermal emitter fabrication.

The phase and texture of the sputtered tantalum coatings were characterized via XRD analysis. Previous studies have shown that elevated deposition temperatures promote the formation of BCC α -tantalum coatings, whereas lower deposition temperatures lead to β -tantalum [150, 151, 156]. Additionally, it has been shown that α -tantalum is the predominant phase in thick sputtered tantalum coatings, with increasing β -tantalum content with decreasing thickness [154, 157, 158]. As the thickness of the coatings studied here is in the micron range and the deposition was carried out at a substrate temperature of 300°C, the existence of the beta phase is unlikely. This is confirmed in Figure C-8, which shows an excellent agreement between the experimental XRD peaks and the reference α -tantalum peaks.

From pole figure analysis, a fiber texture was observed in both films, as revealed in Figure C-9 by the lack of x and y preference. For the 8 μm coating, the surface was aligned with the (110) crystallographic planes, as demonstrated by the surface normals in the center of the (220) pole figure. This is a common growth direction for BCC films due to its high density, and has been observed in many other studies of sputtered tantalum films [150, 151, 156–159]. Interestingly, the thicker coating exhibited a (111) fiber texture. This transition in texture with thickness has been previously detected [157], and has been attributed to stress build-up in the growing film which favors a texture that reduces the stress. The pole figures were obtained both before annealing and after one-hour anneals at 700 and 900°C, and no change in texture was observed.

The calculated residual stress, as defined in Eq. C.1 is plotted as a function of the annealing temperature and coating thickness in Figure C-10. These results indicate

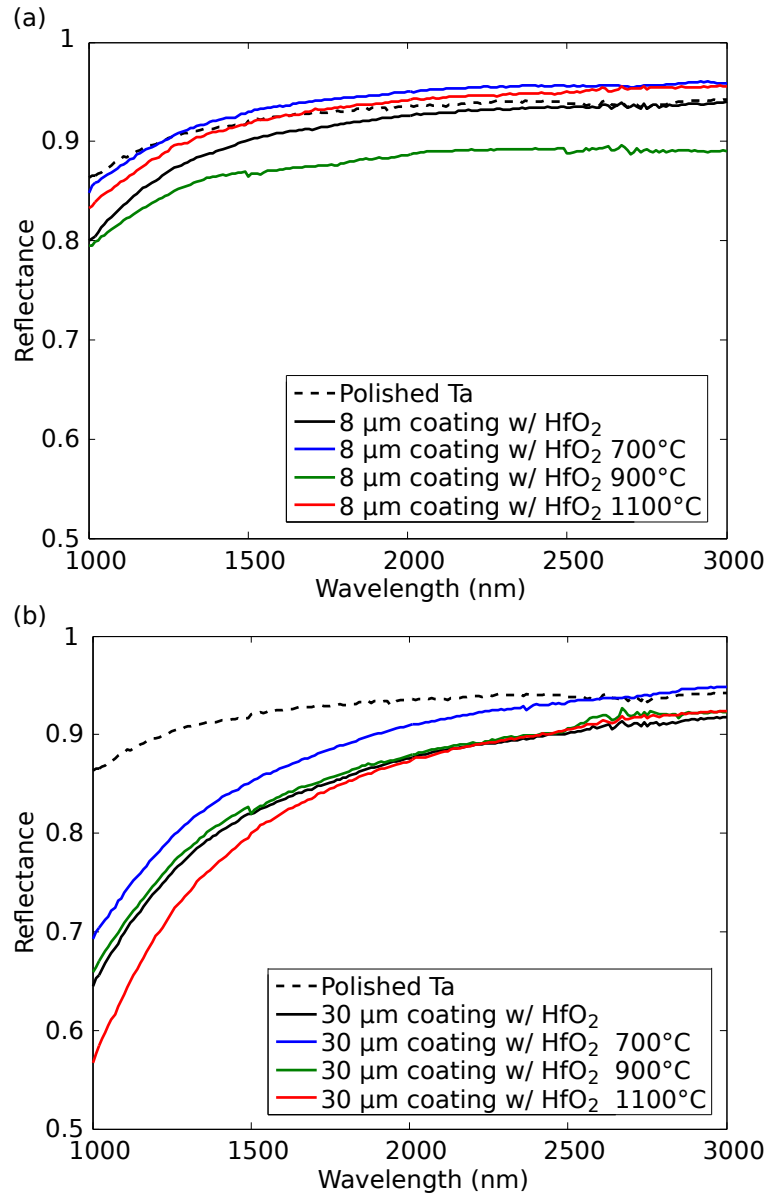


Figure C-7: Reflectance of the 8 μm (a) and 30 μm (b) tantalum coating with the protective HfO₂ conformal layer after one-hour anneals at 700, 900, and 1100°C compared with flat polished tantalum. All reflectance measurements were made at room temperature.

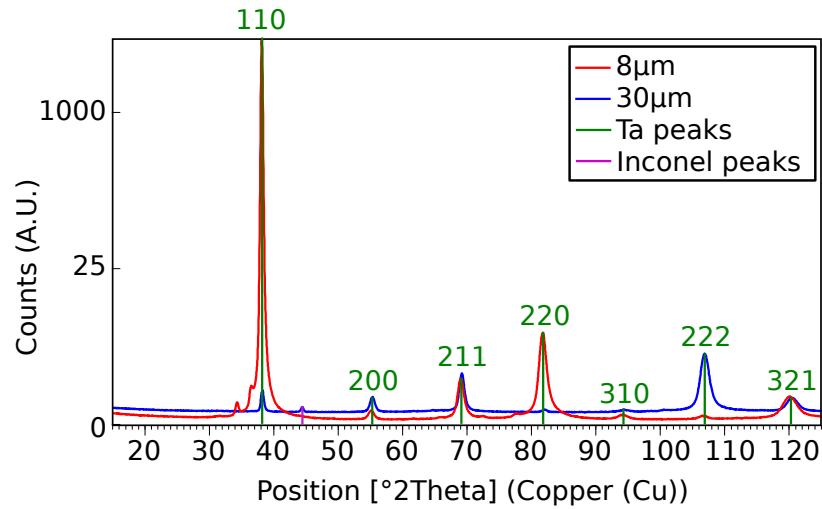


Figure C-8: XRD diffraction peaks all originating from α -phase; no β -phase is present. (The small peak to the left of the (110) peak is the Cu β -peak from the instrument).

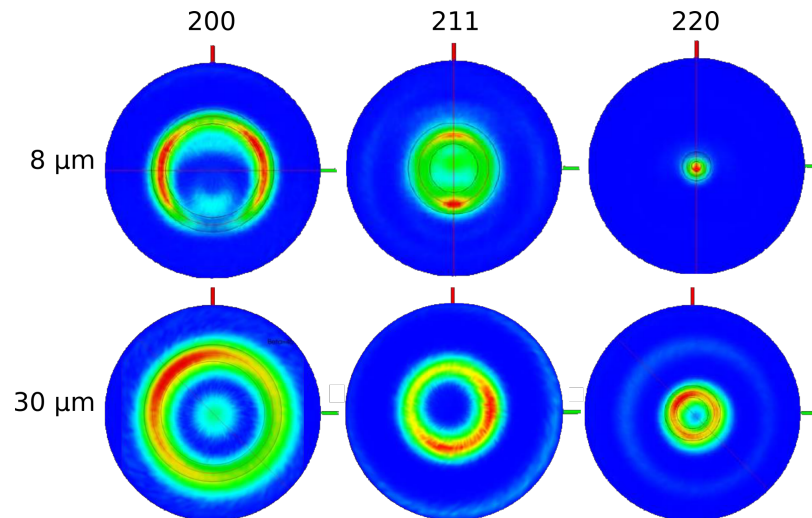


Figure C-9: In both films, a strong (110) fiber texture was observed. The (220) surface normals can be seen in the center of the pole figure. The other projections (211) and (200) show circles, signifying that there is no x and y preference.

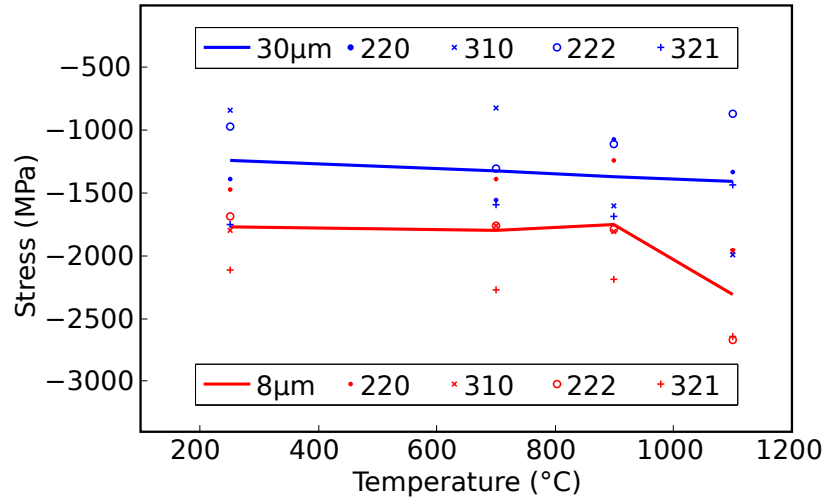


Figure C-10: Residual stress of the 8 and 30 μm coatings calculated as-deposited and after anneal at 700, 900, and 1100°C. The line represents the average of the four diffraction peaks considered at each temperature.

that the as-deposited coatings were highly stressed (values ranging from 1250 to 1750 MPa) and in compression. Values of this magnitude are common for thin films and coatings and have been observed previously in sputtered tantalum samples [153, 157–166].

The stress caused by differences in thermal expansion (thermal stress) was calculated, using the thermal expansion data in [167] (assuming that the thickness of the coating is negligible in comparison to that of the substrate) and taking the deposition temperature to be 673 K, and found to be about -800 MPa. The stress caused by the deposition (intrinsic stress) was found to be approximately -450 to -950 MPa. Compressive intrinsic stresses are expected in films sputtered with low sputtering pressures, high substrate biases, normal incidence, high target mass, low sputtering gas mass, and a low substrate temperature, as these will produce large particle momenta while maintaining low atomic mobility [168, 169]. As such, tantalum coatings deposited with an argon gas (high target to gas mass ratio), at 300°C (low homologous temperature of $0.2T_M$) are expected to be in compression. The

occurrence of this intrinsic compressive stress may be beneficial, as it is indicative of dense coatings with optical properties that approach those of bulk materials (i.e., high reflectivity) [153, 154, 160, 161, 164, 168, 169]. On the other hand, it is also worth noting that high compressive stresses can lead to coating buckling and poor adhesion.

The change in residual stress after annealing is shown in Figure C-10. For the 30 μm coating, a slight increase in compressive stress with temperature was observed, but all results were well within error of one another. For the 8 μm coating, the residual stress was found to be relatively stable. The only exception was the 1100°C anneal, which caused a sudden increase in compressive stress. However, due to the large scatter in the results from all four diffraction peaks, this increase was not statistically significant. This thermally stable residual stress is in contrast to the previous studies on tantalum coatings in which an increase in the compressive stress, increase in the tensile stress, or a reversal from compressive to tensile stress was observed with annealing [162, 163, 165].

The changes in residual stresses with annealing can be attributed to a number of processes: plastic deformation, phase transformation, grain growth, and impurities or oxidation. Indeed, at high temperatures, the thermal stress may cause the coating to yield, thereby altering the residual stress. However, as the substrate's thermal expansion coefficient is larger than that of the coating, the thermal stresses will tend to decrease the compressive stress, and ultimately produce a net tensile stress on the order of 1500 MPa at 1373 K. This signifies that plastic deformation may be unlikely at the temperatures investigated and with this combination of substrate and coating. Previous work (on β to α transformations [162, 165]) has shown that phase transitions can result in a relaxation of the residual stress. However, as the coatings studied are already in the stable α phase, transformations will not occur. Additionally, at elevated temperatures, the reduction of the grain boundary area of the coating would reduce its excess volume and produce a net tensile stress [168, 169]. However, tantalum is unlikely to experience significant grain growth at the

temperatures of interest [124, 125, 127, 128, 170, 171], and this effect may be negligible. Finally, an increase in the impurity content of the coatings, as well as the formation of tantalum pentoxide (Ta_2O_5), has been associated with an increase in the compressive stress [163, 164, 166, 172, 173], which is caused by an associated increase in the volume of the unit cells. However, the protective HfO_2 coating, as well as the high-vacuum conditions, may prevent any significant oxidation, and would therefore prevent volumetric distortion.

C.2.1 Summary

In this study, we found that the sputtered tantalum layers withstand temperatures up to 1100°C without delamination and can be used as a viable photonic crystal substrate. The reflectance of the tantalum sputtered coatings was found to be exceptionally high as-deposited and comparable to that of polished bulk samples. The reflectance of the $8\ \mu\text{m}$ coating was found to be higher than that of the $30\ \mu\text{m}$ coating due to lower surface roughness. The reflectance of the coatings did not increase significantly after one-hour anneals at 700 to 1100°C in vacuum. No significant change in roughness was observed, as expected from the reflectance measurements, thus meeting the roughness and reflectance requirements for thermal emitters. The pole figures, obtained by XRD diffraction before and after the anneals, revealed a fiber texture for all peaks for both coatings at all temperatures. The $8\ \mu\text{m}$ coating exhibited a (110) texture while the $30\ \mu\text{m}$ coating exhibited a (111) texture, attributed to stress build-up. The tantalum sputtered coatings were found to be in a state of compressive stress, thereby producing dense coatings with high reflectivity. For the $8\ \mu\text{m}$ coating, the residual stress was found to be relatively stable. For the $30\ \mu\text{m}$ coating, a slight increase in compressive stress with temperature was observed, but all results were well within error of one another. Annealing the coatings was not found to produce any significant changes in the residual stress, demonstrating that phenomena such as plastic deformation, phase transformations, grain growth, and oxidation were not

significant under these conditions. Both 8 and 30 μm coatings were found to be suitable substrates for photonic crystal fabrication, however the 8 μm coating exhibited all in all slightly better optical and thermo-mechanical properties. Overall, the results of this study suggest that these thick tantalum coatings are a promising alternative to bulk substrates as a relatively low-cost and easily integrated platform for nano-structured devices for high-temperature energy conversion applications.

C.3 Optical Performance

Spectral efficiency and in-band emissivity are typically used as figures of merit when evaluating selective emitter because spectral efficiency, the fraction of input heat converted to in-band radiation, largely determines the heat-to-electricity conversion efficiency, and in-band emissivity, the total in-band power normalized to the blackbody, determines the required active area to achieve a specified electrical power output and is important in calculating the overall (for example, fuel-to-electricity) conversion efficiency for a lossy system where in-band thermal radiation must compete with other heat loss mechanisms (exhaust, parasitic radiation, etc).

Mathematically, the spectral efficiency η_{sp} , in-band emissivity ε_{in} , and useful emitted power density P_{out} are defined as:

$$\eta_{sp} = \frac{\int_0^{\lambda_{PV}} \varepsilon(\lambda) E_b(\lambda) d\lambda}{\int_0^{\infty} \varepsilon(\lambda) E_b(\lambda) d\lambda} \quad (\text{C.2})$$

$$\varepsilon_{in} = \frac{\int_0^{\lambda_{PV}} \varepsilon(\lambda) E_b(\lambda) d\lambda}{\int_0^{\lambda_{PV}} E_b(\lambda) d\lambda} \quad (\text{C.3})$$

$$P_{out} = \int_0^{\lambda_{PV}} \varepsilon(\lambda) E_b(\lambda) d\lambda \quad (\text{C.4})$$

where $\varepsilon(\lambda)$ is the emitter's hemispherically-averaged wavelength-dependent emissivity, $E_b = 2hc^2/[\lambda^5(e^{hc/\lambda k_B T} - 1)]$ is the spectral blackbody emissive power distribution given by Planck's law, λ is the wavelength, λ_{PV} corresponds to the bandgap of the PV cell (in our case, $\lambda_{PV} = 1.7 \mu\text{m}$ for GaSb), h is Planck's constant, c is the speed of light, k_B is the Boltzmann constant, and T is the emitter temperature.

The calculated spectral efficiency for two optimized photonic crystal designs as a function of operating temperature is shown in Fig. C-11b. At a target operating temperature of 1500K the spectral efficiency of PhC design I (InGaAsSb, $\lambda_{PV}=2.3 \mu\text{m}$) is 57.0% and that of PhC design II (InGaAs, $\lambda_{PV}=2.0 \mu\text{m}$) is 48.2%, increasing with temperature. The optimum operating temperature also depends on the PV cell, as

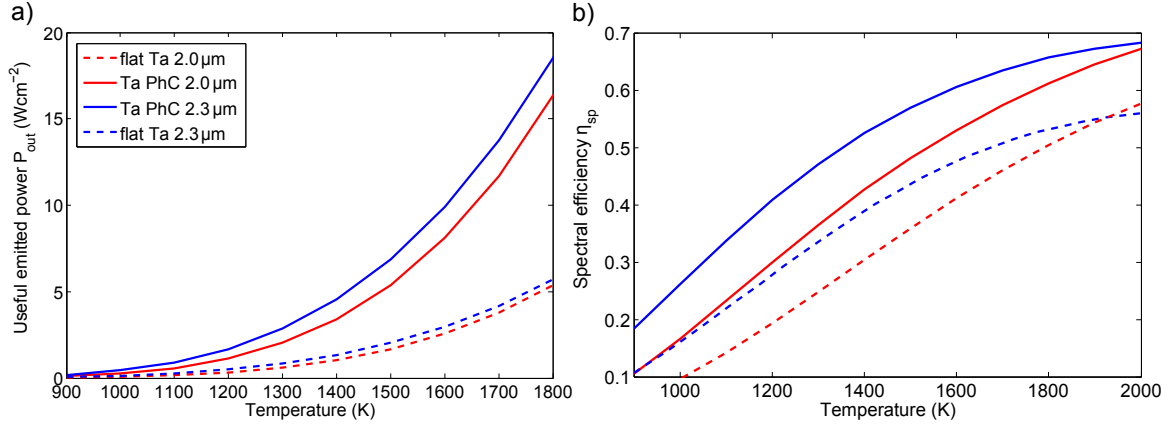


Figure C-11: (a) Useful emitted irradiance (power density P_{out}) and (b) spectral selectivity (η_{sp}) in dependence of the operating temperature for PhC design I (InGaAsSb, $\lambda_{PV}=2.3\mu\text{m}$, blue) and II (InGaAs, $\lambda_{PV}=2.0\mu\text{m}$, red) and for flat tantalum using the same cutoff wavelengths (dashed lines).

Table C.2: Efficiency and power density comparison at 1500K.

Cell	Emitter	η_{sp} (%)	P_{out} (W/cm ²)
InGaAsSb	PhC I	57.0	6.9
InGaAsSb	Flat Ta	43.6	2.0
InGaAs	PhC II	48.2	5.4
InGaAs	Flat Ta	35.9	1.7

the cell efficiency decreases with increasing incident irradiance at higher temperatures. In comparison, the spectral efficiency of flat tantalum at a cutoff wavelength of 2.3 μm is 43.6% and 35.9% at 2.0 μm . In addition to increased selectivity, the useful emitted output power is much higher for the photonic crystal emitter, as shown in Fig. C-11(a). At 1500K, the useful emitted irradiance below the cutoff wavelength is 6.9 W/cm^2 for the photonic crystal emitter with an InGaAsSb PV cell, and 5.4 W/cm^2 with an InGaAs PV cell. In contrast, the useful emitted power using flat tantalum is only 2.0 W/cm^2 and 1.7 W/cm^2 for a cutoff wavelength of 2.3 μm and 2.0 μm respectively. These results are summarized in Table C.2. At this temperature, the spectral selectivity was found to increase by more than 10% using the selective emitter. Since the emissivity of the photonic crystal approaches that of a blackbody for wavelengths $\lambda < \lambda_c$ resulting in higher power density, the useful emitted irradiance was found to be selectively increased *by a factor of 3* using the selective emitter as compared to the non-structured surface [41].

The calculated spectral efficiency and in-band emissivity for the sputtered photonic crystal emitter, flat tantalum, and a blackbody are presented in Fig. C-12. The emissivity used in the calculations was hemispherically averaged over all polar and azimuthal angles to account for angular dependence inherent in the photonic crystal structure. Furthermore, the high temperature material properties were used to simulate the actual performance of a real TPV system. The spectral efficiency increases with temperature because the blackbody spectrum shifts to shorter wavelengths, thus increasing the in-band fraction. Temperature alone cannot be used to achieve high spectral efficiency because of material stability limitations and because increased heat loss elsewhere in the system counteracts gains in spectral efficiency. On the other hand, the in-band emissivity remains nearly constant with temperature because the material properties do not change much with temperature.

The spectral efficiency and in-band emissivity is shown for two emitter temperatures (1200 and 1500°C) in Table C.3. The spectral efficiency of the photonic crystal

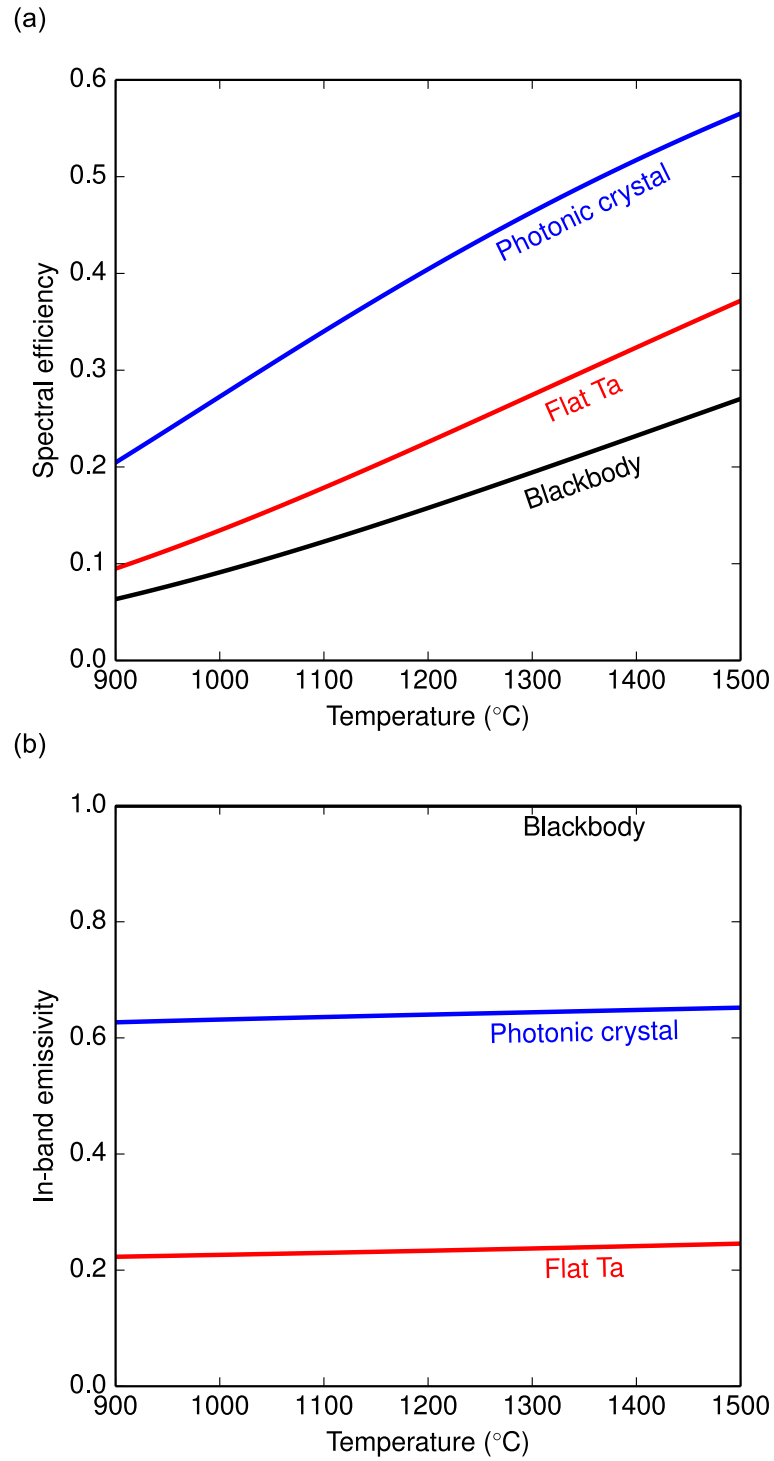


Figure C-12: (a) Calculated spectral efficiency and (b) in-band emissivity of the 2D sputtered tantalum photonic crystal emitter, flat polished tantalum emitter, and blackbody emitter for $\lambda_{PV}=1.7 \mu\text{m}$, as a function of temperature.

Table C.3: Spectral efficiency and in-band emissivity of different emitters.

Emitter type	Spectral efficiency		In-band emissivity	
	1200°C	1500°C	1200°C	1500°C
Sputtered 2D PhC	0.404	0.565	0.640	0.652
Flat Ta	0.226	0.372	0.233	0.246
Blackbody	0.158	0.270	1.000	1.000

is approximately double that of a blackbody because of the reduced out-of-band radiation. The photonic crystal achieves an in-band emissivity about 65% of the blackbody limit. The in-band emissivity can be further increased towards the blackbody limit by optimizing the geometry to maximize hemispherical emission [68].

Appendix D

Custom Codes

D.1 Reflectance Calibration

Because this work demands high accuracy reflectance measurements, we needed to develop an improved calibration procedure. Instead of the built-in linear correction with two standards, we used a linear correction with three standards and least squares fitting. This procedure was used on the Cary 5000, but is applicable to any tool. Before measuring the sample, we made three calibration measurements: first, the sample beam was blocked with an opaque material; second, a calibrated low reflectance standard (Ocean Optics STAN-SSL) was measured; third, a calibrated high reflectance standard (Ocean Optics STAN-SSH) was measured. Additional standards can be used to increase accuracy. When using this method, the Cary can be operated in absolute reflectance mode which does not use the built-in calibration procedure.

The calibration method applies a wavelength-dependent linear correction to the the measured values to estimate the true values:

$$r(\lambda)' = a(\lambda)r(\lambda) + b(\lambda) \tag{D.1}$$

where R' is the true or corrected reflectance, R is the measured reflectance, and a and

b are the correction factors, all as a function of wavelength. The correction factors can be found by solving a system of equations:

$$\begin{bmatrix} R_B & 1 \\ R_L & 1 \\ R_H & 1 \\ \vdots & \vdots \end{bmatrix} \begin{bmatrix} a \\ b \end{bmatrix} = \begin{bmatrix} 0 \\ R'_L \\ R'_H \\ \vdots \end{bmatrix} \quad (\text{D.2})$$

where H denotes the high reflectance mirror, L denotes the low reflectance mirror, and B denotes the blocked beam. Additional calibration points may be added by adding additional rows. Alternatively, the original two-point method can be reproduced by using only the blocked beam and high reflectance rows. The a and b coefficients as well as the least squares residuals for three different measurements are shown in Figure D-1.

D.2 Geometric Parameter Fitting

Accurate values of a , r , and d cannot be obtained directly by SEM, thus we rely on matching the measured reflectance to a simulation. We used a combination of numerical optimization and S4 simulations to match the spectra. Dimensions from SEM images were used as the initial guess. An S4 simulation was run. The difference between the measured spectrum and simulated spectrum was then used as the figure of merit in a nonlinear numerical optimization algorithm. Several examples are shown in Figures D-2, D-3, and D-4.

D.3 Hot Side Model

The purpose of the model is to understand the influence of the emitter on the flow of energy within a TPV device. The full process begins with combustion and ends

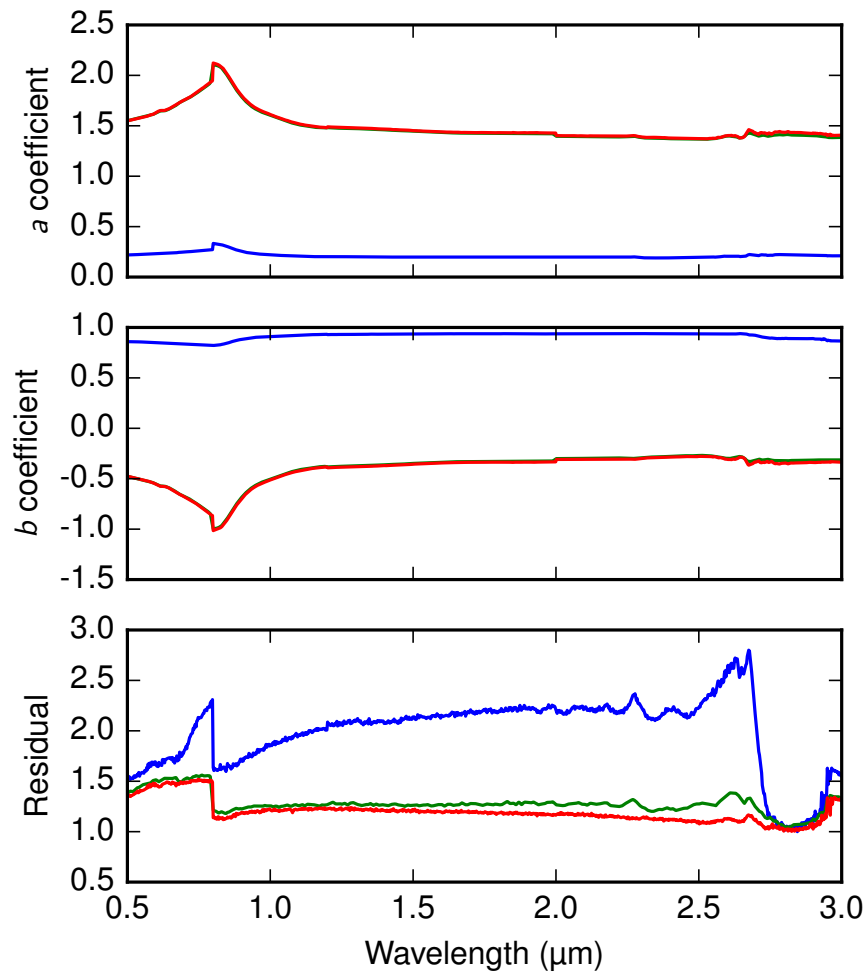


Figure D-1: The a and b coefficients from three Cary runs and the residuals from the least squares fit. Note that the red and green lines are overlapping.

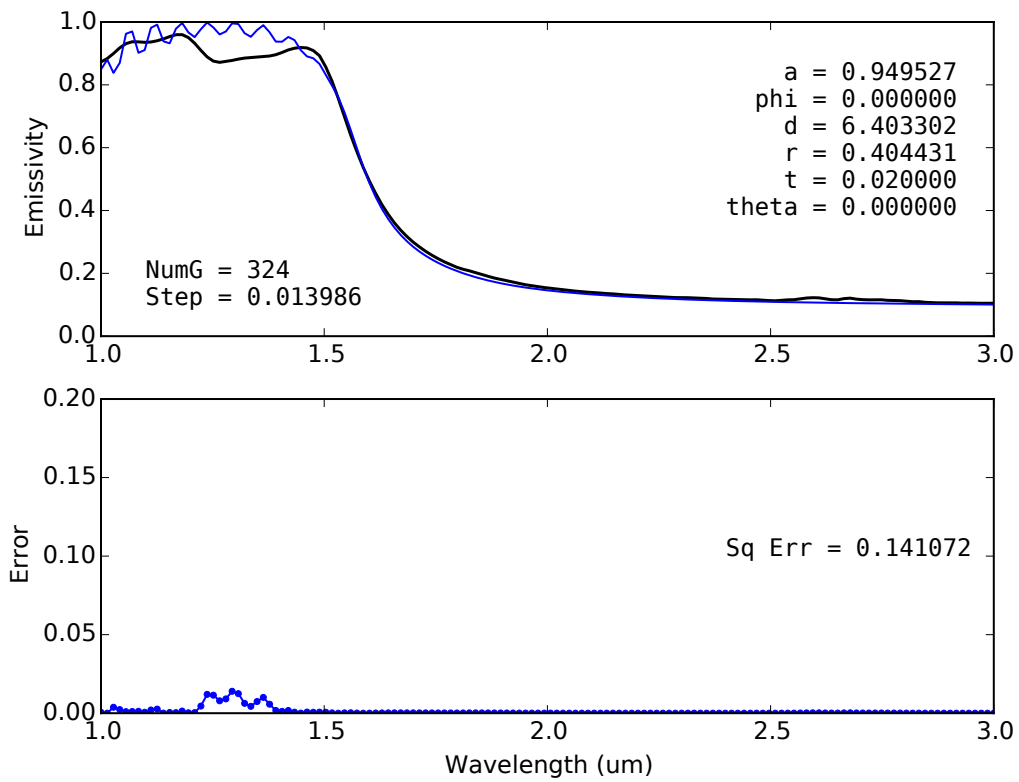


Figure D-2: Fitting of parameters of the photonic crystal with 1.7 μm cutoff.

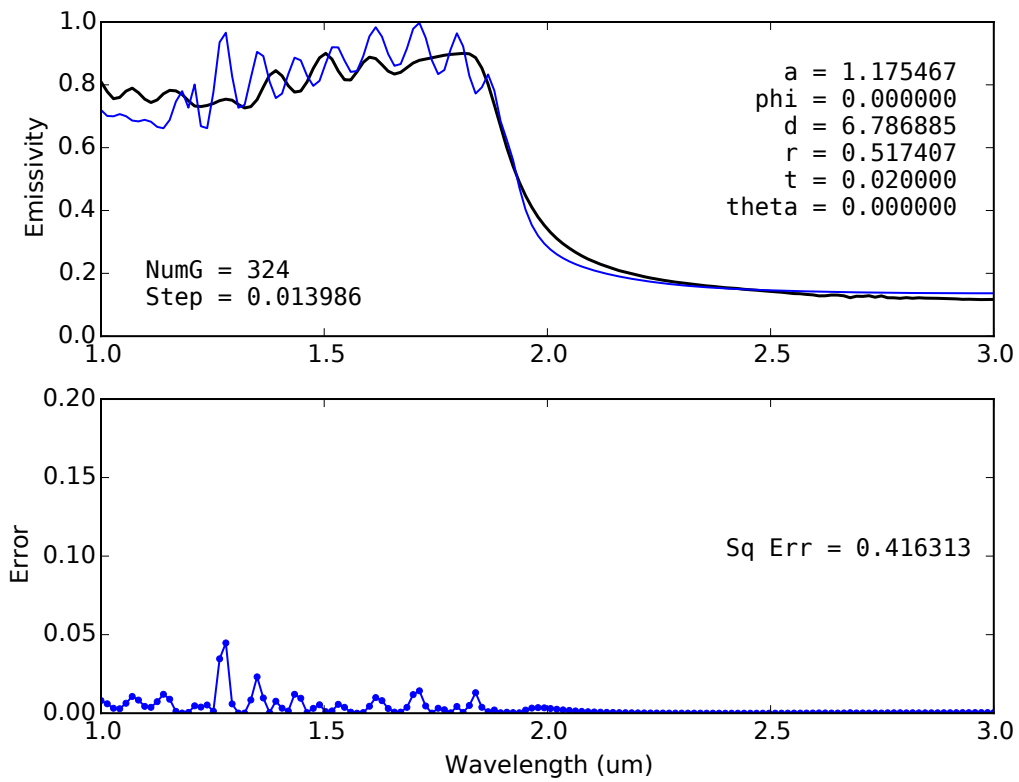


Figure D-3: Fitting of parameters of the photonic crystal with 2.0 μm cutoff.

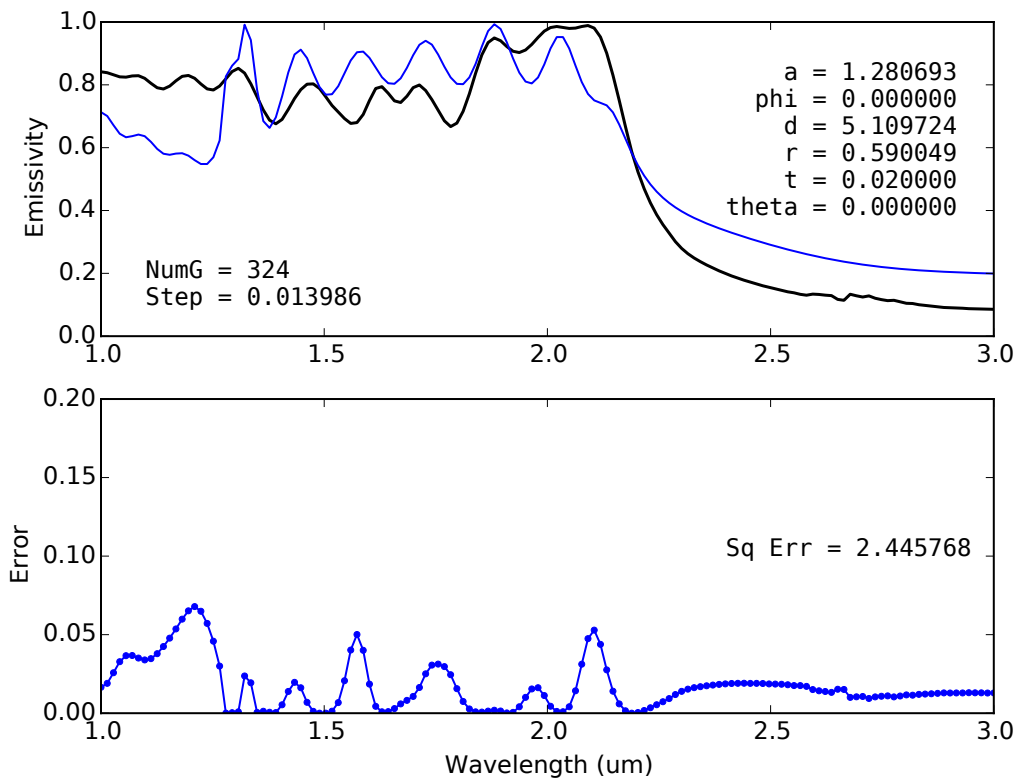


Figure D-4: Fitting of parameters of the photonic crystal with 2.3 μm cutoff.

with electricity, and is described in Ref. [13]. For the purpose of quantifying emitter performance, begin with combustion and end with in-band radiation, thus simplifying the model by only including at the thermal and optical domains.

We used a heat balance to predict the amount of power radiated from the emitter and the microburner temperature. To simplify the model, we assumed a perfectly insulated microburner whose only heat loss mechanism is the exhaust which is fundamental to the combustion. The resulting heat balance is

$$Q_{fuel} = Q_{exh}, \quad (\text{D.3})$$

where Q_{fuel} is the caloric content of the fuel and Q_{exh} is the heat carried out by the exhaust. The exhaust heat loss is given by a sum over the heat absorbed by the heat capacity of the reaction products:

$$Q_{exh} = \sum_{i \in \text{prod.}} \dot{n}_i \int_{T_a}^{T_b} C_{p,i}(T) dT \quad (\text{D.4})$$

$$\approx \sum_{i \in \text{prod.}} \dot{n}_i C_{p,i}(T_b - T_a) \quad (\text{D.5})$$

where T_a is the ambient temperature, T_b is the microburner temperature, $C_{p,i}$ and \dot{n}_i are the molar heat capacity and flow rate of species i , and the sum is over the reaction products i : CO_2 , H_2O , excess O_2 , and N_2 if using air. The exhaust loss can be approximated by Equation D.5 which assumes temperature independent heat capacities.

We can gain some intuition from a thermal circuit model, where heat is equivalent to current and temperature is equivalent to voltage. The heat of combustion is modeled as a current source and exhaust loss is modeled as a resistor, forming a Norton equivalent circuit as shown in the inset of Fig. D-5b. The temperature reached by the combustion decreases approximately linearly with the amount of heat extracted as in Fig. D-5b. The “short circuit current” is heat of combustion and the “open

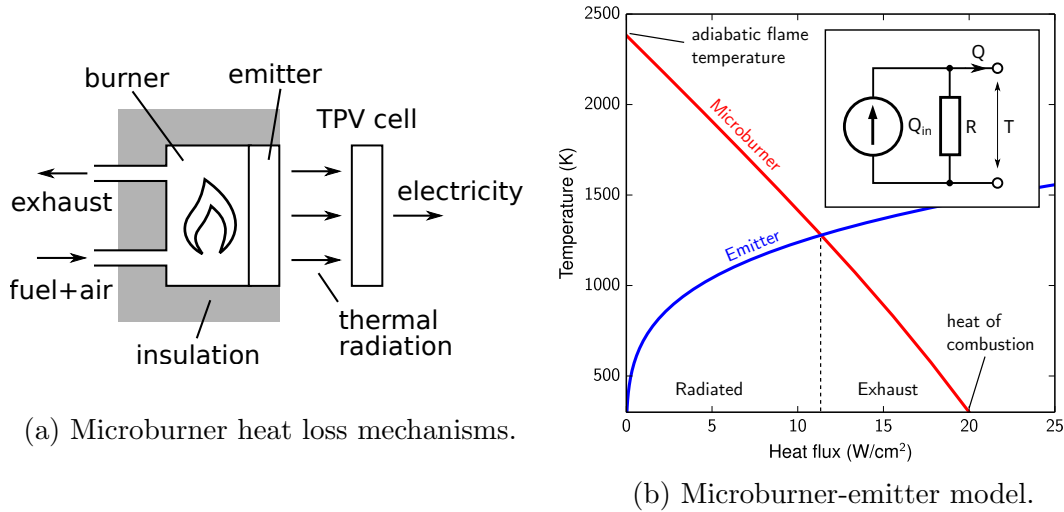


Figure D-5: (a) A simple microburner-emitter model only considering combustion, exhaust, thermal emission from the emitter. (b) Equivalent circuit model for combustion and the emitter.

circuit voltage” is the adiabatic flame temperature. The slight nonlinearity due to the temperature-dependent heat capacities in Equation D.4.

Non-exhaust loss mechanisms are loads to the Norton circuit. As an example, we coupled the microburner to a grey body emitter whose radiated power is given by the Stefan-Boltzmann law

$$Q_{rad} = A_e \varepsilon_e \sigma T_b^4 \quad (D.6)$$

where ε_e is the emissivity, A_e is the area, σ is the Stefan-Boltzmann constant, and T_b is the microburner temperature. A single $\varepsilon_e = 1$ curve is plotted in Fig. D-5b. The microburner and emitter share a single temperature and heat flux, thus the operating point is the intersection of the two curves. The fraction of the heat to the left of the intersection is radiated by the emitter and the fraction to the right is carried out the exhaust. This fraction is termed the burner efficiency. An efficient TPV system requires an effective “impedance match” to maximize transfer heat from the microburner to the emitter, which is obtained with a high emissivity emitter and low temperature microburner.

In this model, we used a wavelength-dependent emissivity of the emitter. If we assume that the amount of radiation reflected from the cell is small, the heat loss can be approximated from the the emissivity of the emitter:

$$Q_{rad} \approx A_e \int_0^{\infty} \varepsilon_e(\lambda) e_b(\lambda, T_b) d\lambda, \quad (\text{D.7})$$

where $\varepsilon_e(\lambda)$ is the wavelength dependent emissivity and $e_b(\lambda, T_e)$ is the blackbody spectrum given by Planck's Law,

$$e_b(\lambda, T) = \frac{2hc^2}{\lambda^5} \frac{1}{e^{\frac{hc}{\lambda k_B T}} - 1} \quad (\text{D.8})$$

where λ is the wavelength, h is Plank's constant, c is the speed of light, k_B is the Boltzmann constant, and T is the absolute temperature.

The complete heat balance model becomes

$$Q_{fuel} = Q_{exh} + Q_{rad} \quad (\text{D.9})$$

where Q_{rad} is divided into in-band and out-of-band emission. In-band emission is

$$Q_{in} \approx A_e \int_0^{\lambda_{PV}} \varepsilon_e(\lambda) e_b(\lambda, T_b) d\lambda, \quad (\text{D.10})$$

where λ_{PV} is the bandgap of the PV cell. The figure of merit used to evaluate different emitters is the hot side efficiency

$$\eta_{hs} = \frac{Q_{in}}{Q_{fuel}}. \quad (\text{D.11})$$

This figure of merit rewards emitter for high in-band emissivity and punishes emitters for high out-of-band emissivity.

Bibliography

- [1] W. R. Chan, V. Stelmakh, M. Ghebrebrhan, M. Soljačić, J. D. Joannopoulos, and I. Čelanović, “Enabling efficient heat-to-electricity generation at the mesoscale,” *Energy Environ. Sci.*, 2017.
- [2] A. H. Epstein, “Millimeter-scale, mems gas turbine engines,” in *Proc. ASME Turbo Expo*, vol. GT-2003-38, 2003.
- [3] O. Dessornes, S. Landais, R. Valle, A. Fourmaux, S. Burguburu, C. Zwysig, and Z. Kozanecki, “Advances in the Development of a Microturbine Engine,” *J. Eng. Gas Turbines Power*, vol. 136, no. 7, p. 71201, 2014.
- [4] A. Gomez, J. J. Berry, S. Roychoudhury, B. Coriton, and J. Huth, “From jet fuel to electric power using a mesoscale, efficient Stirling cycle,” *Proc. Combust. Inst.*, vol. 31, no. 2, pp. 3251–3259, 2007.
- [5] A. Kundu, J. H. Jang, J. H. Gil, C. R. Jung, H. R. Lee, S.-H. Kim, B. Ku, and Y. S. Oh, “Micro-fuel cells current development and applications,” *J. Power Sources*, vol. 170, pp. 67–78, 2007.
- [6] A. Bieberle-Hutter, D. Beckel, A. Infortuna, U. P. Muecke, J. L. M. Rupp, L. J. Gauckler, S. Rey-Mermet, P. Mural, N. R. Bieri, N. Hotz, M. J. Stutz, D. Poulidakos, P. Heeb, P. Müller, A. Bernard, R. Gmur, and T. Hocker, “A micro-solid oxide fuel cell system as battery replacement,” *J. Power Sources*, vol. 177, no. 1, pp. 123–130, 2008.
- [7] C. H. Marton, G. S. Haldeman, and K. F. Jensen, “Portable Thermoelectric Power Generator Based on a Microfabricated Silicon Combustor with Low Resistance to Flow,” *Ind. Eng. Chem. Res.*, vol. 50, no. 14, pp. 8468–8475, 2011.
- [8] K. Yoshida, S. Tanaka, S. Tomonari, D. Satoh, and M. Esashi, “High-energy density miniature thermoelectric generator using catalytic combustion,” *J. Microelectromech. Syst.*, vol. 15, pp. 195–203, 2006.
- [9] E. Doyle, K. Shukla, and C. Metcalfe, “Development and Demonstration of a 25 Watt Thermophotovoltaic Power Source for a Hybrid Power System,” Tech. Rep. August, NASA, 2001.

- [10] B. Bitnar, W. Durisch, and R. Holzner, “Thermophotovoltaics on the move to applications,” *Appl. Energy*, vol. 105, pp. 430–438, 2013.
- [11] W. R. Chan, P. Bermel, R. C. N. Pilawa-Podgurski, C. H. Marton, K. F. Jensen, J. J. Senkevich, J. D. Joannopoulos, M. Soljacic, and I. Celanovic, “Toward high-energy-density, high-efficiency, and moderate-temperature chip-scale thermophotovoltaics,” *Proc. Natl. Acad. Sci.*, vol. 110, no. 14, pp. 5309–5314, 2013.
- [12] C.-X. Zu and H. Li, “Thermodynamic analysis on energy densities of batteries,” *Energy Environ. Sci.*, vol. 4, pp. 2614–2624, 2011.
- [13] W. Chan, *High efficiency thermophotovoltaic microgenerators*. PhD thesis, Massachusetts Institute of Technology, 2015.
- [14] R. E. Nelson, “A brief history of thermophotovoltaic development,” *Semicond. Sci. Technol.*, vol. 18, pp. S141–S143, May 2003.
- [15] M. Zenker and A. Heinzl, “Efficiency and power density potential of combustion-driven thermophotovoltaic systems using GaSb photovoltaic cells,” *IEEE Trans. Electron Devices*, vol. 48, no. 2, pp. 367–376, 2001.
- [16] D. M. Bierman, A. Lenert, W. R. Chan, B. Bhatia, I. Celanović, M. Soljačić, and E. N. Wang, “Enhanced photovoltaic energy conversion using thermally based spectral shaping,” *Nature Energy*, vol. 1, p. 16068, 2016.
- [17] X. Wang, W. Chan, V. Stelmakh, I. Celanovic, and P. Fisher, “Toward high performance radioisotope thermophotovoltaic systems using spectral control,” *Nuclear Instruments and Methods in Physics Research Section A: Accelerators, Spectrometers, Detectors and Associated Equipment*, vol. 838, pp. 28 – 32, 2016.
- [18] V. M. Andreev, S. V. Sorokina, N. K. Timoshina, V. P. Khvostikov, and M. Z. Shvarts, “Solar cells based on gallium antimonide,” *Semiconductors*, vol. 43, no. 5, pp. 668–671, 2009.
- [19] B. Wernsman, R. R. Siergiej, S. D. Link, R. G. Mahorter, M. N. Palmisiano, R. J. Wehrer, R. W. Schultz, G. P. Schmuck, R. L. Messham, S. Murray, C. S. Murray, F. Newman, D. Taylor, D. M. DePoy, and T. Rahmlow, “Greater than 20% radiant heat conversion efficiency of a thermophotovoltaic radiator/module system using reflective spectral control,” *IEEE Trans. Electron Devices*, vol. 51, no. 3, pp. 512–515, 2004.
- [20] M. W. Dashiell, J. F. Beausang, H. Ehsani, G. J. Nichols, D. M. Depoy, L. R. Danielson, P. Talamo, K. D. Rahner, E. J. Brown, S. R. Burger, P. M. Fourspring, W. F. Topper, P. F. Baldasaro, C. A. Wang, R. K. Huang, M. K. Connors, G. W. Turner, Z. a. Shellenbarger, G. Taylor, J. Li, R. Martinelli,

- D. Donetski, S. Anikeev, G. L. Belenky, and S. Luryi, "Quaternary InGaAsSb thermophotovoltaic diodes," *IEEE Trans. Electron Devices*, vol. 53, no. 12, pp. 2879–2888, 2006.
- [21] Y. X. Yeng, W. R. Chan, V. Rinnerbauer, V. Stelmakh, J. J. Senkevich, J. D. Joannopoulos, M. Soljacic, and I. Čelanović, "Photonic crystal enhanced silicon cell based thermophotovoltaic systems," *Optics Express*, vol. 23, p. A157, jan 2015.
- [22] F. O'Sullivan, I. Celanovic, N. Jovanovic, J. Kassakian, S. Akiyama, and K. Wada, "Optical characteristics of one-dimensional Si/SiO₂ photonic crystals for thermophotovoltaic applications," *J. Appl. Phys.*, vol. 97, no. 3, 2005.
- [23] T. Rahmlow, J. Lazo-Wasem, and E. Gratrix, "Front Surface Tandem Filters using Sapphire (Al₂O₃) Substrates for Spectral Control in Thermophotovoltaic Energy Conversion Systems," Tech. Rep. LM-05K032, US Department of Energy, 2005.
- [24] P. M. Fourspring, D. M. DePoy, T. D. R. Jr., J. E. Lazo-Wasem, and E. J. Gratrix, "Optical coatings for thermophotovoltaic spectral control," *Appl. Opt.*, vol. 45, no. 7, pp. 1356–1358, 2006.
- [25] T. D. Rahmlow, D. M. DePoy, P. M. Fourspring, H. Ehsani, J. E. Lazo-Wasem, and E. J. Gratrix, "Development of front surface, spectral control filters with greater temperature stability for thermophotovoltaic energy conversion," in *Seventh World Conf. Thermophotovoltaic Gener. Electr.* (C. Algora and V. Corregidor, eds.), pp. 59–67, American Institute of Physics, 2007.
- [26] R. T. Kristensen, J. F. Beausang, and D. M. DePoy, "Frequency selective surfaces as near-infrared electromagnetic filters for thermophotovoltaic spectral control," *J. Appl. Phys.*, vol. 95, no. 9, pp. 4845–4851, 2004.
- [27] V. Stelmakh, V. Rinnerbauer, R. D. Geil, P. R. Aimone, J. J. Senkevich, J. D. Joannopoulos, M. Soljačić, and I. Celanovic, "High-temperature tantalum tungsten alloy photonic crystals: Stability, optical properties, and fabrication," *Applied Physics Letters*, vol. 103, p. 123903, sep 2013.
- [28] B. Bitnar, W. Durisch, J. C. Mayor, H. Sigg, and H. R. Tschudi, "Characterisation of rare earth selective emitters for thermophotovoltaic applications," *Sol. Energy Mater. Sol. Cells*, vol. 73, no. 3, pp. 221–234, 2002.
- [29] C. Schlemmer, J. Aschaber, V. Boerner, and J. Luther, "Thermal stability of micro-structured selective tungsten emitters," in *AIP Conf. Proc.*, vol. 653, pp. 164–173, 2003.

- [30] H. Sai, Y. Kanamori, and H. Yugami, "High-temperature resistive surface grating for spectral control of thermal radiation," *Appl. Phys. Lett.*, vol. 82, no. 11, pp. 1685–1687, 2003.
- [31] N. R. Denny, S. E. Han, D. J. Norris, and A. Stein, "Effects of thermal processes on the structure of monolithic tungsten and tungsten alloy photonic crystals," *Chem. Mater.*, vol. 19, pp. 4563–4569, 2007.
- [32] N. R. Denny, F. Li, D. J. Norris, and A. Stein, "In situ high temperature TEM analysis of sintering in nanostructured tungsten and tungstenmolybdenum alloy photonic crystals," *J. Mater. Chem.*, vol. 20, no. 8, pp. 1538–1545, 2010.
- [33] K. A. Arpin, M. D. Losego, and P. V. Braun, "Electrodeposited 3D tungsten photonic crystals with enhanced thermal stability," *Chem. Mater.*, vol. 23, no. 21, pp. 4783–4788, 2011.
- [34] S. G. Rudisill, Z. Wang, and A. Stein, "Maintaining the structure of templated porous materials for reactive and high-temperature applications," *Langmuir*, vol. 28, pp. 7310–7324, 2012.
- [35] K. A. Arpin, M. D. Losego, A. N. Cloud, H. Ning, J. Mallek, N. P. Sergeant, L. Zhu, Z. Yu, B. Kalanyan, G. N. Parsons, G. S. Girolami, J. R. Abelson, S. Fan, and P. V. Braun, "Three-dimensional self-assembled photonic crystals with high temperature stability for thermal emission modification.," *Nat. Commun.*, vol. 4, p. 2630, 2013.
- [36] H. J. Lee, K. Smyth, S. Bathurst, J. B. Chou, M. Ghebrehbrhan, J. D. Joannopoulos, N. Saka, and S.-G. Kim, "Hafnia-plugged microcavities for thermal stability of selective emitters," *Appl. Phys. Lett.*, vol. 102, no. 24, 2013.
- [37] D. Peykov, Y. X. Yeng, I. Celanovic, J. D. Joannopoulos, and C. A. Schuh, "Effects of surface diffusion on high temperature selective emitters," *Opt. Express*, vol. 23, no. 8, p. 9979, 2015.
- [38] V. Rinnerbauer, S. Ndao, Y. Xiang Yeng, J. J. Senkevich, K. F. Jensen, J. D. Joannopoulos, M. Soljacic, I. Celanovic, and R. D. Geil, "Large-area fabrication of high aspect ratio tantalum photonic crystals for high-temperature selective emitters," *J. Vac. Sci. Technol. B Microelectron. Nanom. Struct.*, vol. 31, no. 1, p. 11802, 2013.
- [39] V. Rinnerbauer, Y. X. Yeng, W. R. Chan, J. J. Senkevich, J. D. Joannopoulos, M. Soljačić, and I. Celanovic, "High-temperature stability and selective thermal emission of polycrystalline tantalum photonic crystals.," *Opt. Express*, vol. 21, no. 9, pp. 11482–91, 2013.

- [40] V. Stelmakh, D. Peykov, W. R. Chan, J. J. Senkevich, J. D. Joannopoulos, M. Soljačić, I. Celanovic, R. Castillo, K. Coulter, and R. Wei, “Thick sputtered tantalum coatings for high-temperature energy conversion applications,” *Journal of Vacuum Science & Technology A: Vacuum, Surfaces, and Films*, vol. 33, p. 061204, nov 2015.
- [41] V. Stelmakh, V. Rinnerbauer, W. R. Chan, J. J. Senkevich, J. D. Joannopoulos, M. Soljagic, and I. Celanovic, “Performance of tantalum-tungsten alloy selective emitters in thermophotovoltaic systems,” in *Energy Harvesting and Storage: Materials, Devices, and Applications V* (N. K. Dhar, P. Balaya, and A. K. Dutta, eds.), SPIE, jun 2014.
- [42] P. Nagpal, D. P. Josephson, N. R. Denny, J. DeWilde, D. J. Norris, and A. Stein, “Fabrication of carbon/refractory metal nanocomposites as thermally stable metallic photonic crystals,” *J. Mater. Chem.*, vol. 21, no. 29, p. 10836, 2011.
- [43] V. Rinnerbauer, S. Ndao, Y. X. Yeng, W. R. Chan, J. J. Senkevich, J. D. Joannopoulos, M. Soljačić, and I. Celanovic, “Recent developments in high-temperature photonic crystals for energy conversion,” *Energy Environ. Sci.*, vol. 5, no. 10, p. 8815, 2012.
- [44] A. Heinzl, V. Boerner, A. Gombert, B. Blasi, V. Wittwer, and J. Luther, “Radiation filters and emitters for the NIR based on periodically structured metal surfaces,” *J. Mod. Opt.*, vol. 47, no. 13, pp. 2399–2419, 2000.
- [45] H. Sai and H. Yugami, “Thermophotovoltaic generation with selective radiators based on tungsten surface gratings,” *Appl. Phys. Lett.*, vol. 85, no. 16, pp. 3399–3401, 2004.
- [46] E. Rephaeli and S. Fan, “Tungsten black absorber for solar light with wide angular operation range,” *Appl. Phys. Lett.*, vol. 92, no. 21, p. 211107, 2008.
- [47] I. Celanovic, N. Jovanovic, and J. Kassakian, “Two-dimensional tungsten photonic crystals as selective thermal emitters,” *Appl. Phys. Lett.*, vol. 92, no. 19, p. 193101, 2008.
- [48] J. D. Joannopoulos, P. R. Villeneuve, and S. Fan, “Photonic crystals: putting a new twist on light,” 1997.
- [49] Y. X. Yeng, M. Ghebrebrhan, P. Bermel, W. R. Chan, J. D. Joannopoulos, M. Soljagic, and I. Celanovic, “Enabling high-temperature nanophotonics for energy applications,” *Proc. Natl. Acad. Sci.*, vol. 109, no. 7, pp. 2280–2285, 2012.

- [50] M. Ghebrebrhan, P. Bermel, Y. X. Yeng, I. Celanovic, M. Soljagic, and J. D. Joannopoulos, "Tailoring thermal emission via Q matching of photonic crystal resonances," *Phys. Rev. A - At. Mol. Opt. Phys.*, vol. 83, no. 3, pp. 1–6, 2011.
- [51] I. Celanovic, F. O'Sullivan, M. Ilak, J. Kassakian, and D. Perreault, "Design and Optimization of One-Dimensional Photonic Crystals for Thermophotovoltaic Applications," *Opt. Lett.*, vol. 29, p. 863, 2004.
- [52] S. Y. Lin, J. Moreno, and J. G. Fleming, "Three-dimensional photonic-crystal emitter for thermal photovoltaic power generation," *Appl. Phys. Lett.*, vol. 83, pp. 380–382, jul 2003.
- [53] Y. X. Yeng, J. B. Chou, V. Rinnerbauer, Y. Shen, S.-G. Kim, J. D. Joannopoulos, M. Soljagic, and I. Čelanović, "Global optimization of omnidirectional wavelength selective emitters/absorbers based on dielectric-filled anti-reflection coated two-dimensional metallic photonic crystals," *Opt. Express*, vol. 22, no. 18, p. 21711, 2014.
- [54] V. Stelmakh, W. R. Chan, M. Ghebrebrhan, M. Soljagic, J. D. Joannopoulos, and I. Celanovic, "Fabrication of an Omnidirectional 2D Photonic Crystal Emitter for Thermophotovoltaics," *Journal of Physics: Conference Series*, vol. 773, p. 012037, dec 2016.
- [55] G. E. Guazzoni, "High- temperature spectral emittance of oxides of erbium, samarium, neodymium and ytterbium," *Appl. Spectrosc.*, vol. 26, pp. 60–65, January 1972.
- [56] "ReffIT description." <https://sites.google.com/site/reffitprogram/home>. Accessed: 2017-04-23.
- [57] Y. S. Touloukian, R. K. Kirby, R. E. Taylor, and P. D. Desai, *Thermophysical Properties of Matter, Volume 12: Thermal Expansion, Metallic Elements and Alloys*. New York, NY: IFI/Plenum, 1975.
- [58] A. F. Oskooi, D. Roundy, M. Ibanescu, P. Bermel, J. D. Joannopoulos, and S. G. Johnson, "Meep: A flexible free-software package for electromagnetic simulations by the FDTD method," *Comput. Phys. Commun.*, vol. 181, no. 3, pp. 687–702, 2010.
- [59] V. Liu and S. Fan, "S4: A free electromagnetic solver for layered periodic structures," *Comput. Phys. Commun.*, vol. 183, no. 10, pp. 2233–2244, 2012.
- [60] S. G. Johnson, "The NLOpt nonlinear-optimization package."
- [61] I. Celanovic, M. Ghebrebrhan, Y. X. Yeng, J. Kassakian, M. Soljačić, and J. D. Joannopoulos, "Photonic Crystals: Shaping the Flow of Thermal Radiation," *MRS Proc.*, vol. 1162, 2009.

- [62] M. Araghchini, Y. X. Yeng, N. Jovanovic, P. Bermel, L. A. Kolodziejski, M. Soljagic, I. Celanovic, and J. D. Joannopoulos, "Fabrication of two-dimensional tungsten photonic crystals for high-temperature applications," 2011.
- [63] V. Stelmakh, W. R. Chan, M. Ghebrebrhan, M. Soljagic, J. D. Joannopoulos, and I. Celanovic, "Photonic crystal emitters for thermophotovoltaic energy conversion," *Journal of Physics: Conference Series*, vol. 660, p. 012080, dec 2015.
- [64] V. Stelmakh, W. R. Chan, M. Ghebrebrhan, J. Senkevich, J. D. Joannopoulos, M. Soljagic, and I. Celanovic, "Sputtered tantalum photonic crystal coatings for high-temperature energy conversion applications," *IEEE Transactions on Nanotechnology*, vol. 15, pp. 303–309, mar 2016.
- [65] H. S. I. Paul Aimone. private communication, 2013.
- [66] M. E. Walsh, *On the design of lithographic interferometers and their application*. Thesis (Ph.D.), Massachusetts Institute of Technology, 2004.
- [67] V. Rinnerbauer, J. J. Senkevich, J. D. Joannopoulos, M. Soljagic, I. Celanovic, R. R. Harl, B. R. Rogers, M. Soljagic, I. Celanovic, R. R. Harl, and B. R. Rogers, "Low emissivity high-temperature tantalum thin film coatings for silicon devices," *J. Vac. Sci. Technol. A Vacuum, Surfaces, Film.*, vol. 31, no. 1, p. 011501, 2013.
- [68] J. B. Chou, Y. X. Yeng, A. Lenert, V. Rinnerbauer, I. Celanovic, M. Soljačić, E. N. Wang, and S.-G. Kim, "Design of wide-angle selective absorbers/emitters with dielectric filled metallic photonic crystals for energy applications," *Opt. Express*, vol. 22 Suppl 1, no. January, pp. A144–54, 2014.
- [69] W. R. Chan, B. A. Wilhite, J. J. Senkevich, M. Soljagic, J. Joannopoulos, and I. Celanovic, "An all-metallic microburner for a millimeter-scale thermophotovoltaic generator," in *Journal of Physics: Conference Series*, vol. 476, p. 12017, 2013.
- [70] D. Wilt, R. Wehrer, M. Palmisiano, M. Wanlass, and C. Murray, "Monolithic interconnected modules (MIMs) for thermophotovoltaic energy conversion," *Semicond. Sci. Technol.*, vol. 18, no. 5, pp. S209–S215, 2003.
- [71] V. Stelmakh, W. R. Chan, J. D. Joannopoulos, M. Soljagic, I. Celanovic, and K. Sablon, "Improved thermal emitters for thermophotovoltaic energy conversion," in *Volume 1: Micro/Nanofluidics and Lab-on-a-Chip; Nanofluids; Micro/Nanoscale Interfacial Transport Phenomena; Micro/Nanoscale Boiling and Condensation Heat Transfer; Micro/Nanoscale Thermal Radiation; Micro/Nanoscale Energy Devices and Systems*, ASME, jan 2016.

- [72] D. Woolf, J. Hensley, J. G. Cederberg, D. T. Bethke, A. D. Grine, and E. A. Shaner, "Heterogeneous metasurface for high temperature selective emission," *Applied Physics Letters*, vol. 105, no. 8, p. 081110, 2014.
- [73] H. Sai, Y. Kanamori, and H. Yugami, "Tuning of the thermal radiation spectrum in the near-infrared region by metallic surface microstructures," 2005.
- [74] H. H. Kolm, "Solar-battery power source," tech. rep., MIT-Lincoln Laboratory Group 35, 1956.
- [75] D. C. White, B. D. Wedlock, and J. Blair, "Recent advance in thermal energy conversion," in *Proc. 15th Power Sources Conf.*, pp. 125–32, 1961.
- [76] B. D. Wedlock, "Thermophotovoltaic conversion," in *Proc. IEEE*, vol. 51, pp. 694–698, 1963.
- [77] P. E. Gray and *et al.*, "Investigation of a pin-structure germanium photovoltaic cell," tech. rep., Massachusetts Institute of Technology (Cambridge, MA), 1968.
- [78] R. J. Schwartz and *et al.*, "Pin structures for controlled spectrum photovoltaic converters," in *Proc. of NATO AGARD Conf. (Cannes, France)*, pp. 897–922, March 16-20 1964.
- [79] R. J. Schwartz and *et al.*, "A theoretical and experimental investigation of planar pin thermophotovoltaic cells," tech. rep., Purdue University (Lafayette, IN), 1968.
- [80] E. Kittl and G. Guazzoni, "Design analysis of TPV-generator system," in *Proc. 25th Power Sources Symp.*, pp. 106–9, 1972.
- [81] R. W. Haushalter, "Engineering investigation of a thermophotovoltaic energy converter," tech. rep., General Motors Defense Research Laboratories (Santa Barbara, CA), 1966.
- [82] J. J. Werth, "Thermo-photovoltaic converter with radiant energy reflective means," 1963. US Patent 3,331,707.
- [83] R. M. Swanson, "Recent developments in thermophotovoltaic conversion," in *Proc. Int. Electron Devices Meeting (Washington, DC)*, pp. 186–9, December 8-10 1980.
- [84] W. E. Horne, "Conversion of solar to electrical energy," 1977. US Patent 4,313,024.
- [85] P. Wurfel and W. Ruppel, "Upper limit of thermophotovoltaic solar energy conversion," in *IEEE Trans. Electron Devices*, vol. 27, pp. 745–50, 1980.

- [86] F. Demichelis and E. Minetti-Mezzetti, "A solar thermophotovoltaic converter," *Solar Cells*, vol. 1, no. 4, pp. 395 – 403, 1980.
- [87] L. D. Woolf, J. C. Bass, and N. B. Elsner, "Theoretical and experimental investigation of variable band gap cells in thermophotovoltaic energy conversion," in *32nd International Power Sources Symposium* (N. A. Godshall and A. R. Baldwin, eds.), pp. 101–109, 1986.
- [88] C. A. Wang, H. K. Choi, S. L. Ransom, G. W. Charache, L. R. Danielson, and D. M. DePoy, "High-quantum-efficiency $\{0.5\text{eV}\}$ $\{\text{GaInAsSb}\}/\{\text{GaSb}\}$ thermophotovoltaic devices," *Appl. Phys. Lett.*, vol. 75, no. 9, pp. 1305–1307, 1999.
- [89] O. V. Sulima, "GaSb-, InGaAsSb-, InGaSb-, InAsSCP- AND Ge-TPV CELLS WITH DIFFUSED EMITTERS," *Jet Propuls.*, pp. 2000–2003, 2000.
- [90] O. V. Sulima and a. W. Bett, "Fabrication and simulation of GaSb thermophotovoltaic cells," *Sol. Energy Mater. Sol. Cells*, vol. 66, no. 1-4, pp. 533–540, 2001.
- [91] V. Andreev, V. Khvostikov, and A. Vlasov, "Solar thermophotovoltaics," *Springer Ser. Opt. Sci.*, vol. 130, pp. 175–197, 2007.
- [92] M. W. Dashiell, J. F. Beausang, H. Ehsani, G. J. Nichols, D. M. Depoy, L. R. Danielson, P. Talamo, K. D. Rahner, E. J. Brown, S. R. Burger, P. M. Fourspring, W. F. Topper, P. F. Baldasaro, C. A. Wang, R. K. Huang, M. K. Connors, G. W. Turner, Z. a. Shellenbarger, G. Taylor, J. Li, R. Martinelli, D. Donetski, S. Anikeev, G. L. Belenky, S. Luryi, W. F. T. Jr., P. F. Baldasaro, C. A. Wang, R. K. Huang, M. K. Connors, G. W. Turner, Z. a. Shellenbarger, G. Taylor, J. Li, R. Martinelli, D. Donetski, S. Anikeev, G. L. Belenky, and S. Luryi, "Quaternary InGaAsSb thermophotovoltaic diodes," *IEEE Trans. Electron Devices*, vol. 53, no. 12, pp. 2879–2888, 2006.
- [93] R. E. Nelson, "Thermophotovoltaic technology," 1983. US Patent 4,584,426.
- [94] D. L. Chubb, "Reappraisal of solid selective emitters," in *IEEE Conference on Photovoltaic Specialists*, pp. 1326–1333 vol.2, May 1990.
- [95] T. D. Rahmlow, J. E. Laxo-Wasem, E. J. Gratrix, P. M. Fourspring, and D. M. DePoy, "New performance levels for TPV front surface filters," in *Sixth Conf. Thermophotovoltaic Gener. Electr.* (A. Gopinath, T. J. Coutts, and J. Luther, eds.), pp. 180–188, American Institute of Physics, 2004.
- [96] T. D. Rahmlow, D. M. DePoy, P. M. Fourspring, H. Ehsani, J. E. Lazo-Wasem, and E. J. Gratrix, "Development of front surface, spectral control filters with

- greater temperature stability for thermophotovoltaic energy conversion,” in *Seventh World Conf. Thermophotovoltaic Gener. Electr.* (C. Algora and V. Corregidor, eds.), pp. 59–67, American Institute of Physics, 2007.
- [97] P. Nagpal, S. E. Han, A. Stein, and D. J. Norris, “Efficient low-temperature thermophotovoltaic emitters from metallic photonic crystals,” *Nano Lett.*, vol. 8, no. 10, pp. 3238–3243, 2008.
- [98] A. Lenert, D. M. Bierman, Y. Nam, W. R. Chan, I. Celanovic, M. Soljačić, and E. N. Wang, “A nanophotonic solar thermophotovoltaic device,” *Nat. Nanotechnol.*, vol. 9, no. January, pp. 1–5, 2014.
- [99] M. Kaminsky and S. K. Das, “Effect of channeling and irradiation temperature on the morphology of blisters in niobium,” *Appl. Phys. Lett.*, vol. 21, no. 9, pp. 443–445, 1972.
- [100] S. K. Das and M. Kaminsky, “Blistering in helium-ion-implanted (111) niobium monocrystals,” *J. Appl. Phys.*, vol. 44, no. 6, pp. 2520–2529, 1973.
- [101] M. Kaminsky and S. K. Das, “Orientation dependence of blister shape in niobium monocrystals implanted with channeled helium ions,” *Appl. Phys. Lett.*, vol. 23, no. 6, pp. 293–295, 1973.
- [102] M. Kaminsky and S. K. Das, “Blistering of polycrystalline and monocrystalline niobium,” *Rad. Effects*, vol. 18, no. 3-4, pp. 245–250, 1973.
- [103] S. K. Das and M. Kaminsky, “Radiation blistering of structural materials for fusion devices and reactors,” *J. Nucl. Mater.*, vol. 53, pp. 115–122, 1974.
- [104] S. K. Das and M. Kaminsky, “Radiation blistering in metals and alloys,” *Adv. Chem. Ser.*, vol. 158, pp. 112–170, 1976.
- [105] D. Ghose, D. Basu, and S. B. Karmohapatro, “Formation of blisters in tantalum by 30 mev alpha particle bombardment,” *J. Nucl. Mater.*, vol. 125, no. 3, pp. 342–345, 1984.
- [106] D. Ghose, S. R. Bhattacharya, D. Basu, and S. B. Karmohapatro, “Blistering of tantalum foils during alpha particle bombardment,” *J. Nucl. Mater.*, vol. 144, no. 3, pp. 282–286, 1987.
- [107] J. E. Spruiell, “The oxidation of columbium at 850°C in oxygen at low pressures,” Master’s thesis, University of Tennessee, 1960.
- [108] R. E. Clausing, C. J. McHargue, and J. E. Spruiell, “Some remarks on the importance of contaminants in high temperature applications of niobium and vanadium,” *J. Nucl. Mater.*, vol. 53, pp. 123–124, 1974.

- [109] W. Bauer and G. J. Thomas, "Formation of surface features on niobium during high temperature hydrogen irradiation," *Rad. Effects*, vol. 23, no. 3, pp. 211–212, 1974.
- [110] T. W. Haas and J. T. Grant, "Chemical effects on the kll auger electron spectrum from surface carbon," *Appl. Phys. Lett.*, vol. 16, no. 4, pp. 172–173, 1970.
- [111] T. W. Haas, J. T. Grant, and G. J. Dooley III, "Chemical effects in auger electron spectroscopy," *J. Appl. Phys.*, vol. 43, no. 4, pp. 1853–1860, 1972.
- [112] S. M. Ko and L. D. Schmidt, "Adsorption and solution of h_2 , d_2 , n_2 , o_2 and co by (100) ta," *Surf. Sci.*, vol. 47, no. 2, pp. 557–568, 1975.
- [113] R. Ducros, G. Piquard, B. Weber, and A. Cassuto, "Spectres auger du carbone: Carbures de tantale et adsorption d'éthylène et de monoxyde de carbone sur tantale et rhénium polycristallin," *Surf. Sci.*, vol. 54, no. 2, pp. 513–518, 1976.
- [114] S. Craig, G. L. Harding, and R. Payling, "Auger lineshape analysis of carbon bonding in sputtered metal-carbon thin films," *Surf. Sci.*, vol. 124, no. 2, pp. 591–601, 1983.
- [115] A. Y. Tontegode, "Carbon on transition metal surfaces," *Prog. Surf. Sci.*, vol. 38, no. 3, pp. 201–429, 1991.
- [116] N. R. Gall, E. V. Rutkov, and A. Y. Tontegode, "Sequential ta (100) carbonisation: from adsorption of single carbon atoms to bulk carbide production," *Surf. Sci.*, vol. 472, no. 3, pp. 187–194, 2001.
- [117] E. K. Storms, *The Refractory Carbides*. New York, NY: Academic Press, 1967.
- [118] L. Kaufman, "Coupled thermochemical and phase diagram data for tantalum based binary alloys," *CALPHAD*, vol. 15, no. 3, pp. 243–259, 1991.
- [119] K. Frisk and A. Fernández Guillermet, "Gibbs energy coupling of the phase diagram and thermochemistry in the tantalum-carbon system," *J. Alloys Comp.*, vol. 238, no. 1, pp. 167–179, 1996.
- [120] G. J. Thomas and W. Bauer, "Carbide formation on nb surfaces during high-temperature h irradiation," *J. Vac. Sci. Technol.*, vol. 12, no. 1, pp. 490–495, 1975.
- [121] D. W. Lynch and W. Hunter, "An introduction to the data for several metals," in *Handbook of Optical Constants of Solids* (E. D. Palik, ed.), pp. 341 – 419, Burlington: Academic Press, 1997.

- [122] F. A. Modine, R. W. Major, T. W. Haywood, G. R. Gruzalski, and D. Y. Smith, "Optical properties of tantalum carbide from the infrared to the near ultraviolet," *Phys. Rev. B*, vol. 29, no. 2, pp. 836–841, 1984.
- [123] M. Sahnoun, C. Daul, J. C. Parlebas, C. Demangeat, and M. Driz, "Electronic structure and optical properties of tac from the first principles calculation," *Eur. Phys. J. B*, vol. 44, no. 3, pp. 281–286, 2005.
- [124] B. A. Mrowca, "Controlled Crystal Growth in Tantalum Ribbons," *Journal Appl. Phys.*, vol. 684, 1943.
- [125] L. Kirkbride, J. Basmajian, D. Stoller, W. Ferguson, R. Perkins, and D. Dunning, "The effect of yttrium on the recrystallization and grain growth of tantalum," *J. Less Common Met.*, vol. 9, no. 6, pp. 393–408, 1965.
- [126] P. Kumar and C. E. Mosheim, "Effect of intermetallic compounds on the properties of tantalum," *Int. J. Refract. Met. H.*, vol. 12, no. 1, pp. 35–40, 1994.
- [127] M. F. Hupalo and H. R. Z. Sandim, "The annealing behavior of oligocrystalline tantalum deformed by cold swaging," *Mater. Sci. Eng. A*, vol. 318, no. 1-2, pp. 216–223, 2001.
- [128] S. N. Mathaudhu and K. Ted Hartwig, "Grain refinement and recrystallization of heavily worked tantalum," *Mater. Sci. Eng. A*, vol. 426, no. 1-2, pp. 128–142, 2006.
- [129] V. Stelmakh, V. Rinnerbauer, J. D. Joannopoulos, M. Soljačić, I. Celanovic, J. J. Senkevich, C. Tucker, T. Ives, and R. Shrader, "Evolution of sputtered tungsten coatings at high temperature," *Journal of Vacuum Science & Technology A: Vacuum, Surfaces, and Films*, vol. 31, p. 061505, nov 2013.
- [130] T. Karabacak, C. R. Picu, J. J. Senkevich, G. C. Wang, and T. M. Lu, "Stress reduction in tungsten films using nanostructured compliant layers," *J. Appl. Phys.*, vol. 96, no. 10, pp. 5740–5746, 2004.
- [131] T. Karabacak, J. J. Senkevich, G.-C. Wang, and T.-M. Lu, "Stress reduction in sputter deposited films using nanostructured compliant layers by high working-gas pressures," *J. Vac. Sci. Technol. A Vacuum, Surfaces, Film.*, vol. 23, no. 4, p. 986, 2005.
- [132] Y. G. Shen, Y. W. Mai, Q. C. Zhang, D. R. McKenzie, W. D. McFall, and W. E. McBride, "Residual stress, microstructure, and structure of tungsten thin films deposited by magnetron sputtering," *J. Appl. Phys.*, vol. 87, no. 1, p. 177, 2000.

- [133] A. W. Sood, D. J. Poxson, F. W. Mont, S. Chhajed, J. Cho, E. F. Schubert, R. E. Welsler, N. K. Dhar, and A. K. Sood, "Experimental and Theoretical Study of the Optical and Electrical Properties of Nanostructured Indium Tin Oxide Fabricated by Oblique-Angle Deposition," *J. Nanosci. Nanotechnol.*, vol. 12, no. 5, pp. 3950–3953, 2012.
- [134] D. E. Aspnes, "Local-field effects and effective-medium theory: A microscopic perspective," 1982.
- [135] H. P. Klug and t. Alexander, Leroy Elbert, *X-ray diffraction procedures*. Wiley New York, 1954.
- [136] P. Petroff, T. T. Sheng, a. K. Sinha, G. a. Rozgonyi, and F. B. Alexander, "Microstructure, growth, resistivity, and stress in thin tungsten films deposited by RF sputtering," *J. Appl. Phys.*, vol. 44, no. 6, pp. 2545–2554, 1973.
- [137] I. C. Noyan, T. M. Shaw, and C. C. Goldsmith, "Inhomogeneous strain states in sputter deposited tungsten thin films," *J. Appl. Phys.*, vol. 82, no. 9, p. 4300, 1997.
- [138] S. M. Rossnagel, I. C. Noyan, and J. C. Cabral, "Phase transformation of thin sputter-deposited tungsten films at room temperature," *J. Vac. Sci. Technol. B*, vol. 20, 2002.
- [139] J. R. Groza and J. F. Shackelford, *Materials processing handbook*. CRC press, 2007.
- [140] R. G. Frieser, "A Review of Solder Glasses," *Electrocompon. Sci. Technol.*, vol. 2, no. 3, pp. 163–199, 1975.
- [141] J. H. Partridge, *Glass-To-Metal Seals*. Sheffield: The Society of Glass Technology, 1949.
- [142] M. Pelliccione and T.-M. Lu, *Evolution of Thin Film Morphology: Modeling and Simulations*. Springer-Verlag Berlin Heidelberg, New York, NY, 2008.
- [143] I. Noyan and J. Cohen, "An X-ray diffraction study of the residual stress-strain distributions in shot-peened two-phase brass," 1985.
- [144] I. C. Noyan, T. C. Huang, and B. R. York, "Residual stress/strain analysis in thin films by X-ray diffraction," 1995.
- [145] G. Simmons and H. Wang, *Single crystal elastic constants and calculated aggregate properties: a handbook*. Cambridge, MA: MIT Press, 1971.

- [146] D. A. Armstrong and B. L. Mordike, "The influence of alloying and temperature on the elastic constants of tantalum," *J. Less Common Met.*, vol. 22, no. 3, pp. 265–274, 1970.
- [147] R. G. Leisure, D. K. Hsu, and B. A. Seiber, "Elastic properties of tantalum over the temperature range 4–300 K," *J. Appl. Phys.*, vol. 44, no. 8, pp. 3394–3397, 1973.
- [148] W. L. S. III, J. M. Roberts, N. G. Alexandropolous, and K. Salama, "Effect of hydrogen on the temperature dependence of the elastic constants of tantalum single crystals," *J. Appl. Phys.*, vol. 48, pp. 75–81, 1977.
- [149] C. E. Anderson and F. R. Brotzen, "Elastic constants of tantalum-tungsten alloys," *J. Appl. Phys.*, vol. 53, no. 1, pp. 292–297, 1982.
- [150] D. W. Matson, E. D. McClanahan, J. P. Rice, S. L. Lee, and D. Windover, "Effect of sputtering parameters on Ta coatings for gun bore applications," *Surf. Coatings Technol.*, vol. 133–134, pp. 411–416, 2000.
- [151] D. W. Matson, E. D. McClanahan, S. L. Lee, and D. Windover, "Properties of thick sputtered Ta used for protective gun tube coatings," *Surf. Coatings Technol.*, vol. 146–147, pp. 344–350, 2001.
- [152] W. D. Westwood and F. C. Livermore, "Phase composition and conductivity of sputtered tantalum," *Thin Solid Films*, vol. 5, no. 5–6, pp. 407–420, 1970.
- [153] D. W. Hoffman and J. A. Thornton, "Internal stresses in Cr, Mo, Ta, and Pt films deposited by sputtering from a planar magnetron source," *J. Vac. Sci. Technol.*, vol. 20, no. 3, p. 355, 1982.
- [154] M. Grosser and U. Schmid, "The impact of sputter conditions on the microstructure and on the resistivity of tantalum thin films," *Thin Solid Films*, vol. 517, no. 16, pp. 4493–4496, 2009.
- [155] L. J. Cunningham and A. J. Braundmeier, "Measurement of the correlation between the specular reflectance and surface roughness of ag films," *Phys. Rev. B*, vol. 14, pp. 479–483, Jul 1976.
- [156] S. L. Lee, M. Cipollo, D. Windover, and C. Rickard, "Analysis of magnetron-sputtered tantalum coatings versus electrochemically deposited tantalum from molten salt," in *Surf. Coatings Technol.*, vol. 120–121, pp. 44–52, 1999.
- [157] L. Gladczuk, A. Patel, C. S. Paur, and M. Sosnowski, "Tantalum films for protective coatings of steel," *Thin Solid Films*, vol. 467, no. 1–2, pp. 150–157, 2004.

- [158] S. L. Lee, D. Windover, M. Audino, D. W. Matson, and E. D. McClanahan, "High-rate sputter deposited tantalum coating on steel for wear and erosion mitigation," *Surf. Coatings Technol.*, vol. 149, no. 1, pp. 62–69, 2002.
- [159] S. L. L. Lee and D. Windover, "Phase, residual stress, and texture in triode-sputtered tantalum coatings on steel," *Surf. Coatings Technol.*, vol. 108-109, pp. 65–72, 1998.
- [160] J. A. Thornton, "Internal stresses in titanium, nickel, molybdenum, and tantalum films deposited by cylindrical magnetron sputtering," 1977.
- [161] D. W. Hoffman and J. A. Thornton, "Effects of substrate orientation and rotation on internal stresses in sputtered metal films," *J. Vac. Sci. Technol.*, vol. 16, no. 2, p. 134, 1979.
- [162] L. A. Clevenger, A. Mutscheller, J. M. E. Harper, C. Cabral, and K. Barmak, "The relationship between deposition conditions, the beta to alpha phase transformation, and stress relaxation in tantalum thin films," *J. Appl. Phys.*, vol. 72, no. 10, pp. 4918–4924, 1992.
- [163] C. Cabral Jr., L. A. Clevenger, and R. G. Schad, "Repeated compressive stress increase with 400 °C thermal cycling in tantalum thin films due to increases in the oxygen content," *J. Vac. Sci. Technol. B*, vol. 12, pp. 2818–2821, 1994.
- [164] B. L. French and J. C. Bilello, "In situ observations of the real-time stress-evolution and delamination of thin Ta films on Si(100)," *Thin Solid Films*, vol. 446, no. 1, pp. 91–98, 2004.
- [165] R. Knepper, K. Jackson, B. Stevens, and S. P. Baker, "Thermomechanical behavior and microstructural evolution in tantalum thin films," *MRS Proc.*, vol. 854, p. U6.8, 2005.
- [166] M. H. Cheng, T. C. Cheng, W. J. Huang, M. N. Chang, and M. K. Chung, "Influence of oxygen diffusion on residual stress for tantalum thin films," *J. Vac. Sci. Technol. B Microelectron. Nanom. Struct.*, vol. 25, no. 1, p. 147, 2007.
- [167] Y. S. Touloukian, R. K. Kirby, R. E. Taylor, and P. D. Desai, *Thermophysical Properties of Matter, Volume 12: Thermal Expansion, Metallic Elements and Alloys*. New York, NY: IFI/Plenum, 1975.
- [168] J. A. Thornton and D. Hoffman, "Stress-related effects in thin films," 1989.
- [169] H. Windischmann, "Intrinsic stress in sputter-deposited thin films," *Crit. Rev. Solid State Mater. Sci.*, vol. 17, no. 6, pp. 547–596, 1992.

- [170] E. M. Savitskii, M. A. Tylkina, and I. A. Tayganova, "The recrystallization diagram of tantalum," *Dokl. Akad. Nauk. SSSR*, vol. 118, p. 720, 1958.
- [171] P. Kumar and C. Mosheim, "Effect of intermetallic compounds on the properties of tantalum," *Int. J. Refract. Met. Hard Mater.*, vol. 12, no. 1, pp. 35–40, 1993.
- [172] D. S. Wu, C. C. Chan, and R. H. Horng, "Material characteristics and thermal stability of cosputtered Ta-Ru thin films," *J. Vac. Sci. Technol. A Vacuum, Surfaces, Film.*, vol. 17, no. 6, p. 3327, 1999.
- [173] L. Liu, H. Gong, Y. Wang, J. Wang, A. T. S. Wee, and R. Liu, "Annealing effects of tantalum thin films sputtered on [001] silicon substrate," *Mater. Sci. Eng. C*, vol. 16, no. 1-2, pp. 85–89, 2001.